IMPLEMENTATION AND ASSESSMENT OF HELLSTEN EXPLICIT ALGEBRAIC REYNOLDS STRESS K-OMEGA MODEL

A THESIS SUBMITTED TO
THE GRADUATE SCHOOL OF NATURAL AND APPLIED SCIENCES
OF
MIDDLE EAST TECHNICAL UNIVERSITY

BY

UMUT İLHAN

IN PARTIAL FULFILLMENT OF THE REQUIREMENTS
FOR
THE DEGREE OF MASTER OF SCIENCE
IN
MECHANICAL ENGINEERING

SEPTEMBER 2022

Approval of the thesis:

IMPLEMENTATION AND ASSESSMENT OF HELLSTEN EXPLICIT ALGEBRAIC REYNOLDS STRESS K-OMEGA MODEL

submitted by **UMUT İLHAN** in partial fulfillment of the requirements for the degree of **Master of Science in Mechanical Engineering Department, Middle East Technical University** by,

Prof. Dr. Halil Kalıpçılar
Dean, Graduate School of **Natural and Applied Sciences** _____

Prof. Dr. Mehmet Ali Sahir Arıkan
Head of Department, **Mechanical Engineering** _____

Prof. Dr. Mehmet Haluk Aksel
Supervisor, **Mechanical Engineering, METU** _____

Assist. Prof. Dr. Özgür Uğraş Baran
Co-supervisor, **Mechanical Engineering, METU** _____

Examining Committee Members:

Assist. Prof. Dr. Ali Karakuş
Mechanical Engineering, METU _____

Prof. Dr. Mehmet Haluk Aksel
Mechanical Engineering, METU _____

Assist. Prof. Dr. Özgür Uğraş Baran
Mechanical Engineering, METU _____

Assist. Prof. Dr. Hediye Atik
Aerospace Engineering, Atılım University _____

Assist. Prof. Dr. Onur Baş
Mechanical Engineering, TEDU _____

Date:

I hereby declare that all information in this document has been obtained and presented in accordance with academic rules and ethical conduct. I also declare that, as required by these rules and conduct, I have fully cited and referenced all material and results that are not original to this work.

Name, Surname: Umut İlhan

Signature :

ABSTRACT

IMPLEMENTATION AND ASSESSMENT OF HELLSTEN EXPLICIT ALGEBRAIC REYNOLDS STRESS K-OMEGA MODEL

İlhan, Umut
M.S., Department of Mechanical Engineering
Supervisor: Prof. Dr. Mehmet Haluk Aksel
Co-Supervisor: Assist. Prof. Dr. Özgür Uğraş Baran

September 2022, 91 pages

Turbulence modeling is one of the most challenging aspects of Computational Fluid Dynamics (CFD). The choice of turbulence model affects the accuracy and computational cost of the CFD analyses. Linear Eddy Viscosity Models (LEVMs) are commonly used in industrial CFD applications due to their low computational cost and ease of convergence. However, they often fail to model complex flow structures. More advanced models, such as Reynolds Stress Transport Models (RSTMs), have better performance for capturing the complex flow physics. RSTMs suffer from convergence difficulties and high computational requirements. In order to combine the computational cost advantage of LEVMs with the accurate prediction of complex flow physics of RSTMs, Explicit Algebraic Reynolds Stress Models (EARSMs) have been introduced. Hellsten utilizes Wallin-Johansson Explicit Algebraic Reynolds Stress Model (WJ-EARSM) as a constitutive model and Menter's Shear Stress Transport Model as a baseline model for k and ω transport equations. Hellsten slightly modified the transport model equations and calibrated the model coefficients to implement WJ-EARSM on the base turbulence model. This model is claimed to be fa-

vorable by having similar computational cost and coding advantages to the SST and a similar level of accuracy to the WJ-EARSM. In this thesis, Hellsten's $k-\omega$ EARSM, which is designed for high-lift aerodynamics, is implemented to open-source CFD code flowPSI. The model is validated using seven different generic turbulence model validation and high-lift aerodynamic test cases.

Keywords: Turbulence, Turbulence Model, EARSM, CFD

ÖZ

HELLSTEN BELİRTİK CEBİRSEL REYNOLDS GERİLİM K-OMEGA MODELİNİN UYGULANMASI VE DEĞERLENDİRİLMESİ

İlhan, Umut
Yüksek Lisans, Makina Mühendisliği Bölümü
Tez Yöneticisi: Prof. Dr. Mehmet Haluk Aksel
Ortak Tez Yöneticisi: Dr. Öğr. Üyesi. Özgür Uğraş Baran

Eylül 2022, 91 sayfa

Türbülans modellemesi hesaplamalı akışkanlar dinamiği için zorlu konulardan biridir. Türbülans modeli seçimi hesaplamalı akışkanlar dinamiği analizlerinin doğruluğunu ve hesaplama zamanlarını etkiler. Doğrusal Girdap Viskozite Modelleri, göreli olarak daha az miktarda hesaplama zamanına ihtiyaç duymaları ve yakınsamalarındaki kolaylık nedeni ile endüstriyel uygulamalarda sıkça tercih edilmektedir. Ancak bu modeller karmaşık akış yapılarını modellemede yetersiz kalmaktadırlar. Reynolds Gerilim Taşınım Modelleri gibi daha gelişmiş modeller bu karmaşık akış fenomenlerini daha başarılı şekilde yakalayabilmekte ancak yakınsama zorluklarından ve yüksek hesaplama gereksinimlerinden dolayı pratikte kullanımamaktadırlar. Doğrusal Modellerin hesaplama maliyeti avantajlarından ve Reynolds Gerilim Modelleri'nin karmaşık akış fiziğini doğru tahmin etme özelliklerinden faydalanmak için Belirtik Cebirsel Reynolds Gerilim Modelleri oluşturulmuştur. Hellsten, yapısal model olarak Wallin–Johansson Belirtik Cebirsel Reynolds Gerilim Modeli'ini kullanmış, k ve ω taşınım denklemleri için ise Menter'in Kayma Gerilim Taşınım Modelini temel al-

mıştır. Hellsten taşınım modeli denklemlerini bir miktar değiştirerek ve model katsayılarını kalibre ederek kullanmaktadır. Bu modelin, Kayma Gerilim Taşınım Modeli'nin benzer hesaplama maliyetine ve kodlama avantajlarına sahip olmakla birlikte Wallin-Johansson Belirtik Cebirsel Reynolds Gerilim Modeli ile benzer doğruluk düzeyine sahip olduğu belirtilmektedir. Bu tezde, yüksek kaldırmalı aerodinamik için tasarlanan Hellsten'in Belirtik Cebirsel Reynolds Gerilim $k - \omega$ Modeli açık kaynak hesaplamalı akışkanlar dinamiği kodu olan flowPsi'ye uygulanmıştır. Bu model yedi farklı genel türbülans modeli doğrulama problemleri ve yüksek kaldırmalı aerodinamik problemleri kullanılarak doğrulanmıştır.

Anahtar Kelimeler: Türbülans, Türbülans modeli, BCRGM, HAD

To my family

ACKNOWLEDGMENTS

I would like to express my deepest gratitude to my co-supervisor, Assist. Prof. Dr. Özgür Uğraş Baran, for his valuable guidance, advice, criticism, and encouragement throughout the thesis. I would also like to thank Prof. Dr. Mehmet Haluk Aksel for his help during the thesis study.

I would like to thank my colleagues in Aerodynamic Design and Analysis Department of ROKETSAN, especially Ulaş Canberk Ayan, for their discussions and support that he shared with me throughout the thesis.

I would like to thank my parents, Nesrin İlhan and Ayhan İlhan, for their love, support, and sacrifices throughout my educational life.

I would also like to thank my lovely girlfriend, Ceren Barlak, for her endless love, support, and understanding throughout the thesis study. This thesis would never have been written without her love and understanding.

TABLE OF CONTENTS

LIST OF TABLES

TABLES

LIST OF FIGURES

FIGURES

LIST OF ABBREVIATIONS

ABBREVIATONS

2D	Two-Dimensional
3D	Three-Dimensional
ARSM	Algebraic Reynolds Stress Model
BSL	Baseline Model of Menter
CFD	Computational Fluid Dynamics
DNS	Direct Numerical Simulation
EARS	Explicit Algebraic Reynolds Stress
EARSM	Explicit Algebraic Reynolds Stress Model
EVM	Eddy Viscosity Model
GWJ	Grundestam-Wallin-Johansson
LES	Large Eddy Simulation
LEVM	Linear Eddy Viscosity Model
LRR	Launder-Reece-Rodi
N-S	Navier-Stokes
NLEVM	Non-linear Eddy Viscosity Model
RANS	Reynolds Average Navier Stokes
RSTM	ReynoldsStress Transport Model
SSG	Speziale-Sarkar-Gatski
SST	Shear Stress Transport Model of Menter
TCM	Tandem Control Missile
WJ	Wallin-Johansson

LIST OF SYMBOLS

SYMBOLS

$\beta_1, ..., \beta_9$	Coefficients in the explicit tensor expression for the Reynolds stress anisotropy
C_D	Drag coefficient
C_L	Lift coefficient
C_f	Skin friction coefficient
C_m	Pitching moment coefficient
C_p	Pressure coefficient
ρ	Fluid density
F_1	Mixing function of Menter's SST
Ω^*_{ij}	Mean vorticity tensor nondimensionalized by the turbulent timescale
P	Turbulence production term
Re	Reynolds Number
S^*_{ij}	Mean strain rate tensor nondimensionalized by the turbulent timescale
S_{ij}	Mean strain rate tensor
a_{ij}	Reynolds stress anisotropy tensor
β^*	Model coefficient
δ_2	Momentum thickness
δ_{ij}	Kronecker's delta
d	Distance to the nearest wall point
f_{mix}	Mixing function of Hellsten
$\Gamma, \Gamma_1, \Gamma_2, \Gamma_3$	Arguments of mixing function
γ	Model coefficient
g	Gravity

k_s^+	Sand roughness height, k_s, scaled by the viscous length scale
k	Turbulent kinetic energy per unit mass
μ_{eff}	Effective dynamic viscosity
μ_t	Eddy viscosity
μ	Dynamic viscosity of fluid
p	Fluid pressure
σ	Model coefficients of diffusive terms
τ_{ij}	Reynolds stress tensor
τ	Turbulent timescale
u_i	Fluid velocity in i direction
u_τ	Friction velocity
ω	Specific dissipation rate
y_w^+	Wall normal coordinate scaled by the viscous length scale

CHAPTER 1

INTRODUCTION

Throughout the aviation history, experimental fluid dynamics, especially wind tunnels, have played a crucial role in aircraft design. Wind tunnel testing is highly costly and time-consuming, despite being far more practical than flight testing. Therefore, replacing wind-tunnel tests with alternative procedures that are more cost-effective would be of enormous benefit to the aeronautical industry. Analytical methods were the only available theoretical tools in the past until the 1960s. These tools require less time compared to experiments. On the other hand, they may lead to a loss of accuracy since their derivations include many unphysical assumptions such as assuming flow to be inviscid. Fortunately, another practical tool, Computational Fluid Dynamics (CFD), emerged when digital computers became generally available.

One of the key elements of the CFD in today's engineering is turbulence modelling. Turbulence is associated with the three-dimensional, time-dependent, irregular and dissipative motion of a fluid, which is mainly observed at high Reynolds numbers [12]. Reynolds number is a nondimensional measure of the ratio of intertial and viscous forces. The Reynolds number can be expressed as given in Equation (1.1):

$$Re = \frac{\rho U^2/L}{\mu U/L} = \frac{\rho U L}{\mu} \tag{1.1}$$

Reynolds number is generally high for the flow past over a typical transport aircraft wing. Therefore, turbulence modeling plays a crucial role in modeling flow physics accurately in high Reynolds number analyses of aerospace problems.

These high Re flows are modeled by a highly nonlinear system of partial differential equations called Navier-Stokes equations. These equations do not have analytical

solutions. In addition, their numerical solutions are not simple.

Direct Numerical Simulation (DNS) and Large Eddy Simulation (LES) are the only available tools to numerically solve the turbulent motion of fluid without utilizing turbulence models. DNS is utilized for low Reynolds number flows in basic geometries for research purposes rather than engineering applications today. In theory, only the massive computing and storage capacity requirements restrict its application to engineering applications. Argyropoulos et al. [13] estimated, for instance, that the DNS of a turbulent channel flow with a Reynolds number of 800,000 required a computer that is 500,000 times faster than the fastest supercomputer available in 2015. For these reasons, Reynolds Averaged Navier-Stokes (RANS) equations provide the optimum solutions for the majority of engineering problems, including aerodynamics, currently and in the near future.

1.1 Governing Equations of Fluid Flow

The viscous motion of a fluid flow is governed by the Navier-Stokes equations (N-S). In this section, the conservation of mass and momentum of a viscous flow will be presented. The tensor notation will be used throughout the thesis whenever applicable. Repeated indices show that the Einstein summation convention is applied.

Conservation of mass in Cartesian coordinates form can be written as in Equation (1.2):

$$\frac{\partial \rho}{\partial t} + \frac{\partial (\rho u_i)}{\partial x_i} = 0 \tag{1.2}$$

where u_i is the fluid velocity. Conservation of momentum of an incompressible viscous flow is given in Equation (1.3):

$$\frac{\partial (\rho u_i)}{\partial t} + \frac{\partial (\rho u_i u_j)}{\partial x_j} = \frac{\partial p}{\partial x_i} + \mu (\frac{\partial^2 u_i}{\partial x_j \partial x_j}) + \rho g \tag{1.3}$$

where p is the pressure and ρ is the fluid density, and μ is the dynamic viscosity of the fluid.

1.1.1 Reynolds Averaged Navier-Stokes Equations

Local pressure, density, velocity components, and temperature vary randomly with time in turbulent flows. The separation of the flow variables into stationary and random parts is called Reynolds decomposition. The flow quantities are represented as a sum of mean and fluctuating parts. Examples for fluid velocity u_i and pressure p are given in Equation (1.4).

$$u_i(x_i,t) = \overline{u}_i(x_i) + u_i^{'}(x_i,t), \quad p(x_i,t) = \overline{p}(x_i) \ \ + p^{'}(x_i,t) \tag{1.4}$$

In turbulence-model research, there are three types of averaging: time average, spatial average, and ensemble average. "Mean" is the broad term used to characterize various averaging methods. The most frequent type of averaging is the first, time averaging. It can only be utilized for stationary turbulence, i.e., for a turbulent flow that time averaged the flow variables is independent of time or origin of time. The mean velocity value for such a flow is defined as in Equation (1.5):

$$\overline{u_i}(x_i) = \lim_{T\to\infty} \frac{1}{T} \int_{t}^{t+T} u_i(x_i,t)dt \tag{1.5}$$

T in Equation (1.5) is chosen to be sufficiently longer than the time scale of the rapid fluctuations and shorter than that of the slow motion.

Moreover, as a reasonable suggestion for compressible flows, density-weighted Favre averaging is utilized as Equation 1.6:

$$\widetilde{u_i} = \frac{\overline{\rho u_i}}{\overline{\rho}} \tag{1.6}$$

Considering the generic flow variable ϕ and ψ, the properties for the average operator presented in Equations (1.7) and (1.8) are hold as it is given by Tennekes [12]:

$$\overline{\phi'} = \overline{\psi'} = 0, \quad \overline{\phi\psi} = \overline{\phi}\,\overline{\psi} + \overline{\phi'\psi'}, \quad \overline{\overline{\phi}\phi'} = \overline{\overline{\psi}\psi'} = \overline{\overline{\phi}\psi'} = \overline{\overline{\psi}\phi'} = 0 \tag{1.7}$$

$$\overline{\phi^2} = \overline{\phi}^2 + \overline{\phi'^2}, \quad \frac{\overline{\partial \phi}}{\partial t} = \frac{\partial \overline{\phi}}{\partial t}, \quad \frac{\overline{\partial \phi}}{\partial x_i} = \frac{\partial \overline{\phi}}{\partial x_i} \tag{1.8}$$

By substituting the Reynolds decomposition in Equation (1.4) into the conservation of mass and momentum equations in (1.2) and (1.3), one can obtain Equations (1.9) and (1.10).

$$\frac{\partial(\rho(\overline{u_i} + u_i^{'}))}{\partial x_i} = 0 \tag{1.9}$$

$$\frac{\partial(\rho(\overline{u_i} + u_i^{'}))}{\partial t} + \frac{\partial}{\partial x_j}(\rho(\overline{u_i} + u_i^{'})(\overline{u_j} + u_j^{'})) = \frac{\partial(\overline{p} + p^{'})}{\partial x_i} + \mu(\frac{\partial^2 \left(\overline{u_i} + u_i^{'}\right)}{\partial x_j \partial x_j}) + \rho g \tag{1.10}$$

By applying the rules given in Equations (1.7) and (1.8) to Equation (1.10), RANS equations are obtained:

$$\frac{\partial(\rho\overline{u_i})}{\partial x_i} = 0 \tag{1.11}$$

$$\frac{\partial \rho \overline{u_i}}{\partial t} + \frac{\partial}{\partial x_j}(\rho \overline{u_i}\,\overline{u_j}) = -\frac{\partial \overline{p}}{\partial x_i} + \mu(\frac{\partial^2 \overline{u_i}}{\partial x_j \partial x_j}) - \frac{\partial}{\partial x_j}(\rho \overline{u_i^{'} u_j^{'}}) + \rho g \tag{1.12}$$

where $-\rho\overline{u_i^{'}u_j^{'}}$ appeared in Equation (1.12) can be replaced by the tensor given in Equation (1.13).

$$\tau_{ij} = -\rho\overline{u_i^{'}u_j^{'}} \tag{1.13}$$

τ_{ij} is named as Reynolds stress tensor and acts as additional stress in the fluid flow. This term describes the influence of turbulent motions on mean stresses. The diagonal components of the Reynolds stress tensor are normal stresses, while the off-diagonal components are shear stresses. Moreover, the Reynolds stress tensor is a symmetric tensor.

1.2 Closure Problem of Turbulence

As a result of temporal averaging, the Reynolds averaged momentum equations contain unknown variables called Reynolds stresses. There are six more unknowns than equations. In order to obtain a closed form of the solution, these unknown variables must be supplied to the equations. This problem is called the closure problem of turbulence. It requires new algebraic or differential equations to solve this problem. A set of equations that supply unknown variables to the solution is named "turbulence closure models" [14].

Three types of RANS-based turbulence closure models are currently used by the CFD community. These are Linear Eddy Viscosity Models (LEVMs), Reynolds Stress Transport Models (RSTMs) and Nonlinear Eddy Viscosity Models (NEVMs), to which Explicit Algebraic Reynolds Stress Models (EARSMs) belong. These models are briefly discussed in the corresponding subsections.

1.2.1 Boussinesq Hypothesis and Linear Eddy Viscosity Models

In this section, LEVMs are described briefly. The most common LEVMS are categorized as zero- or algebraic mixing length, one-, and two-equation models. These models are based on the Boussinesq assumption [15] that the turbulent stress tensor can be expressed in terms of the mean rate of strain in the same manner as the viscous stress for Newtonian isotropic fluid, with the exception that the coefficient of the molecular viscosity is replaced by the eddy viscosity [14].

$$\tau_{ij} = -\rho\overline{u_i' u_j'} = 2\mu_t(S_{ij} - \frac{1}{3}\frac{\partial u_k}{\partial x_k}\delta_{ij}) - \frac{2}{3}\rho k\delta_{ij} \tag{1.14}$$

where μ_t appeared in Equation (1.14) is turbulent viscosity or eddy viscosity, k is turbulent kinetic energy, and S_{ij} is mean strain rate. Note that the final term of Equation (1.14) for zero-equation models, which do not employ turbulent kinetic energy k, is zero.

$$k = \sqrt{\frac{1}{2}(\overline{u_1'^2} + \overline{u_2'^2} + \overline{u_3'^2})} \tag{1.15}$$

$$S_{ij} = \frac{1}{2}(\frac{\partial u_i}{\partial x_j} + \frac{\partial u_j}{\partial x_i}) \tag{1.16}$$

A direct analogy between the formulation of the molecular and turbulent flux of momentum makes it possible to express the total flux in terms of effective values. For instance, effective dynamic viscosity, utilized in viscous fluxes, is calculated as presented in equation (1.17).

$$\mu_{eff} = \mu + \mu_t \tag{1.17}$$

where μ is fluid viscosity and μ_t is turbulent viscosity, also called eddy viscosity. The LEVM method yields the same form of conservation equations as for laminar flows, with the exception that the fluid variable coefficients are substituted with their effective values. Since the same methodology and computational code may be used for both laminar and turbulent transport processes without change, this method is computationally very convenient and easy to implement. In flows with high Reynolds numbers, the eddy viscosity is orders of magnitude greater than the molecular viscosity unless in the vicinity of a solid wall, where turbulent oscillations are dampened.

LEVMs can frequently be applied successfully to two-dimensional (2D) or weakly three-dimensional (3D) boundary layers, and other thin shear flows that are close to equilibrium. In such flows, only a single Reynolds stress component is significant. The linear relationship between strain rate and Reynolds stress tensor may provide an accurate stress component if the model has been appropriately calibrated. However, it cannot offer more than one component correctly in general. Consequently, it is anticipated to fail in flows when several stress components have a considerable impact on the mean flow. Strongly 3D flows, strongly curved mean flows, irrotational impinging flows, whirling flows, turbulence-driven secondary flows, are examples of such flows. LEVMs are also fully insensitive to the flow's rotation rate and, as a result, cannot be sensitive to system rotation or streamline curvature unless a correction is introduced; hence, they cannot be used in the flow of rotating systems.

As Grundestam et al. [16] indicate, flows impacted by rotation, separation, and streamline curvature are of great interest because they play a crucial role in numerous engineering problems, such as aeronautics and turbomachinery. The application of high-lift aerodynamics is of tremendous interest when all these flow structures are present. In spite of the well-known shortcomings of these LEVMs, the development of new one- and two-equation models persists. Due to the computational robustness of these models and the fact that many turbulent flows of practical significance are dominated by one component of the turbulent shear stress, necessitating a satisfactory closure for this one component of the Reynolds stress tensor. Boussinesq's hypothesis linking the shear stress to the mean velocity gradient is typically enough for such shear stress closures [2].

Two-equation models, such as $k - \varepsilon$ and $k - \omega$ models, are by far the most prevalent and computationally efficient models for engineering applications today, which will be discussed in the related subsections. One equation LEVMs are advantageous in terms of computing time and complexity since they require only one additional transport equation to be solved. One-equation modeling has become quite popular in the field of aerodynamics after Baldwin and Barth [17] and later Spalart and Allmaras [18] published their models that are based on general transport equations for the eddy viscosity (or Reynolds number) and tuned for aerodynamic flow problems. The Baldwin-Barth model, however, was never as popular as its successor, the Spalart-Allmaras model, which has become widely preferred model in aerodynamics. Earlier single-equation models were founded on the transport equation for k with a specified length scale. Such models have a more limited range of applicability than two-equation models in which the second scale variable is derived from a modeled transport equation. Clearly, recent one-equation models, such as the Spalart-Allmaras model, are also incomplete, due to the fact that the second scale-variable does not appear directly in their formulation. These models are optimal for simple boundary-layer flows [8].

1.2.1.1 Two-Equation Eddy Viscosity Models

Two-Equation EVMs are the most popular class of LEVMs. Their main benefit is their simplicity and compatibility for simple integration into current N-S numerical codes. In a few simple classes of flows, computations of a variety of flows have demonstrated remarkable consistency with experimental measurements, such as 2D attached boundary layers and flows with pressure gradients, some recirculating flows etc. Two-equation models can be effective in engineering if their limits are understood [14].

Two-equation models utilize two transport equations for two turbulence quantities in addition to the mean-flow N-S equations. The first is typically that of the turbulent kinetic energy k, while the second can be any of a number of variables, such as the dissipation rate of turbulence kinetic energy (ε), the specific dissipation rate (ω), the length scale (l), the product of $k - l$, the time scale τ, the product of k and τ [19]. This category of models is the most popular in the industry, and this trend is likely to continue in the near future [20].

The k–ε model is by far the most commonly used and tested two-equation model, with numerous enhancements over the years [13]. Launder and Spalding [21] published the most well-known linear $k - \varepsilon$ model. The initial low Reynolds number version $k - \varepsilon$ model was developed by Jones and Launder [22]. Numerous authors have modified these models since their initial publication. The k–ε model has been quite successful in a wide range of flow conditions, despite its well-known drawbacks. From an aerodynamics perspective, the lack of sensitivity to adverse pressure gradients is the most worrying aspect. Under adverse pressure gradient condition, the model overestimates the shear-stresses, delaying or completely preventing separation. Rodi et al. [23] attribute this problem to the overprediction of the turbulent length-scale in the near wall region and have demonstrated that a modification offered by Hanjalic and Launder [24] significantly improves the predictions. Moreover, Yakhot and Orszag [25] demonstrated a significant improvement in the prediction of the recirculation length in separating flows [14].

In the quest for better models, a variety of alternative two-equation models have been

presented, with the choice of scale-providing variable serving as the primary distinction. Wilcox's $k - \omega$ model is one of the most successful in terms of accuracy and robustness [26]. This model solves one equation for the turbulent kinetic energy k and another for the specific turbulent dissipation rate ω. This model was mostly favored by some CFD users, primarily aerodynamicists, because it appears to be more robust and requires no adjustment for the region close to the wall [14]. The model performs significantly better than the $k - \varepsilon$ model under adverse pressure gradient conditions [27]. Menter et al. [28] stated that ω-equation-based models offer substantial advantages over ε-equation-based models, particularly when viscous sublayer integration is required.

Nonetheless, Wilcox model has its own shortcomings. The most significant shortcoming was the extreme sensitivity to the free-stream values chosen for ω [29, 30]. This freestream sensitivity resulted in a considerable dependence of the solution on somewhat arbitrary values specified for k and ω at the inlet, as well as their decay upstream of the aerodynamic vehicle [28]. This issue has been thoroughly examined, and it has been demonstrated that the magnitude of the eddy viscosity can be altered by more than 100 percent simply by varying the farfield values of ω [29]. Menter et al. [31] created a zonal Baseline (BSL) $k - \omega$ model to compensate for the shortcomings of the Wilcox $k - \omega$ model. In the inner 50 percent of the boundary layer, the BSL model is identical to the Wilcox model, then gradually transforms to the $k - \varepsilon$ model of Jones and Launder [22]. The performance of the BSL model for adverse pressure gradient boundary-layer flows was remarkably close to that of the Wilcox $k - \omega$ model without the unwanted free stream dependence. Although the Wilcox and the BSL $k - \omega$ models perform better than the $k - \varepsilon$ model in flows with adverse pressure gradients, they continue to underestimate the amount of separation in flows with severe adverse pressure gradients [27]. Menter et al. [32] developed the Shear Stress Transport (SST) model in order to improve the BSL model further. In addition to employing the method of blending between $k - \omega$ and $k - \varepsilon$ via a blending function, this model can also account for the transport of the primary turbulent shear stress in boundary layers with adverse pressure gradient. The definition of the eddy-viscosity in this model is based on the assumption of Bradshaw that the principal shear stress is proportional to the turbulent kinetic energy. The BSL and the SST

models are not considerably more complex than the original $k-\omega$ model and require only a slight increase in computational time. Menter's SST model is the reasonably accurate at predicting severe adverse pressure gradient boundary layers and flow separation compared to all other two-equation models. The SST model is implemented into the majority of the general-purpose commercial CFD software. In other words, the model's application range has greatly grown beyond its initial aerodynamic purpose. The model has been validated against numerous applications with promising results, including free shear layers, zero pressure gradient and adverse pressure gradient boundary layers [13]. Recent modifications to the model include an improved version for the rotation and the streamline-curvature [33] and the substitution of vorticity in the eddy viscosity with strain rate [28].

The aforementioned two-equation models have poor performance in many applications, such as flows with strong curvature, strong buoyancy influences, low-Reynolds-number effects, strong swirl, etc. [13]. Two-equation models additionally neglect nonlocal and history effects on Reynolds-stress anisotropies. The shortcomings of the two-equation models are mostly attributable to the fact that the representation of turbulence by its kinetic energy alone cannot adequately describe turbulence anisotropy. Also, linear constitutive relation leads to a rigid stress-strain coupling [34]. Unless production clipping is implemented, these models also tend to overestimate eddy viscosity close to vortex cores. Correct estimation of eddy-viscosity near vortex cores is important in most aerodynamic flows to accurately model the vortex interaction between components of devices. In these circumstances, more sophisticated turbulence models are necessary. One way is to use Reynolds-Stress Transport Models (RSTMs), which will be looked at in the next section.

1.2.2 Reynolds Stress Transport Models

Reynolds Stress Transport Models (RSTMs) or Differential Second-Moments are based on the Reynolds-stress transport equations. Six more transport equations must be solved for the individual Reynolds-stress tensor components. These models provide the most advanced degree of RANS turbulence modeling currently accessible for practical application [8]. Chou defined the RSTM's fundamental notions as early

as 1945 [35]. A few years later, Rotta made a significant and lasting contribution to Reynolds-stress modelling [36]. In the 1970s, the RSTM grew in popularity as a result of the influential work of Hanjalić and Launder [37] and Launder, Reece, Rodi [38]. Since then, several researchers have contributed to the topic, proposing models with varied levels of description and complexity [8]. The most well known RSTMs are Launder-Reece-Rodi (LRR) [38] model and Speziale-Sarkar-Gatski (SSG) [39] model.

A solution of a separate transport equation for each component of the turbulent stress permits, in principle, accurate prediction of the turbulent stress field and its anisotropy. Accurate prediction of turbulence anisotropy plays a critical role in complex flows, either as a major source of turbulence energy, such as in the stagnation regions, as a source of secondary motion, or in controlling the dynamics of longitudinal vortices. It is also essential to accurately predict the wall-normal stress component when simulating the wall shear stress, heat and mass transfer. In addition, capturing stress anisotropy provides accurate modelling of the scale-determining equation [8].

The RSTM has not acquired notable popularity within the industry and among other end-users for several reasons, despite the widespread knowledge of the LEVMs' notable weaknesses and shortcomings [40]. One of the reasons is the necessity to model additional terms to provide a better representation of the physics of diverse turbulence interactions. However, if some terms are modeled incorrectly, this advantage may be nullified. Because the model transport equations are not well coupled, the usage of RSTM places a higher demand on computational resources and necessitates a higher level of skill from the code user [14]. In addition, the development of such models is more difficult and requires a deeper understanding of the physics of turbulence in order to develop mathematically and physically consistent closures. Due to this, fewer alternative RSTM formulations are currently available [41]. Moreover, few commercial CFD packages offer RSTM as a modelling alternative. Even fewer industrial users recognize the RSTM's inherent superiority. Most of these models are used and studied in the academic world, where they are still seen as a work in progress rather than a tried and true way to solve complex flow problems [14].

1.2.3 Explicit Algebraic Reynolds Stress Models

Flows impacted by rotation, the streamline curvature, and separation are the central concerns for turbulence models. These processes are of great interest because they play a crucial role in numerous engineering applications, such as aeronautics and turbomachinery. High-lift aerodynamics is such application in which all of these effects are observed [16]. In complex flow problems typical in high-lift aerodynamics, a linear relationship between the Reynolds-stress and the mean strain-rate tensors utilized in two-equation models might be an overly restrictive assumption. Therefore, it is necessary to seek other turbulence models with a larger range of applications than the Boussinesq models. Since RSTMs are regarded as too difficult for industrial high-lift aerodynamic design, we require a model that falls between RSTMs and LEVMs [8].

Fortunately, the two-equation models may be adapted for this purpose by establishing more sophisticated nonlinear relationships between the stress tensor, the mean-velocity gradient, and the turbulent scales. Typically, these correlations are known as constitutive models. The two-equation turbulence models can be viewed as having two more or less distinct components: the scale determining model, which offers scalar information on the turbulence (k and ω), and the constitutive model, which determines the Reynolds stress tensor (τ_{ij}). The Explicit Algebraic Reynolds Stress models (EARSMs) are promising subset of nonlinear constitutive models. A portion of the higher-order description of physical processes at the RSTM-level is transferred to the two-equation modeling level in this technique. The EARSM approach is an appropriate constitutive modeling technique for capturing relevant physical processes observed in high-lift aerodynamics [8, 41].

EARSMs can alternatively be perceived as nonlinear two-equation models because the linear stress-strain connection is abandoned in the EARSM approach [42]. Nonlinear Eddy Viscosity Models (NLEVMs) are non-linear extensions of LEVMs, whereas EARSMs are truncations of RSTMs [40, 13]. The relationships between various modelling classes are shown in figure 1.1 taken from Gatski [2].

EARSMs are simplified versions of RSTMs generated by omitting Reynolds stress

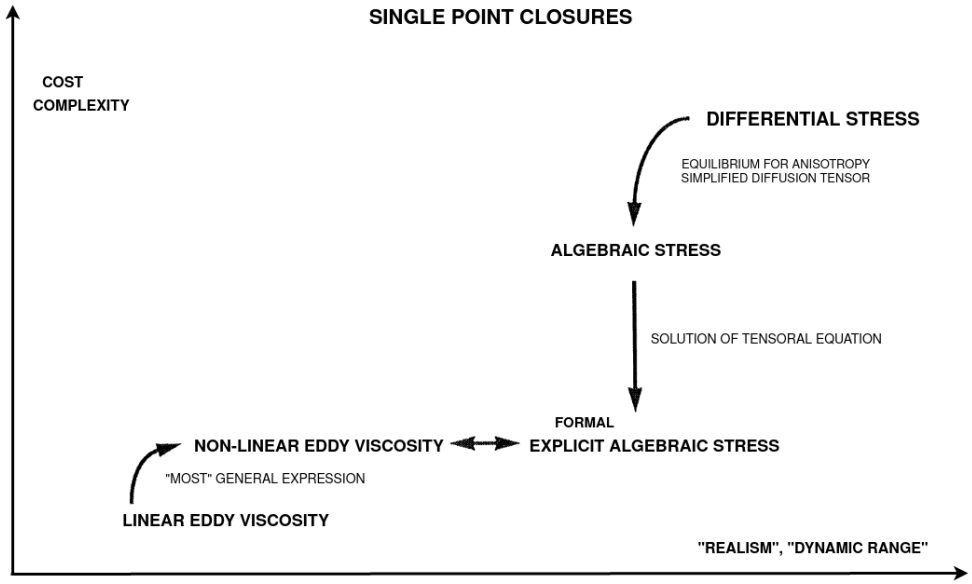

Figure 1.1: Relationship between turbulence models as given by Gatski [2]

transport terms and replacing them with turbulent kinetic energy and length scale equations [13]. In addition, these models are founded upon the transport equation of the stress-anisotropy tensor [42]. However, the EARSM method fails to account for the space and time evolution of the anisotropy tensor. In contrast, they can reproduce anisotropy in normal stresses, which is beyond the capability of LEVMs [43]. The Reynolds-stress components can be separated into an isotropic part and an anisotropic part, which is defined simply as the deviation from the isotropic component [44]. Reynolds-stress tensor utilized in EARSMs can be found in Equation (1.18).

$$\tau_{ij} = -\rho\overline{u_i' u_j'} = 2\mu_t(S_{ij} - \frac{1}{3}\frac{\partial u_k}{\partial x_k}\delta_{ij}) - \frac{2}{3}\rho k\delta_{ij} - a_{ij}\rho k \tag{1.18}$$

As demonstrated by Equation (1.18), a new term is added to the Boussinesq hypothesis-based Reynolds stress equation. This term, a_{ij}, is the Reynolds stress anisotropy tensor, which affects the wall heat and mass transfer [14]. Modeling the eddy viscosity and Reynolds stresses as isotropic in LEVMs can be an oversimplification for three-dimensional flows, particularly in aerodynamics. This problem is depicted in Figure 1.2 where eddy-viscosities in two different directions inside a 3D wing-body junction boundary layer of Devenport and Simpson's experiment [3]. If the LEVMs are used in these types of problems, eddy viscosity and Reynolds stresses do not change

with direction. Hence, eddy viscosities should be on the isotropic line, which has a slope of 1. Modeling the Reynolds-stress anisotropy is crucial in complex 3D flow problems.

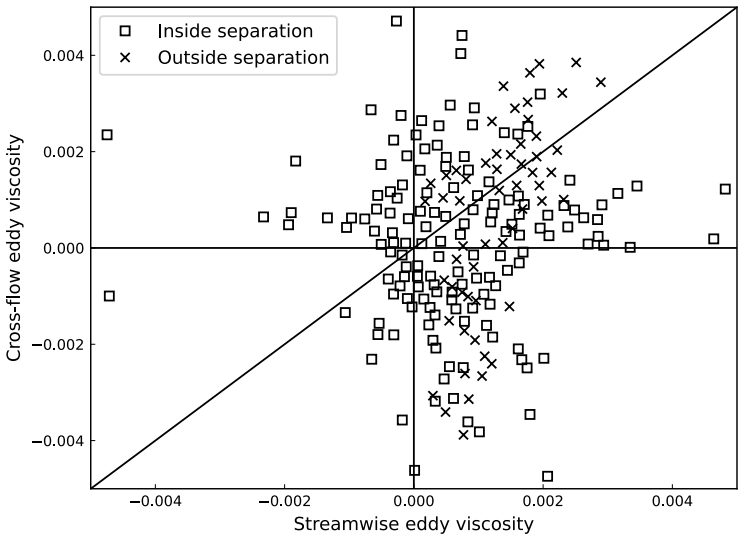

Figure 1.2: Spanwise vs streamwise turbulent viscosity measurement inside a boundary layer for different depths, as given by Devenport and Simpson[3].

EARSMs as an extension to LEVMs primarily appeared during the 1990s, although Pope et al. [45] published remarkable research for two-dimensional flows earlier. Later, Gatski and Speziale [46] and Jongen and Gatski [2] extended and enhanced Pope's model. Gatski and Speziale [46] made the first statement of EARSM that grabbed practical interest in 1993. However, their model has an incorrect asymptotic behaviour in rapidly distorted flows [47]. Gatski-Speziale EARSM is later combined with Wilcox 1988 model and with Wilcox 1998 model by Abid, Rumsey and Gatski [48] and Rumsey and Gatski [49], respectively. In addition, Rung et al. [50] proposed the Realizable Quadratic Eddy Viscosity Model based on the Gatski-Speziale EARSM.

Girimaji [51] introduced another EARSM with the exact solution in the two-dimensional flow and an approximate solution in three-dimensional flows in 1996. Wallin and Johansson [4] developed the Wallin-Johansson EARSM (WJ-EARSM), which is one of the most popular EARSM for the aeronautical applications. Gatski-Speziale and Wallin-Johansson (WJ) EARSMs are both derived from the Launder-Reece-Rodi (LRR) RSTM. Grundestam et al. [16] have introduced the Grundestam-Wallin-Johansson

(GWJ) model, an improved version of the WJ model. However, it performs slightly better than the WJ-EARSM, which is close to being negligible. Also, Wallin and Johansson [52] presented curvature-correction, which claims an improvement in flows where curvature effects are important. According to Crippa et al. [43], the theoretical superiority of curvature correction was not accompanied by sufficient numerical robustness. Hellsten et al. [9] introduced a new $k-\omega$ model which is based on Menter's SST as the two-equation scale determining model and the WJ-EARSM as constitutive model for Reynolds stresses. This model has become one of the most popular EARSM in aerodynamic applications. This model is designed for high-lift aerodynamics in particular. Many researchers employed this model in their CFD codes and applied to various flow problems [53, 54, 47, 43, 55].

EARSMs have comparable computational costs and robustness to LEVMS and are typically no more difficult to use than LEVMs. The additional computational expense relative to LEVMs is often less than 10% according to Hellsten [40]. Nonetheless, these models include a higher level of physical description and can contain many of the same features of the RSTMs. In fact, the EARSMs can be developed such that these characteristics are inherited from the source RSTM [40]. Numerous articles demonstrate that the performance of the EARSMs is more reliable than that of LEVMs for rotating and adverse pressure gradient flows. The application of EARSM significantly improves the prediction of separation length and skin friction in flows with an unfavourable pressure gradient compared to LEVMs [4, 47]. Also, Carri et al. [54] demonstrated that the EARSM method avoids unphysical predictions of the eddy viscosity of vortex cores. However, due to the fact that EARSMs are developed from the presumed RSTMs, their performance is limited to that of the parent RSTM [14].

1.3 Aim of the Thesis

Proper choice of turbulence modeling in aerodynamics is essential for the design and analysis processes of aerodynamic vehicles. Different classes of RANS models are briefly introduced in terms of modelling approaches and advantages. SST model of Menter is one of the prominent turbulence models in aerodynamic applications. It is

robust, computationally cheaper than RSTMs, and has better performance in adverse pressure gradient flows compared to similar LEVMs, as Hanjalic claims [14]. This model is implemented in many open-source and commercial CFD software packages.

However, studies in the literature claim that, proper utilization of EARSM on CFD software might improve the predictions over the LEVMs, including the SST model, without increasing computational time considerably. In this thesis, Hellsten EARS $k-\omega$ model is implemented to an open-source CFD code. Since this model is introduced mainly for high-lift aerodynamic applications, many cases including flow physics observed in high-lift aerodynamic cases are investigated. An open-source CFD implementation of Hellsten EARS $k-\omega$ model is not widely studied. Therefore, this study would be beneficial to assess the characteristic of the Hellsten's model in compressible flow solvers. Flat-plate, Driver's decelerating boundary-layer, and NACA4412 cases are selected to verify model implementation and to observe the model's performance on different flow conditions by comparing the results with experimental and numerical data available in the literature. Transonic flow over RAE2822 airfoil, axisymmetric bump, NASA Tandem Control Missile (TCM), and fin trailing vortex cases are selected to validate the model's performance on external aerodynamic problems with regards to flow field modeling and overall aerodynamic coefficient prediction. All validation and verification cases are compared with the SST model. The goal of this thesis is to assess Hellsten EARS $k-\omega$ model compared to LEVMs.

1.4 Scope of the Thesis

This thesis includes four chapters. The need for turbulence models in CFD analyses is briefly explained in the introduction chapter. Different classes of RANS models are introduced in terms of their aspects, advantages, and available models in the literature. The path leading to the EARSM requirement is briefly explained, and general aspects and different models of EARSMs are shared in the related subsection.

The second chapter aimed to introduce the Hellsten EARS $k-\omega$ model utilized in the thesis. Aspects and equations of the models are given in this chapter.

The third chapter aims to present the results obtained for each case and make meaningful discussions with them. The objective of the selection of each case is presented, and the results' agreement with experiments for each case is discussed.

Finally, chapter 4 concludes the thesis study and summarizes potential future works.

CHAPTER 2

METHODOLOGY

Hellsten Explicit Algebraic Reynolds Stress $k-\omega$ Model [9] is implemented in an open-source CFD solver, flowPsi. In this section, a brief description of the model is given. After that, scale determining and constitutive equations of the model are presented. Moreover, details of the the flow solver are presented.

2.1 Hellsten Explicit Algebraic Reynolds Stress K-Omega Model

Hellsten EARS $k-\omega$ model is created in order to incorporate EARSM into the two-equation $k-\omega$ model [9]. Scale-determining equations that use the transport of turbulent kinetic energy, k, and specific dissipation rate, ω, have a similar structure to Menter's SST model, but the model equations and coefficients have been entirely recalibrated. In addition, the linear relationship between the mean strain-rate tensor and the Reynolds-stress tensor is abandoned in favor of the WJ-EARSM model. Hellsten's model is intended primarily for aerodynamic applications, particularly high-lift aerodynamics. This does not imply that the model is inappropriate for all other flow problems; instead, the focus is on flow phenomena that play a significant role in conventional high-lift aerodynamics problems. This model, according to Hellsten et al. [9], is applicable to a broader range of flows than the majority of existing $k-\omega$ models.

At the beginning of model development, $k-\omega$ models are chosen as the scale-determining model [8, 9]. The primary argument for selecting $k-\omega$ models over $k-\varepsilon$ models is the overestimation of skin friction and delayed separation prediction with $k-\varepsilon$ models in practical flow simulations [9]. Also, Hellsten et al. [42]

demonstrated that $k-\varepsilon$ models are failed to model the separation physics in flows with an adverse pressure gradient regardless of whether or not EARSM is utilized. Nevertheless, linear $k-\omega$ models and EARSMs based on $k-\omega$ models yielded good results [42]. Wallin [4] similarly observed that, as the rate of rotation increases, $k-\varepsilon$ models exhibit a greater shear stress than the $k-\omega$ models. Hellsten et al. [8] also claimed that not all $k-\omega$ models could be employed with EARSMs for constitutive equations. Incompatible models include Wilcox's models [26, 30] and Kok's $k-\omega$ turbulent/nonturbulent (TNT) model [56].

Hellsten discovered that when the EARSM relations are used in Reynolds stress calculations without recalibrating the scale-determining model, $k-\omega$ models can exhibit anomalies such as very abnormal hook-shaped velocity profiles. For this reason, Hellsten calibrated his model with various flow problems by mainly focusing on high-lift aerodynamic flows. Calibration flow problems include boundary layers under zero and adverse pressure gradients, channel flow, planar far wake, and mixing layers. Hellsten's model development started with the BSL and SST models of Menter [32, 8]. The SST model was chosen as the final scale-determining model since it has proven to be one of the most suitable and popular two-equation models for aerodynamic applications and it has been discovered that it is more suitable for usage with the EARSM technique [8].

Hellsten selected Wallin-Johansson's EARSM (WJ-EARSM) as the constitutive relation between mean velocity gradient and Reynolds stresses. WJ-EARSM makes advantage of an explicit relationship between the mean flow and Reynolds stresses [4]. Wallin and Johansson [4] noted that if the implicit relation was utilized for the Reynolds stress anisotropy tensor, the model would be numerically and computationally complex due to the absence of diffusion and damping in the equation system. Also, ARSMs that rely on implicit relations require excessive computation time, which leads to losing their advantages over RSTMs [4]. However, WJ-EARSM is comparable to linear two-equation models in terms of robustness and computational time. As illustrated by the convergence history of the RAE2822 wing profile in Figure 2.1 provided by Wallin and Johansson [4], there are no significant differences between the convergence rates of EARSM and the Wilcox $k-\omega$ model. In fact, WJ-EARSM converges to residuals that are lower. The numerical parameters utilized

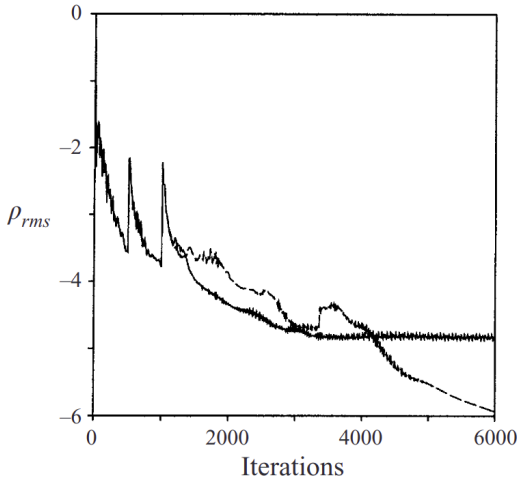

Figure 2.1: Residuals of root mean square of density for RAE2822 profile using WJ-EARSM (—) and Wilcox $k-\omega$ (- - -), as taken from Wallin and Johansson [4]

in RAE2822 profiles for both models are identical, and the calculation time for this example is just 6 percent greater than that of the Wilcox $k-\omega$ model [4]. In addition, Wallin and Johansson [4] demonstrated that their model predicts shock location more accurately than linear two-equation models for the RAE2822 airfoil profile and of the LANN wing.

2.1.1 Equations of the Hellsten EARS K-Omega Model

Equations of the Hellsten EARS $k-\omega$ model can be divided into three categories:

- scale-determining equations derived from Menter's SST,
- constitutive equations determining anisotropy tensor and Reynolds stress tensors taken from WJ-EARSM,
- and lastly the equations that applied on solid wall boundary conditions.

These three categories of equations utilized in the code are given in this section.

2.1.1.1 Scale-Determining Equations of Hellsten

Transport equations for k used in the SST model and Hellsten's EARS $k-\omega$ model are given in Equation (2.1). In this equation, only model coefficients differ for each model.

$$\frac{\partial(\rho k)}{\partial t}+\frac{\partial(\rho\overline{u_j}k)}{\partial x_j}=P-\beta^*\rho\omega k+\frac{\partial}{\partial x_j}\left[(\mu+\sigma_k\mu_t)\frac{\partial k}{\partial x_j}\right] \tag{2.1}$$

In the Equation (2.1), μ is fluid kinematic viscosity, and μ_t is turbulent viscosity (or so called eddy viscosity). Equations for the ω transport differ in terms of both model coefficients and equation sets. The transport equation of ω in the SST model and the Hellsten's model are given in Equations (2.2) and (2.3), respectively.

$$\frac{\partial(\rho\omega)}{\partial t}+\frac{\partial(\rho\overline{u_j}\omega)}{\partial x_j}=\frac{\gamma}{\nu_t}P-\beta\rho\omega^2+\frac{\partial}{\partial x_j}\left[(\mu+\sigma_\omega\mu_t)\frac{\partial\omega}{\partial x_j}\right] + 2\left(1-F_1\right)\frac{\rho\sigma_{w2}}{\omega}\frac{\partial k}{\partial x_j}\frac{\partial\omega}{\partial x_j} \tag{2.2}$$

where, F_1 is the mixing function of Menter. The last term in Equation (2.2) is the cross diffusion term, and in the Hellsten's model, it is modified to be only included when the inner product is positive in order not to include this term in the near-wall.

$$\frac{\partial\left(\rho\omega\right)}{\partial t}+\frac{\partial\left(\rho\overline{u_j}\omega\right)}{\partial x_j}=\boxed{\frac{\gamma\omega}{k}}P-\beta\rho\omega^2+\frac{\partial}{\partial x_j}\left[(\mu+\sigma_\omega\mu_t)\frac{\partial\omega}{\partial x_j}\right] + \boxed{\sigma_d\frac{\rho}{\omega}\max\left(\frac{\partial k}{\partial x_k}\frac{\partial\omega}{\partial x_k},0\right)} \tag{2.3}$$

where, P is the turbulence production term given as in Equation (2.4).

$$P=\tau_{ij}\frac{\partial\overline{u_i}}{\partial x_j} \tag{2.4}$$

The model coefficients such as γ, σ_k, σ_ω, σ_d, can be calculated in solution domain as presented in Equation (2.5).

$$C = f_{\text{mix}} C_1 + (1 - f_{\text{mix}}) C_2 \tag{2.5}$$

In Equation (2.5), C denotes any of the model coefficients, and f_{mix} is the novel mixing function introduced in the Hellsten's model.

Also, Hellsten's mixing function f_{mix} differs from Menter's mixing function, and it is calculated with four different arguments, Γ_1, Γ_2, Γ_3, Γ. The mixing function of Hellsten is designed to be equal to one virtually to edge of the boundary layers and to zero in free turbulent flows.

$$\mathit{\Gamma}_1 = \frac{\sqrt{k}}{\beta^* \omega d} \tag{2.6}$$

$$\mathit{\Gamma}_2 = \frac{500\nu}{\omega d^2} \tag{2.7}$$

$$\mathit{\Gamma}_3 = \frac{20k}{\max\left[\frac{d^2}{\omega}\left(\frac{\partial k}{\partial x_k}\frac{\partial \omega}{\partial x_k}\right), 200k_\infty\right]} \tag{2.8}$$

$$\mathit{\Gamma} = \min\left[\max\left(\mathit{\Gamma}_1, \mathit{\Gamma}_2\right), \mathit{\Gamma}_3\right] \tag{2.9}$$

$$f_{\text{mix}} = \tanh\left(1.5\mathit{\Gamma}^4\right) \tag{2.10}$$

where d is the distance from the nearest wall point, and k_∞ in the Γ_3 calculation given in Equation (2.8) is the user-supplied far-field value of turbulent kinetic energy, k. Far-field value of the turbulent kinetic energy should be a small value, as described by Hellsten [9], and it is taken as 0.01 in the implemented model code. Model coefficients for two different sets, 1 and 2, that are used in scale-determining equations are tabulated in Table 2.1.

Table 2.1: Model coefficients of Hellsten

Set	γ	β	σ_k	σ_ω	σ_d
1	0.518	0.0747	1.1	0.53	1.0
2	0.44	0.0828	1.1	1.0	0.4

2.1.1.2 Constitutive Equations of Hellsten

The explicit algebraic Reynolds stress anisotropy tensor taken from the WJ-EARSM [4] is presented in Equation (2.11).

$$\begin{aligned} a_{ij}^{(ex)} = \beta_3 \left(\Omega_{ik}^* \Omega_{kj}^* - \frac{1}{3} II_\Omega \delta_{ij} \right) + \beta_4 \left(S_{ik}^* \Omega_{kj}^* - \Omega_{ik}^* S_{kj}^* \right) \\ + \beta_6 \left(S_{ik}^* \Omega_{kl}^* \Omega_{lj}^* + \Omega_{ik}^* \Omega_{kl}^* S_{lj}^* - II_\Omega S_{ij}^* - \frac{2}{3} IV \delta_{ij} \right) \\ + \beta_9 \left(\Omega_{ik}^* S_{kl}^* \Omega_{lm}^* \Omega_{mj}^* - \Omega_{ik}^* \Omega_{kl}^* S_{lm}^* \Omega_{mj}^* \right) \end{aligned} \quad (2.11)$$

Nondimensionalized mean strain rate tensor,S_{ij}^*, and mean vorticity rate tensor, Ω_{ij}^*, appeared in Equation (2.11) can be written as in Equations (2.12) and (2.13):

$$S_{ij}^* = \frac{\tau}{2} \left(\frac{\partial \overline{u_i}}{\partial x_j} + \frac{\partial \overline{u_j}}{\partial x_i} \right) \quad (2.12)$$

$$\Omega_{ij}^* = \frac{\tau}{2} \left(\frac{\partial \overline{u_i}}{\partial x_j} - \frac{\partial \overline{u_j}}{\partial x_i} \right) \quad (2.13)$$

Turbulent timescale, τ in Equations (2.12) and (2.13) are computed from the relation in Equation (2.14):

$$\tau = \frac{1}{\beta^* \omega} \quad (2.14)$$

β^* is another model coefficient that equals 0.09 everywhere in the solution space. β coefficients in Equations (2.11) are calculated using the second and fourth order tensor invariants of nondimensionalized mean strain rate and mean vorticity rate tensors. Equations for tensor invariants are presented in Equation (2.15).

$$
\begin{aligned}
II_S &= S^*_{kl} S^*_{lk} \\
II_\Omega &= \Omega^*_{kl} \Omega^*_{lk} \\
IV &= S^*_{kl} \Omega^*_{lm} \Omega^*_{mk}
\end{aligned}
\tag{2.15}
$$

β coefficients that are used in the calculation of explicit algebraic Reynolds stress anisotropy tensor are calculated as given in Equations (2.16).

$$
\begin{aligned}
\beta_1 &= -\frac{N\left(2N^2 - 7II_\Omega\right)}{Q} \quad & \beta_3 &= -\frac{12(IV)}{NQ} \\
\beta_4 &= -\frac{2\left(N^2 - 2II_\Omega\right)}{Q} \quad & \beta_6 &= -\frac{6N}{Q} \qquad \beta_9 = \frac{6}{Q}
\end{aligned}
\tag{2.16}
$$

where denominator Q obtained from Equation (2.17).

$$
Q = \frac{5}{6}\left(N^2 - 2II_\Omega\right)\left(2N^2 - II_\Omega\right) \tag{2.17}
$$

N used in β coefficient calculations is derived from a cubic equation in two-dimensional mean flows. The same equation is also utilized in three-dimensional flows and it is presented in Equation (2.18).

$$
N = \begin{cases}
\frac{A_3'}{3} + \left(P_1 + \sqrt{P_2}\right)^{1/3} + \text{sign}\left(P_1 - \sqrt{P_2}\right)\left|P_1 - \sqrt{P_2}\right|^{1/3} & \text{for} \quad P_2 \geq 0 \\
N = \frac{A_3'}{3} + 2\left(P_1^2 - P_2\right)^{1/6} \cos\left[\frac{1}{3}\arccos\left(P_1 / \sqrt{P_1^2 - P_2}\right)\right] & \text{for} \quad P_2 < 0
\end{cases}
\tag{2.18}
$$

where P_1 and P_2 and $A_3^{'}$ is defined as given in Equations (2.19), (2.20) and (2.21), respectively :

$$
P_1 = \left[\frac{A_3'^2}{27} + \left(\frac{9}{20}\right) II_S - \frac{2}{3} II_\Omega\right] A_3^{'} \tag{2.19}
$$

$$
P_2 = P_1^2 - \left[\frac{A_3'^2}{9} + \left(\frac{9}{10}\right) II_S + \frac{2}{3} II_\Omega\right]^3 \tag{2.20}
$$

$$
A_3^{'} = \frac{9}{5} + \frac{9}{4} C_{\text{diff}} \left[\max\left(1 + \beta_1^{(\text{eq})} II_s, 0\right)\right] \tag{2.21}
$$

where $\beta_1^{(\text{eq})}$ is obtained from Equation (2.22).

$$\beta_1^{(\text{eq})} = -\frac{6}{5}\left[\frac{N^{(\text{eq})}}{\left(N^{(\text{eq})}\right)^2 - 2II_\Omega}\right] \tag{2.22}$$

The values of the constant coefficients $N^{(\text{eq})}$ and C_{diff} taken as in Equation (2.23):

$$N^{(\text{eq})} = \tfrac{81}{20} \quad C_{\text{diff}} = 2.2 \tag{2.23}$$

Finally, Reynolds-stresses are calculated using the Reynolds stress anisotropy tensor found by the constitutive model is presented in Equation (2.24).

$$\tau_{ij} = -\rho\overline{u_i' u_j'} = 2\mu_t\left(S_{ij} - \frac{1}{3}\frac{\partial u_k}{\partial x_k}\delta_{ij}\right) - \frac{2}{3}\rho k\delta_{ij} - a_{ij}^{(ex)}\rho k \tag{2.24}$$

where, eddy viscosity, μ_t, and C_μ are calculated as presented in Equations (2.25) and (2.26).

$$\mu_t = \frac{C_\mu}{\beta^*}\frac{\rho k}{\omega} \tag{2.25}$$

$$C_\mu = -\frac{1}{2}\left(\beta_1 + II_\Omega\beta_6\right) \tag{2.26}$$

2.1.1.3 Wall Boundary Conditions

Far-field boundary conditions are user-specified and are not of great importance because the model does not suffer from freestream sensitivity as opposed to Wilcox's $k-\omega$ models [26, 30]. However, wall boundary conditions must be handled with care. As a typical boundary condition for the $k-\omega$ models, the turbulent kinetic energy at the wall faces must be equal to zero.

$$k_{wall} = 0 \tag{2.27}$$

However, the treatment of the ω boundary condition is somewhat complicated. The current ω wall boundary condition approach is based on the rough wall boundary condition method of Wilcox [26, 30] presented in Equation (2.28).

$$\omega_{wall} = \frac{u_\tau^2 S_R}{\nu} \tag{2.28}$$

As a nondimensional function, S_R is described as given in Equation (2.29).

$$S_R = \begin{cases} \left[\frac{50}{\max\left(k_s^+, k_{s,\min}^+\right)}\right] & \text{for} \quad k_s^+ < 25 \\ \frac{100}{k_s^+} & \text{for} \quad k_s^+ \geq 25 \end{cases} \tag{2.29}$$

where k_s^+ is calculated from sand roughness, k_s, that is specified for rough walls. Calculation of k_s^+ is given in Equation (2.30).

$$k_s^+ = \frac{k_s}{u_\tau \nu} \tag{2.30}$$

where, friction velocity u_τ is obtained from wall shear stress, τ_w, and from the fluid density.

$$u_\tau = \sqrt{\frac{\tau_w}{\rho}} \tag{2.31}$$

$k_{s,\text{min}}^+$ is used for smooth walls and it can be calculated as presented in Equation (2.32):

$$k_{s,\text{min}}^+ = \min[4.3(y_w^+)^{0.85}; 8] \tag{2.32}$$

y_w^+ appear in Equation (2.32) is nondimensional wall distance, which is obtained by Equation (2.33):

$$y_w^+ = \frac{y u_\tau}{\nu} \tag{2.33}$$

2.2 CFD Solver

All model equations and boundary conditions are utilized in an open-source solver flowPsi, developed by Luke et al. [57]. This solver is an unstructured, cell-based, compressible finite volume CFD solver that uses a rule-based programming language LoCi. The entire solution is a series of rules that are scheduled in the LoCi framework and fully parallelized in MPI during execution. This strategy simplifies the development of high-performance parallel programs. The code is written in a LoCi-specific language that is translated to C++ during compilation.

All analyses are conducted utilizing the default flux-schemes and limiters. Utilized inviscid flux scheme is the second order accurate HLLC developed by Toro et al. [58] with the Venkatakrishnan limiter. In addition, preconditioning is applied to flow problems with a Mach number of less than 1.

flowPsi already supplies widely utilized RANS models for aerodynamic applications. The turbulence models consist of one-equation model of Spalart-Allmaras [18], several versions of Wilcox $k - \omega$ models [30], and the BSL and SST models of Menter et al. [32].

CHAPTER 3

RESULTS & DISCUSSION

Results of different test cases are provided in this chapter in comparison with experimental and numerical data available in the literature. In addition, results obtained from the solution of each case are discussed.Test cases are selected for different purposes:

- Zero pressure gradient flat plate test case is selected to verify the model implementation and validate the model on the fundamental turbulence test case.
- Driver's separated boundary layer under adverse pressure gradient is selected to verify the model implementation and the model validation in separating flows under adverse pressure gradient.
- Separating flow over NACA4412 case is chosen to verify the model implementation with the results of Hellsten [8]. The results also compared with a different flow solver, CFD++, equipped with the same model. Also, the effects of wall boundary conditions and the model validation are studied in this case.
- Transonic flow over RAE2822 airfoil profile is studied to assess the model's performance on transonic aerodynamic problems.
- Transonic flow over an axisymmetric bump is one of the fundemental test cases to assess turbulence model performance. The model is selected to validate the model in wall-bounded transonic flow conditions and verify the model implementation in axisymmetric cases.
- NASA Tandem Control Missile (TCM) case is being studied to assess the model on 3D supersonic aerodynamic flows involving high AOA aerodynamics.

Table 3.1: Flat plate grids statistics

Grid name	Nodes on domain	Nodes on wall	Cell numbers	y^+
Grid 1	35 x 25	29	816	1.3
Grid 2	69 x 49	57	3264	0.74
Grid 3	137 x 97	113	13056	0.46
Grid 4	273 x 193	225	52224	0.24
Grid 5	545 x 385	449	208896	0.14

- Fin trailing vortex case is studied in order to observe whether implementation of EARSM improves the capability of vortex modeling compared to the SST.

3.1 Zero Pressure Gradient Flat Plate

Five different grids are used for a grid convergence study conducted for the zero pressure gradient boundary layer over a flat plate case. These grids are taken from the "Turbulence Modeling Resource" of NASA [59]. Boundaries and computational grid of a solution domain for the medium grid (Grid 3) are given in Figure 3.1. The inlet of a domain is modelled as an isentropic inlet in which turbulent kinetic energy, k, specific dissipation rate, ω, total pressure, and total temperature values are specified as inputs. The top line of a 2D domain is modelled as a farfield boundary condition, and Mach number, static temperature, and static pressure are supplied in addition to turbulence properties. The outlet is modelled as a pressure outlet on which static pressure is equal to the pressure of the farfield. The flat plate wall is modelled as a viscous wall with a no-slip boundary condition. The Mach number at the inlet is 0.24, and the Reynolds number at the end of the flat plate is $1.14 * 10^7$.

Node numbers on the flat plate and on the whole solution domain in streamwise and normal directions with the maximum y^+ value along the first cells adjacent to the wall are provided for each grid in table 3.1. Note that even the coarsest grid has a maximum y^+ value of 1.3, which shows that even the coarsest grid can be used without including wall functions in the solution.

In this section, EARSM results of boundary layer with a zero pressure gradient flat

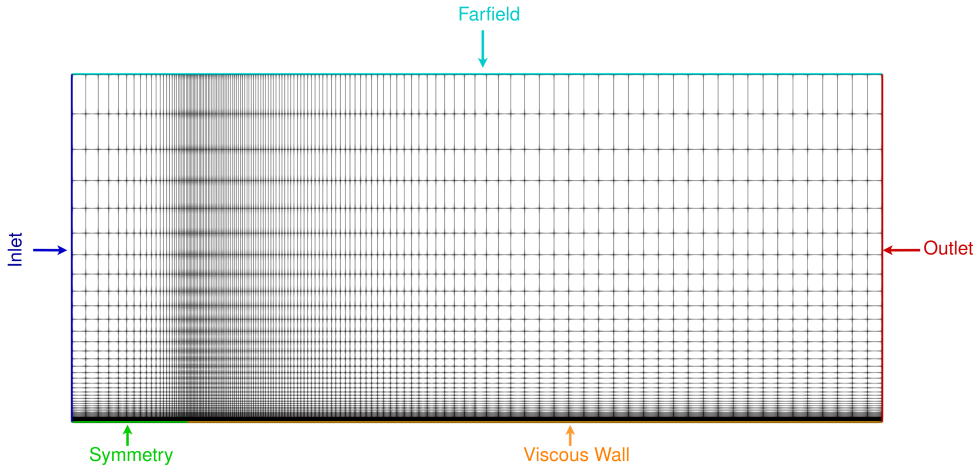

Figure 3.1: Flat plate solution domain of medium grid

plate are presented with numerical data of Hellsten [8] and experimental data of Klebanoff [5], Winter and Gaudet [6], and Wieghardt [7]. Also, the grid independence results of a flat plate is presented. It should be noted that the grid convergence study was carried out for both the SST and the Hellsten EARS $k-\omega$ model written in flowPsi, but only the latter results are presented. Figures 3.2 and 3.3 show the skin friction distribution along the flat plate and the velocity profile of the boundary layer at location $\mathrm{Re}_x = 4.2 * 10^6$. It can be understood from these figures that a solution becomes grid independent starting from the medium grid (Grid 3). The solution still changes slightly after the Grid 3 is refined. However, the change is not significant.

Results for the model verification and validation are given in Figures between 3.4 and 3.6. To verify the code implementation, results of Hellsten et al. [8] with the same turbulence model are presented. When the skin friction distribution along the flat plate is considered, it is concluded that results obtained from flowPsi and Hellsten's results are in good agreement with each other. Furthermore, when compared to flowPsi SST results, results of flowPsi EARSM and of Hellsten et al. [8] give higher skin friction distributions that are closer to experimental data of Wieghardt [7], Winter and Gaudet [6], and Klebanoff [5]. In addition, velocity profiles in the boundary layer at position $\mathrm{Re}_x = 4.2 * 10^6$ are closer to the experimental data of Wieghardt [7] and Klebanoff [5] for EARSM results obtained with flowPsi and Hellsten's results. Lastly, the momentum thickness, δ_2, along the boundary layer is presented in Figure 3.6. Momentum thickness at a position can be calculated as given in Equation (3.1):

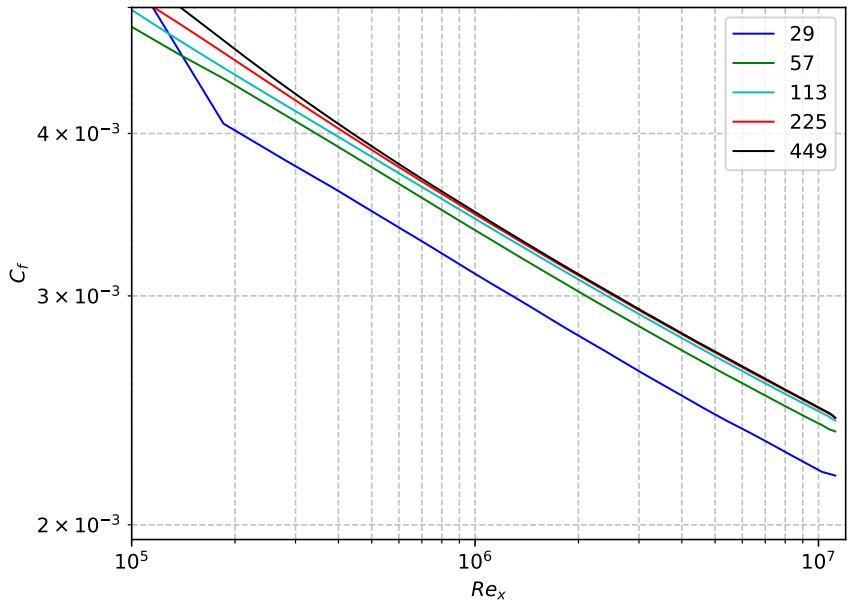

Figure 3.2: Flat plate skin friction distribution for grid convergence

$$\delta_2 = \int_0^\infty \frac{U}{U_\infty}(1 - \frac{U}{U_\infty})dy \tag{3.1}$$

Momentum thickness distribution along the plate is more inline with the experimental data of Wieghardt [7] compared to SST results and results of Hellsten [8]. Also, momentum thickness shows more linear distribution in comparison with Hellsten [8]. This can be due to the grid distribution on the plate near the trailing edge or solver differences such as flux scheme differences. However, when all results are considered, the results of flowPsi and Hellsten [8] with the same turbulence model agree very well. All differences can be treated as a result of grid difference and solver difference, noting that Hellsten used 137 nodes on flat plate parallel direction. When flowPsi SST results are investigated, it can be stated that the SST provides a lower skin friction distribution and agrees less with experimental data than Hellsten EARS $k-\omega$ results.

3.2 Driver's Separating Boundary Layer Under Adverse Pressure Gradient

The second test case for the validation of the turbulence model is the Driver's separated boundary layer under an adverse pressure gradient experiment [60]. The case

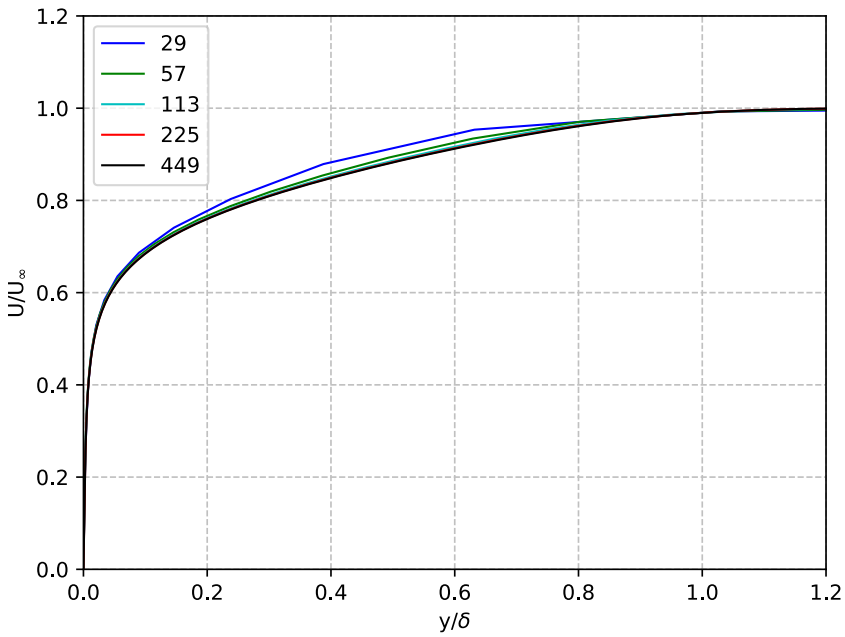

Figure 3.3: Flat plate velocity profile in a boundary layer at $\mathrm{Re}_x = 4.2 * 10^6$ for grid convergence

C of the Driver's experiment is studied since it is the only case involving a separated turbulent boundary layer. The experiment was conducted on a cylinder with a diameter of 0.14 m. As can be seen from Figure 3.7, the outer wall of the test section is diverged to impose an adverse pressure gradient strong enough to cause separation. A separation bubble is observed in the experiment and has a length of approximately 0.2 m. This case will be beneficial to assess the capability of the Hellsten's model to predict separation and to model the flow physics of adverse pressure gradients, which appear frequently in high-lift aerodynamic flows. The present case is also widely studied by other researchers to validate different turbulence models [31, 32, 42, 8].

The solution domain of the test case is presented in Figure 3.8. Note that the case is modelled as a 2D axisymmetric problem. The inlet has a Reynolds number of 2.8×10^5, in which the characteristic length is taken as a cylinder diameter of 0.14 m and has a Mach number of 0.08812. Therefore, the case can be considered as an incompressible flow problem. The lower edge of the domain after the inlet is modelled as a symmetry axis with a length of 0.3 m. After the axis boundary condition, a solid viscous wall boundary condition is applied until the outlet, which has a length of 2.6 m. The upper edge of the solution domain has an inviscid no-slip boundary condition

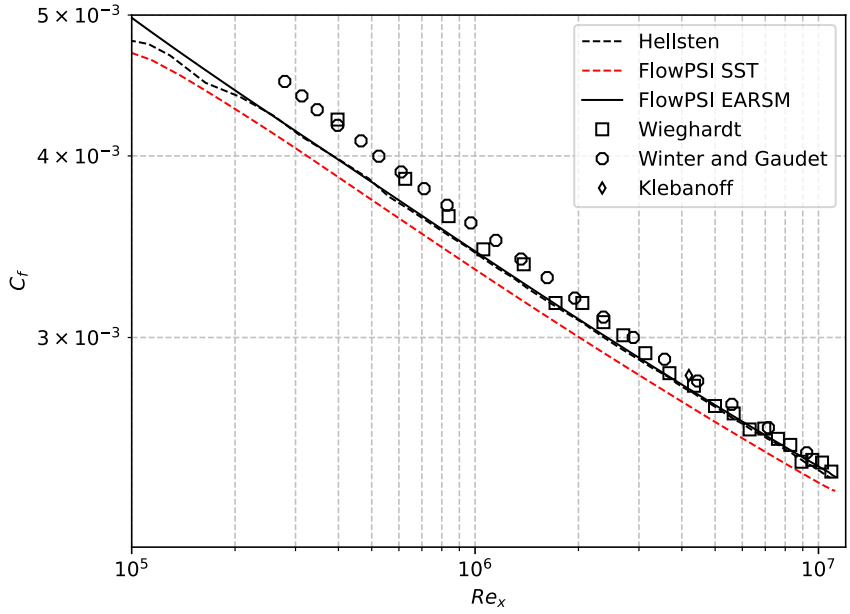

Figure 3.4: Flat plate skin friction distribution with experimental data of Klebanoff, Winter and Gaudet, and Wieghardt and numerical results of Hellsten [5, 6, 7, 8]

to accurately model the streamlines of Driver's experiment [8]. The computational grid is selected as the finest grid provided on NASA's turbulence modelling website [59]. The grid has 1425 nodes in the axial flow direction and 385 nodes in the normal direction and has a maximum y^+value of 0.19 on the solid wall. The finest grid is utilized to ensure the grid independence.

The results of the Driver's separating boundary layer under the adverse pressure gradient are presented in this section. Velocity contour with streamlines and turbulent viscosity ratio contours are given in Figures 3.9a and 3.9b, respectively. The contours are obtained from the results of the Hellsten EARS $k - \omega$ model. The SST model results are not presented because the differences of these results cannot be observed clearly from the contours. Figure 3.9a shows that flow is separated as the wall is enlarging and starts to reattach after the wall is converging to its initial position. From the viscosity ratio contour, it can be said that the turbulent viscosity is up to 890 times higher than the fluid viscosity. Hence,viscous effects are dominant in this flow problem and it would be a proper illustrative test case for the turbulence models.

In order to investigate the results of different turbulence models, firstly pressure coefficient is plotted and presented in Figure 3.10. It is also aimed to observe model

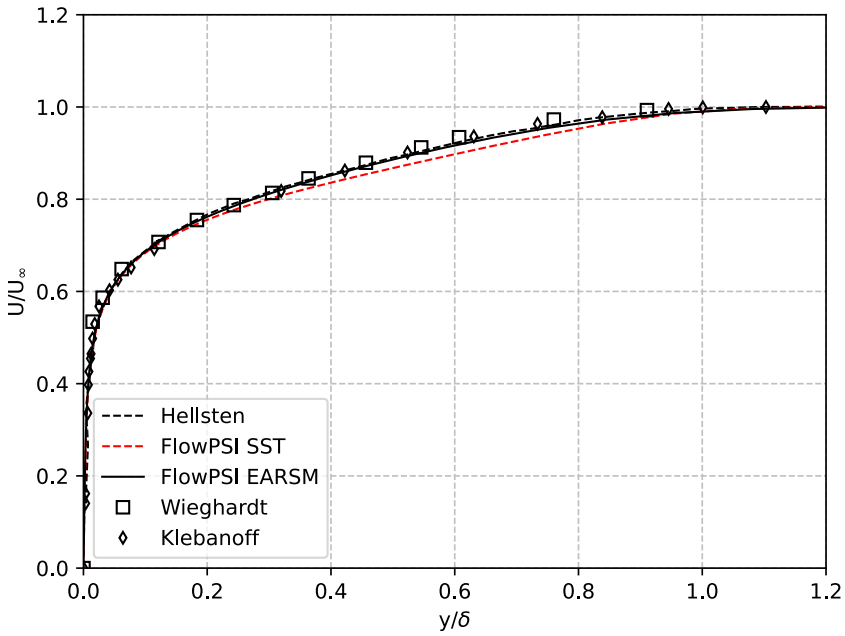

Figure 3.5: Flat plate velocity profile in a boundary layer at $\mathrm{Re}_x = 4.2 * 10^6$ with experimental data of Klebanoff, and Wieghardt and numerical results of Hellsten [5, 7, 8]

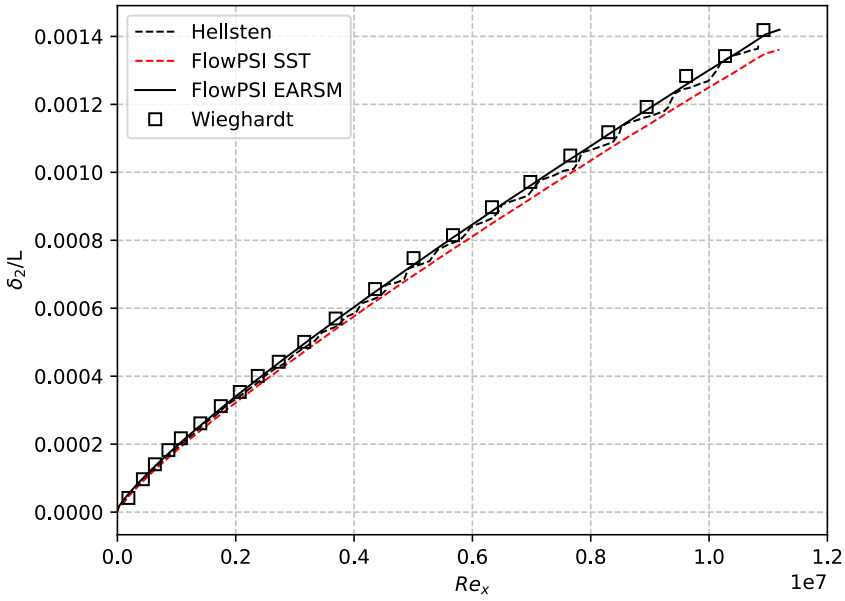

Figure 3.6: Momentum thickness along the flat plate with experimental data of Wieghardt and numerical results of Hellsten [7, 8]

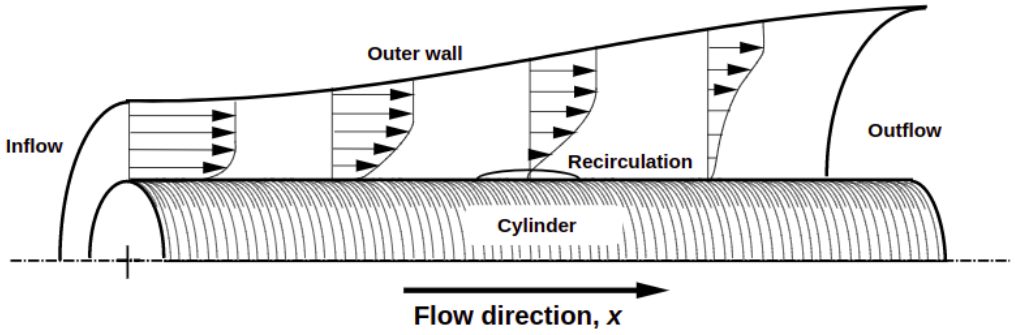

Figure 3.7: Driver's separating boundary layer test setup

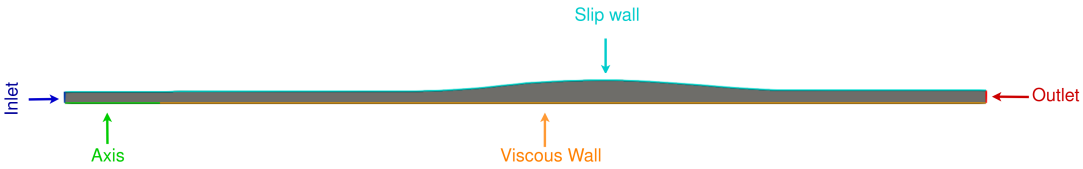

Figure 3.8: Driver's separating boundary layer solution domain

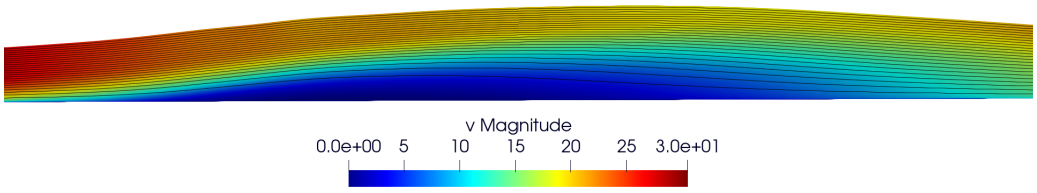

(a) Velocity contour with streamline

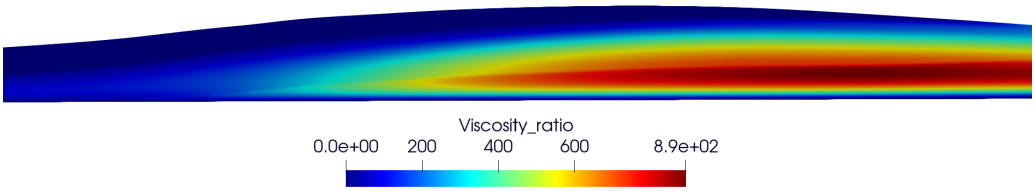

(b) Turbulent to fluid viscosity ratio contour

Figure 3.9: Velocity contour with streamlines 3.9a and turbulent to laminar viscosity ratio 3.9b of Driver's separating boundary layer case

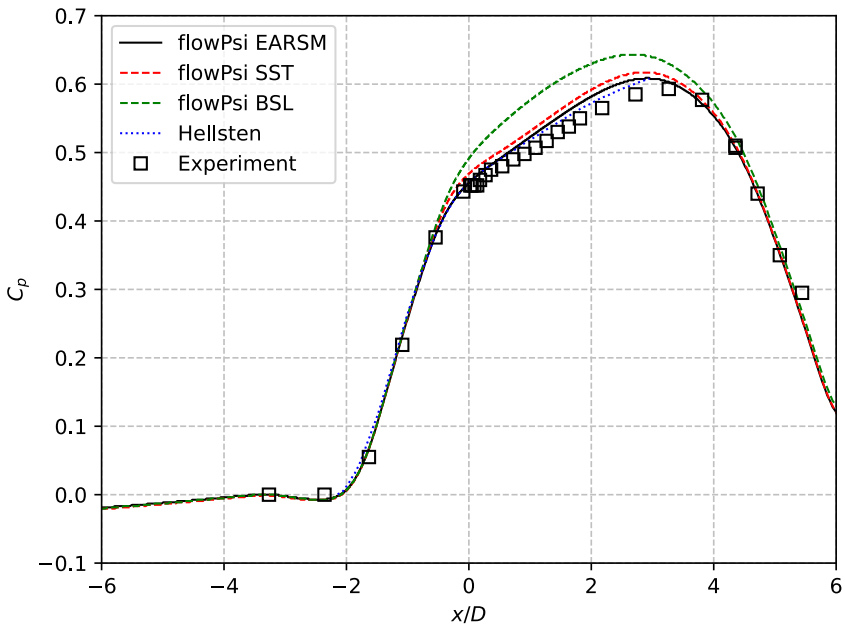

Figure 3.10: Pressure coefficient obtained with flowpsi and presented in Hellsten et al. [9] along the wall of Driver's separated boundary layer case

is implemented correctly on our solver. For this reason, Hellsten's results [9] presented with the experimental data are shown. Note that, our results are obtained such that reference pressure is taken as pressure on the wall at location $x/D = -2.857$, $P_{ref} = P_{x/D=-2.857}$, in the calculation of the pressure coefficient. When Figure 3.10 is considered, it can be stated that the Hellsten EARS $k - \omega$ model, when compared to the SST and the BSL models, produces results that are closer to the Driver's experiment [60]. Also, it can be concluded that the BSL model predicts higher pressure loss inside the separation. Moreover, since both the SST and the BSL predict higher pressure loss than the EARSM, it can be said that the constitutive model is important in this flow problem. Since the results of flowPsi EARSM and the results of Hellsten et al. [9] exhibit similar behavior in terms of pressure coefficients, it can be taken as evidence that the model is implemented accurately into the solver.

Another important indicator of the model validation is the skin friction coefficient distribution along the wall, which is presented in Figure 3.11 with the results of Hellsten et al. [9]. As can be seen from Figure 3.11 that, the EARSM and the BSL models predict higher skin friction upstream of the separation compared to experiment and the results of the SST. This higher skin friction delays the separation location and

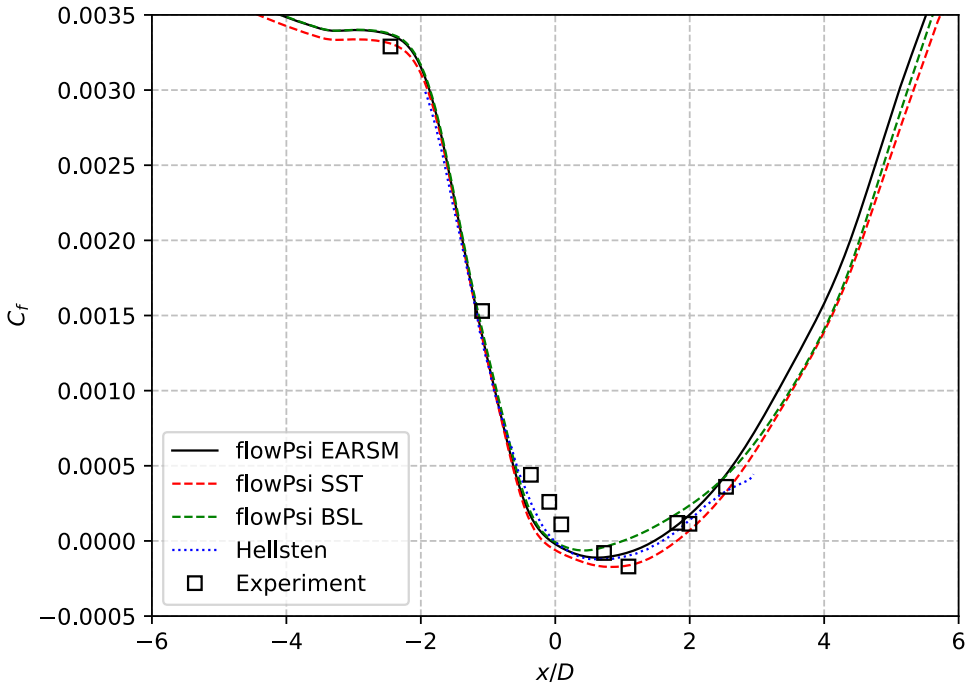

Figure 3.11: Skin friction coefficient distribution along the wall of cylinder for Driver's case

decreases the separation length. All models predict the separation location upstream of the experiment, and the length of the separation bubble differs for each model. The BSL model predicts the separation location upstream and reattachment region downstream of the presented models, and it predicts the lowest magnitude of skin friction along the backflow region. This result indicates that the BSL model has the lowest sensitivity to adverse pressure gradients. The EARSM finds separation and reattachment locations downstream of the SST prediction. The distribution of skin friction with EARSM, along the reattachment and recovery regions is closer to the experiment. Moreover, both the results of Hellsten and of the implemented model are in nearly perfect agreement with each other. Small discrepancies can be considered as a result of grid resolution since Hellsten utilized a 160×96 grid, and our analyses were performed on a 1425×385 grid. The results of the present study can be considered the grid-independent solution of Hellsten.

Velocity profiles of different locations along the cylinder surface, including the regions before and after the separation, are presented in Figures 3.12a and 3.12b. In Figure 3.12a it can be seen that all models predict velocity profiles nearly the same

and very close to the experimental measurements on the first three stations. However, SST and BSL models predict a very sharp velocity profile near the outer edge of the boundary layer, in contrast to the Hellsten's model, which gives a smoother profile closer to the experiment. As Figure 3.12b is considered, it can be said that Menter's SST model predicts stronger backflow near the wall, which is in better agreement with experimental data compared to Hellsten's model. Although Hellsten's model predicts weaker backflow near the cylinder wall, the effect of the adverse pressure gradient is captured accurately enough away from the wall. However, it can be seen from both figures that the BSL model does not predict the separation and backflow along the boundary layer. These results can indicate that the transport of principal Reynolds shear stress accounted for with the SST and the EARSM can lead to significant improvement in modelling the adverse pressure gradient flow problems compared to other two-equation models. Note that Menter calibrated the SST model with this flow problem. This fact is the reason for the perfect agreement of velocity profiles of SST model solution with the experiment.

Figure 3.13 depicts the Reynolds shear stress distribution at the same positions perpendicular to the wall. Only the results of Hellsten's model implemented in flowPsi are given with the experiment data. This is because the original SST code should be modified to obtain Reynolds shear stresses, which is avoided in the present study. When Reynolds shear stresses are taken into account, the Hellsten EARS $k-\omega$ model produces nearly identical results to the experiment before the separation. However, the Hellsten's model gives slightly higher shear stresses in the separation and lower shear stresses in the reattachment region away from the wall. Although the Reynolds shear stresses do not match well with experiments away from the wall, Hellsten's results are in strong agreement with experiment close to the wall at every location.

3.3 Separating Flow Around NACA4412 Airfoil

Flow around a NACA4412 airfoil at 13.87° angle of attack is studied and compared with experimental results of Coles and Wadcock [10] as a third validation case. Reynolds number per airfoil chord is 1.52 million, and incoming flow has a Mach number of 0.09, so the flow problem is incompressible. The solution domain of the

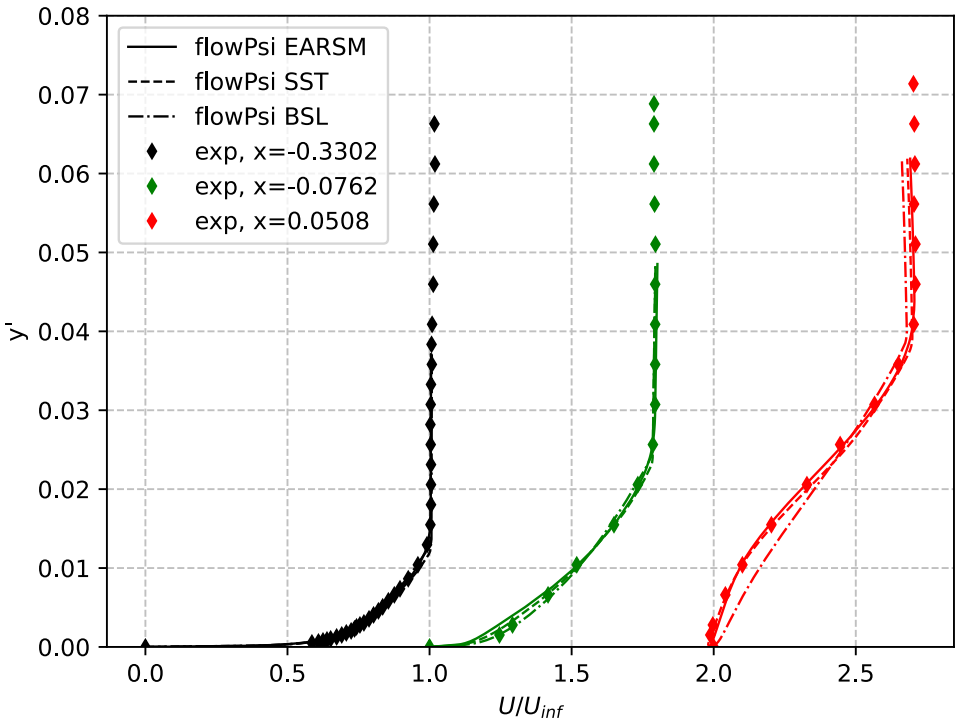

(a) First three stations

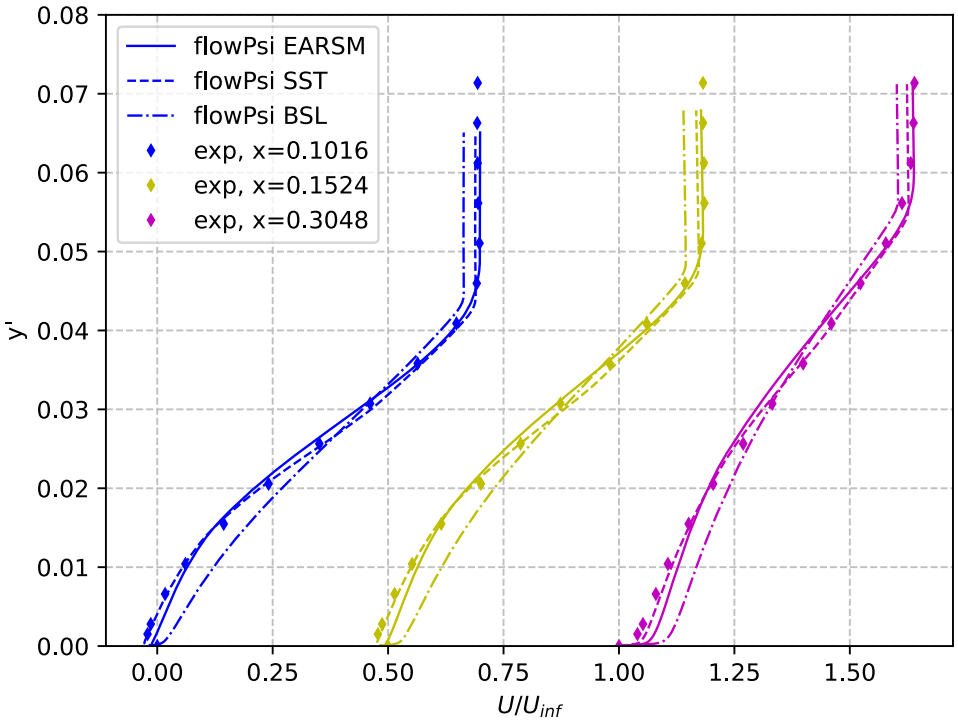

(b) Last three stations

Figure 3.12: x-velocity profiles in a boundary layer of different x-locations for Driver's case 3.12b

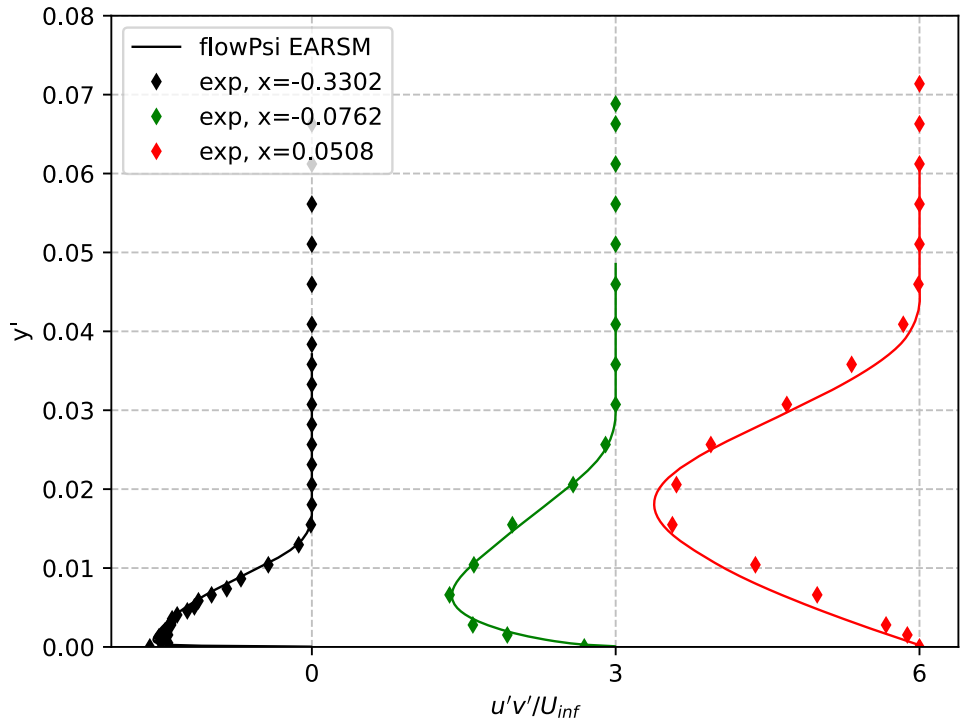

(a) First three stations

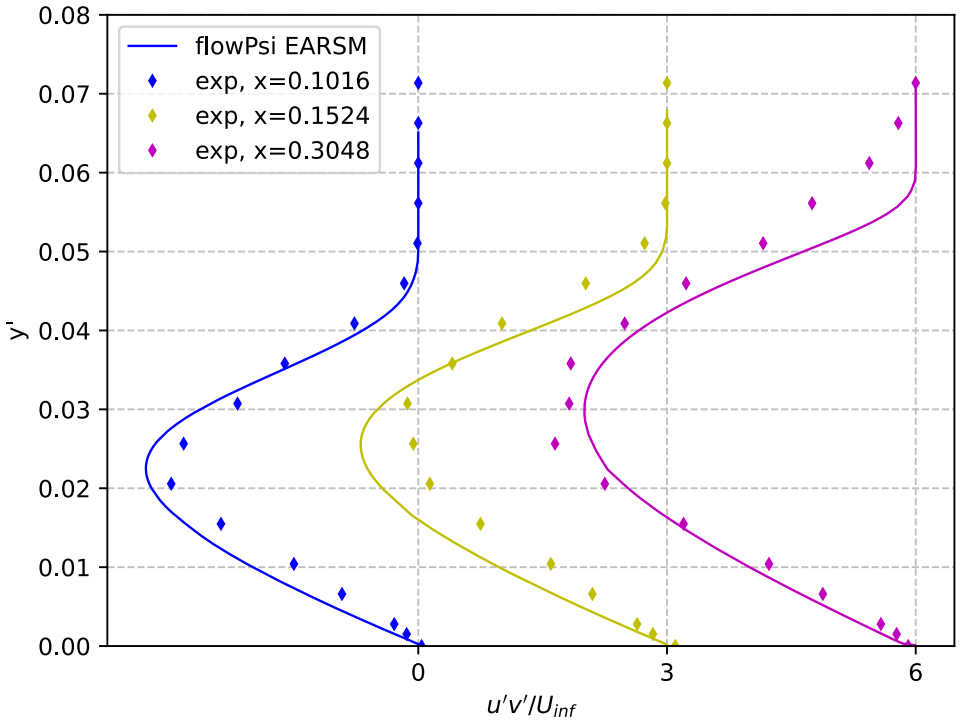

(b) Last three stations

Figure 3.13: Reynolds shear stress profiles in a boundary layer of different x-locations for Driver's case

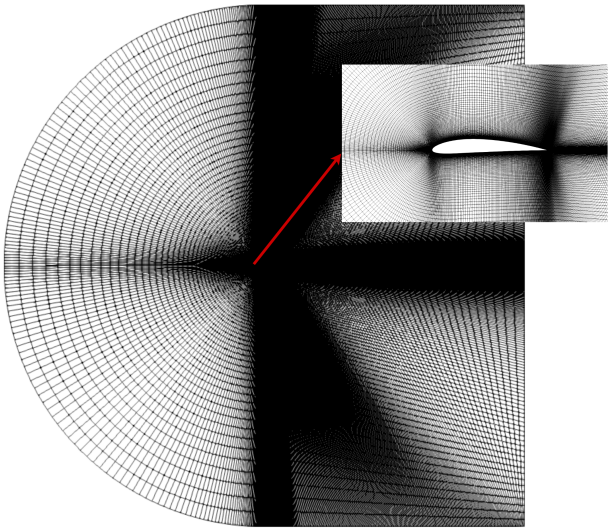

Figure 3.14: NACA4412 solution domain of Grid 4

NACA4412 case of Grid 4 is presented in Figure 3.14. Although the experimental test section has walls, it is not modelled in the solution. Instead of modelling the test section walls, the farfield is modelled, which extends up to 100 chord lengths in all directions. The upper and lower walls of the airfoil are modelled as viscous no-slip walls.

Also, a grid independence study is conducted for the present test case. Five different C-grids taken from NASA's turbulence modeling website are utilized, and the results of different grids are presented. As can be seen from Figure 3.14 that, domain is reasonably far away from the airfoil walls to obtain accurate results of free flight conditions. Node numbers of the whole domain, of the walls and total cell numbers with maximum wall y^+ are presented in Table 3.2. It can be said that maximum wall y^+ are low enough not to utilize wall functions in a solution, especially starting from the medium grid (Grid 3).

In this section, results obtained with different grids, turbulence models, and flow solvers are presented for flow around NACA4412 airfoil at 13.87° angle of attack. Although the experimental results of Coles and Wadcock are considered questionable by many researchers, NACA4412 airfoil flow is selected as another validation case since it has been studied by many researchers, including Menter and Hellsten [31, 32, 42, 8]. Studies conducted for this test case can be divided into four main categories. Firstly, a grid independence study was conducted. Secondly, model ver-

Table 3.2: NACA4412 grids statistics

Grid name	Nodes on domain	Nodes on wall	Cell numbers	y^+
Grid 1	113 x 33	65	3584	3.1
Grid 2	225 x 65	129	14336	1.7
Grid 3	449 x 129	257	57344	0.92
Grid 4	897 x 257	513	229376	0.45
Grid 5	1793 x 513	1025	917504	0.22

ification is studied by comparing the results of Hellsten et al. [8] with the results of flowPsi utilizing the Hellsten's model. Thirdly, the effect of the ω wall boundary condition as well as the results of another flow solver named CFD++ was studied. Finally, Hellsten's model validation study is conducted by comparing the results of the implemented model with the results of the SST model and with the results of the experiment.

The grid convergence study is performed using the Hellsten EARS $k-\omega$ model with solvers flowPsi and CFD++, as well as the SST model in flowPsi, based on the lift and drag coefficients of the airfoil. Because three different solutions produce the same grid convergence results, only the results obtained with flowPsi using the Hellsten EARS $k-\omega$ model are presented in Table 3.3. As can be seen from Table 3.3, the lift coefficient, C_L, becomes grid independent starting from Grid 3. However, the drag coefficient, C_D, changes until Grid 4. Therefore, the grid-independent solutions are achieved starting from Grid 4, and this grid is utilized in all CFD solutions presented in this section. Moreover, time-dependent effects are observed with both turbulence models in terms of coefficients and flowfield data as the grid is refined after the Grid 3. Steady solutions are obtained only with very time-consuming, very small time step solutions, such as $1e^{-6}$ time step with 60000 iterations.

Figure 3.15 shows the contours obtained from the flowPsi solver results with the Hellsten EARS $k-\omega$ model. When velocity contours and streamlines around the airfoil presented in Figures 3.15a and 3.15b are considered, it can be seen that flow separates near the trailing edge of the airfoil. Separated flow has a large extent, and it has a strong backflow. As the turbulent viscosity ratio presented in Figure 3.15c

Table 3.3: NACA4412 grid convergence results of flowPsi with EARSM

Grid name	Nodes on domain	Cell numbers	C_L	C_D
Grid 1	113 x 33	3584	1.45	0.085
Grid 2	225 x 65	14336	1.51	0.045
Grid 3	449 x 129	57344	1.55	0.038
Grid 4	897 x 257	229376	1.55	0.035
Grid 5	1793 x 513	917504	1.55	0.035

Table 3.4: NACA4412 aerodynamic coefficients from different solvers, turbulence models and experiment

Solver-experiment	Turbulence Model	C_L	C_D
flowPsi	EARSM	1.55	0.035
flowPsi	SST	1.61	0.033
flowPsi	EARSM BC 2.4	1.56	0.035
CFD++	EARSM	1.57	0.034
FINFLO [8]	EARSM	1.67	0.039
Experiment	-	1.67	-

shows, the viscous effects are dominant around the airfoil, especially near the trailing edge.

All results of this study using different solvers and turbulence models are presented in Table 3.4, along with the results of Hellsten et al. [8] and experimental results of Coles and Wadcock [10].

3.3.1 Implementation Verification

Following the grid convergence study, the Hellsten EARS $k-\omega$ model results are compared with Hellsten's results with the same model and the experiment to verify the model implementation [8, 10]. When the drag and lift coefficients of the airfoil, presented in Table 3.4, are considered. The lift coefficient found by Hellsten is in excellent agreement with the experiment. However, the EARSM implemented

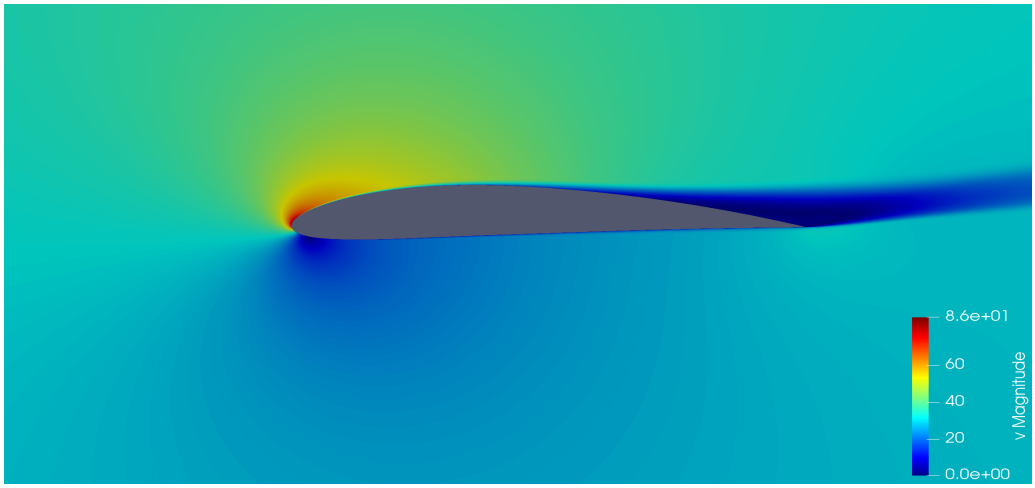

(a) Velocity contour

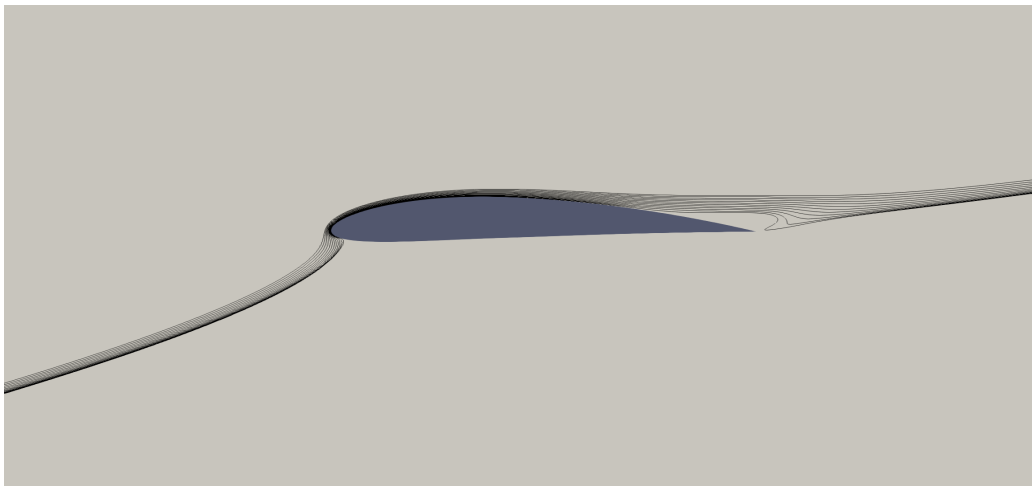

(b) Streamlines

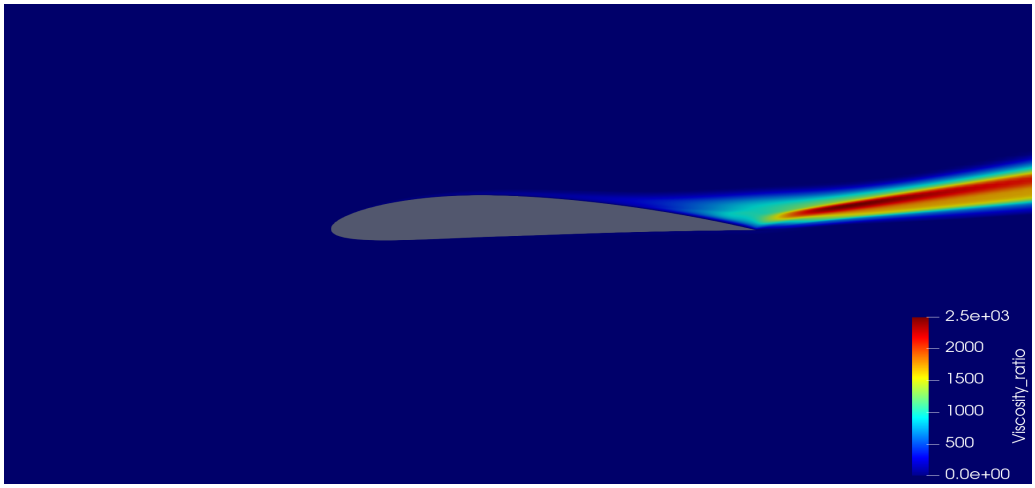

(c) Turbulent to fluid viscosity ratio contours

Figure 3.15: Velocity contours 3.15a, streamlines over the upper surface 3.15b, and turbulent to fluid viscosity ratio contours 3.15b of NACA4412 airfoil

in flowPsi predicts a lower lift coefficient. Although experimental data on the drag coefficient is not available, there is a difference between the Hellsten's results and the results of flowPsi.

In order to further investigate the implementation verification, velocity profiles in the x-direction for different locations, including downstream and inside the separation region, are presented in Figure 3.16. Velocity profiles of these locations are extracted on the lines perpendicular to the upper wall. These profiles are obtained with a reference of x-velocity at a location one chord below and behind the trailing edge of the airfoil, which is slightly different from the generally used far-field velocity. The reference x-velocity is approximately equal to 0.93 of the farfield velocity ($U_{ref} = 0.93U_{\infty}$). As illustrated in Figure 3.16 Hellsten's results, provided for five different locations, are more in line with the experimental data compared with the flowPsi EARSM results. The only significant difference observed in x-velocity profiles was in the near wall region at stations 5 and 6. These results show that this case needs further investigation to provide information about implementation verification and the reliability of Hellsten's results.

3.3.2 Effects of Flow Solver and Wall Boundary Conditions

In order to be sure that model implementation is done properly, a commercial CFD solver CFD++ equipped with the Hellsten's model was utilized in this study. As can be seen from Table 3.4, the results of CFD++ are closer to the results of flowPsi with the same model, compared with the results of Hellsten et al. [8].

It is observed during the validation study that the model implemented in flowPsi and CFD++ utilizes different ω wall boundary conditions based on different publications by Hellsten [8, 9]. In this thesis, the wall boundary condition presented in Section 2.1.1.3 is utilized, which is introduced in the model paper of Hellsten et al. [9]. However, CFD++ utilizes the boundary condition presented in the thesis of Hellsten, presented in 2004 [8]. The only differences between these boundary conditions are the calculation of minimum sand roughness scaled by the viscous length scale, $k^{+}_{s,\text{min}}$. The minimum sand roughness calculation in the implemented code is given in Equation (2.32), and the calculation in CFD++ can be written as in Equation (3.2).

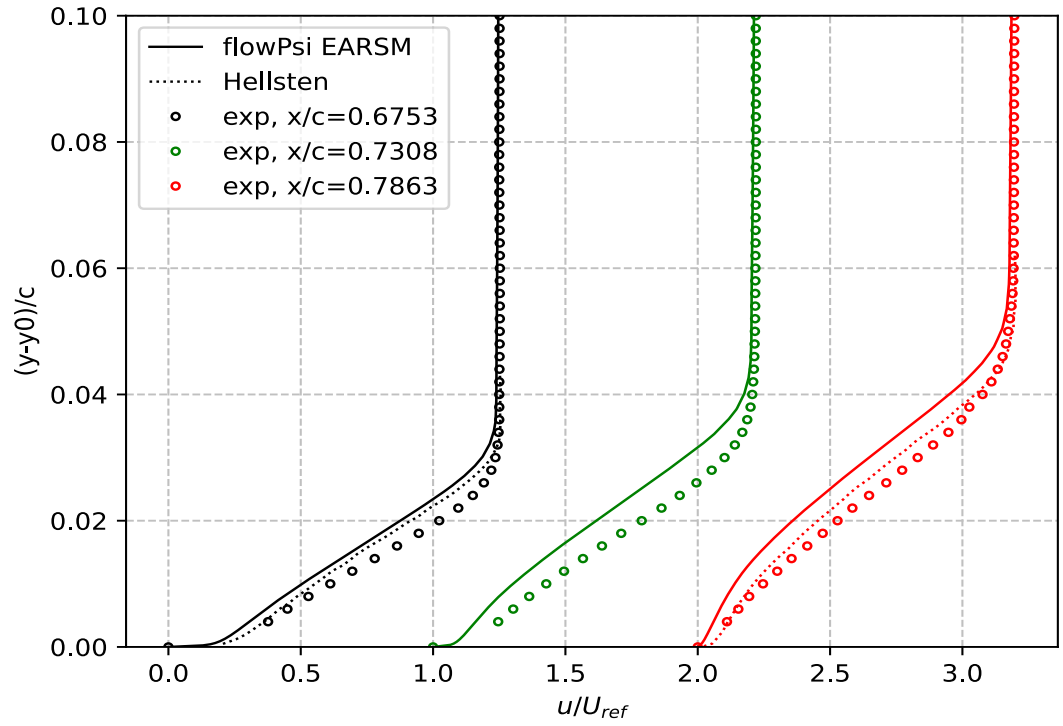

(a) First three stations

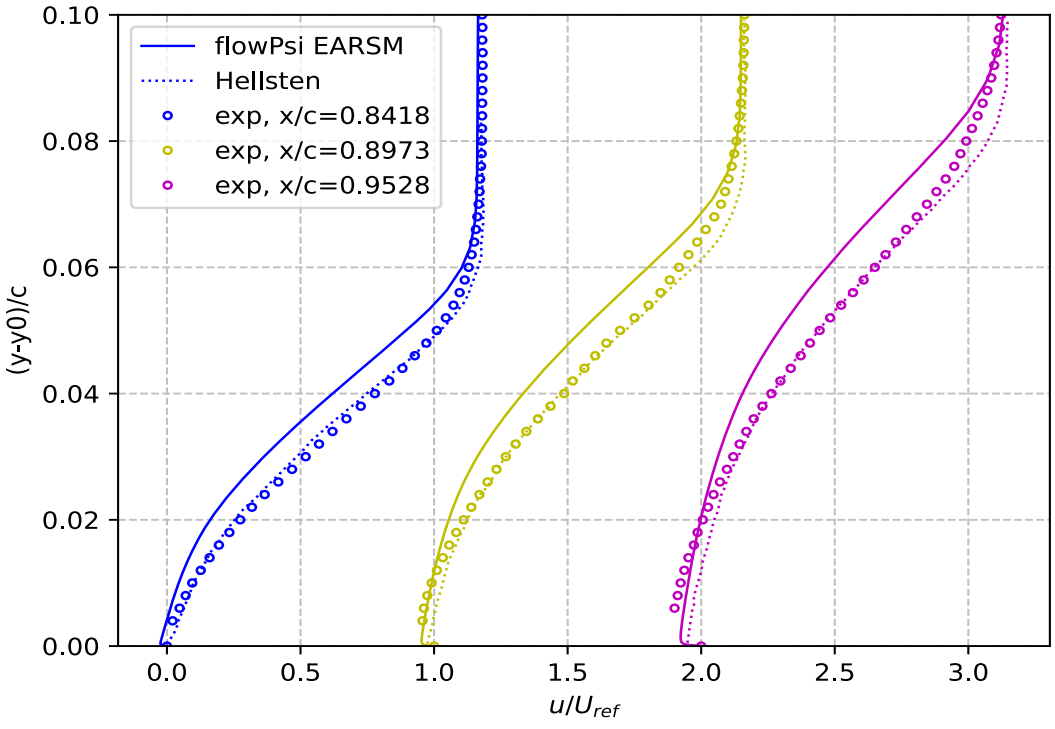

(b) Last three stations

Figure 3.16: x-velocity profiles in a boundary layer of different x-locations for flowPsi EARSM with the results of Hellsten and the experiment [8, 10]

$$k^+_{s,\text{min}} = \min[2.4(y^+_w)^{0.85}; 8] \tag{3.2}$$

Note that only the multiplication of y^+_w changed from 4.3 to 2.4 between the solvers. In order to verify that the differences in the results between CFD++ and flowPsi are only due to the differences between the flow solvers, the wall boundary condition presented in Equation (3.2) is implemented into flowPsi, and the flow problem is solved again. Results obtained with this implementation are referred to "EARSM BC 2.4" in the results presented in the tables and figures in this section. The aerodynamic coefficient prediction of flowPsi with ω wall boundary condition of CFD++ lies between the results of CFD++ and studied EARSM in flowPsi. However, all three results do not significantly differ from each other.

In order to compare the results based on data other than the aerodynamic coefficients, pressure coefficient distributions along the upper and lower walls of the NACA4412 airfoil with different EARSM solutions are presented in Figure 3.17. As can be understood from the figure, all models provide nearly the same pressure distribution along both lower and upper walls. All models predict a higher pressure coefficient distribution compared to the experiment. Since the differences between EARSM solutions cannot be seen clearly from the figure, they are not considered.

The x-velocity profiles at the same stations, presented in Figure 3.16, are plotted for the EARSM results of different flow solvers with different wall boundary conditions and are shown in Figure 3.18. Figure 3.18 contains the results obtained from the Hellsten EARS $k-\omega$ model in two different solvers, flowPsi and CFD++, as well as experimental data of Coles and Wadcock [10]. When these figures are examined, the first observation is that EARSMs results are similar in terms of x-velocity in the boundary layer. There is only a slight difference between the results obtained with CFD++ and those obtained with the same wall boundary conditions utilized in flowPsi. Results of flowPsi with CFD++ ω wall boundary conditions are closer to the results obtained with CFD++ compared with the results obtained with Hellsten's boundary condition revealed in 2005, especially in the near wall region [9]. The small differences between the two solvers with the same boundary conditions can be thought of as a result of the differences between the flow solvers.

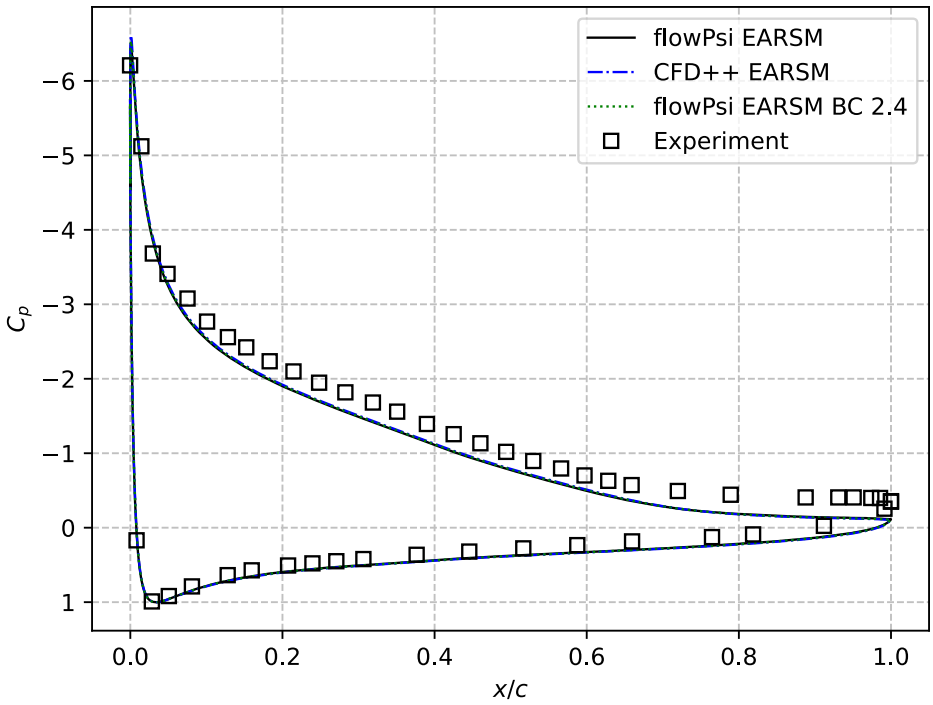

Figure 3.17: Pressure coefficient distribution along the NACA4412 airfoil profile for flowPsi EARSM with the results of Hellsten and the experiment [8, 10]

The y-velocity profiles at the same locations are also plotted and presented in Figure 3.19. The same behavior seen in the x-velocity profiles of different flow solvers is observed again. However, deviation from the experiment is significant this time. Results from Hellsten are not presented for y-velocity profiles since they are not provided in papers. However, the consistency between the results of flowPsi and CFD++ shows that the model is implemented correctly. This might be due to two reasons. The first may be that, as Hellsten implied, his solution may not have reached grid independency, and grid resolution used in his studies [8, 9] pheonemena may not be sufficiently fine to capture separated flows accurately. Another reason could be that Hellsten's results were much more dependent on the flow solver, FINFLO. For these reasons, no meaningful conclusions can be made from the results of Hellsten. One should always be aware that the results from flowPsi and CFD++ are the results of compressible flow solvers in an incompressible flow problem that is challenging to solve.

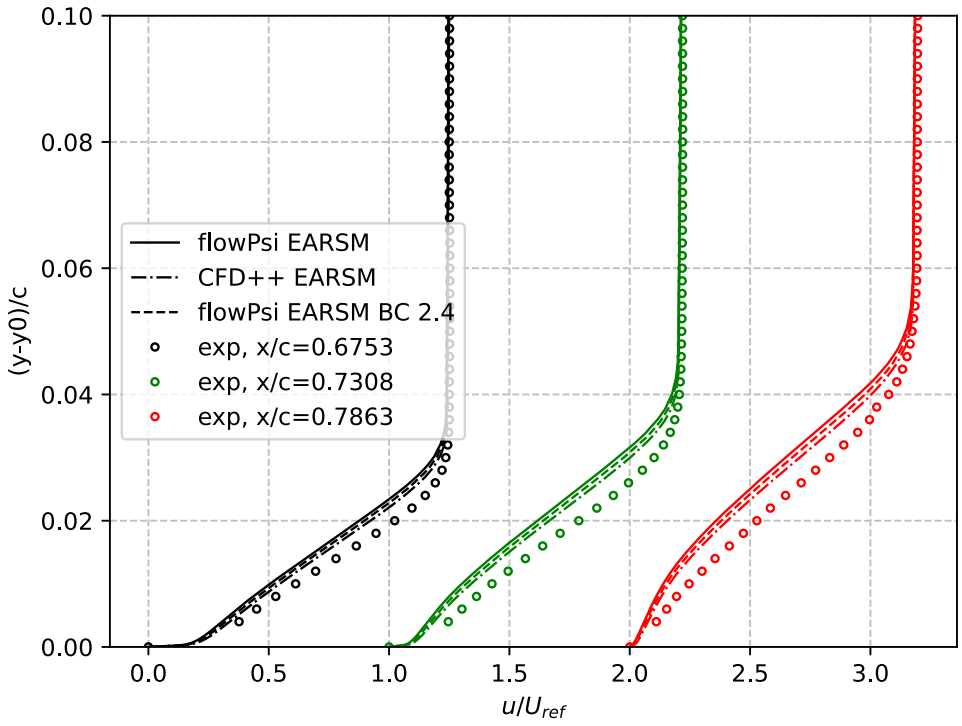

(a) First three stations

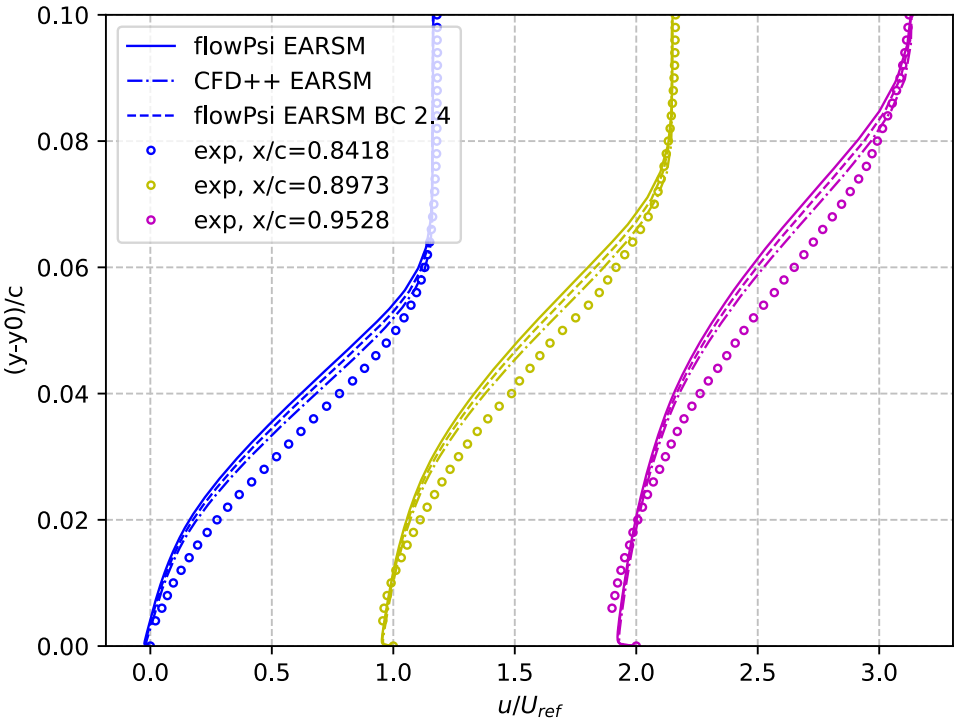

(b) Last three stations

Figure 3.18: x-velocity profiles in a boundary layer of different x-locations for EARSM results of flowPsi and CFD++

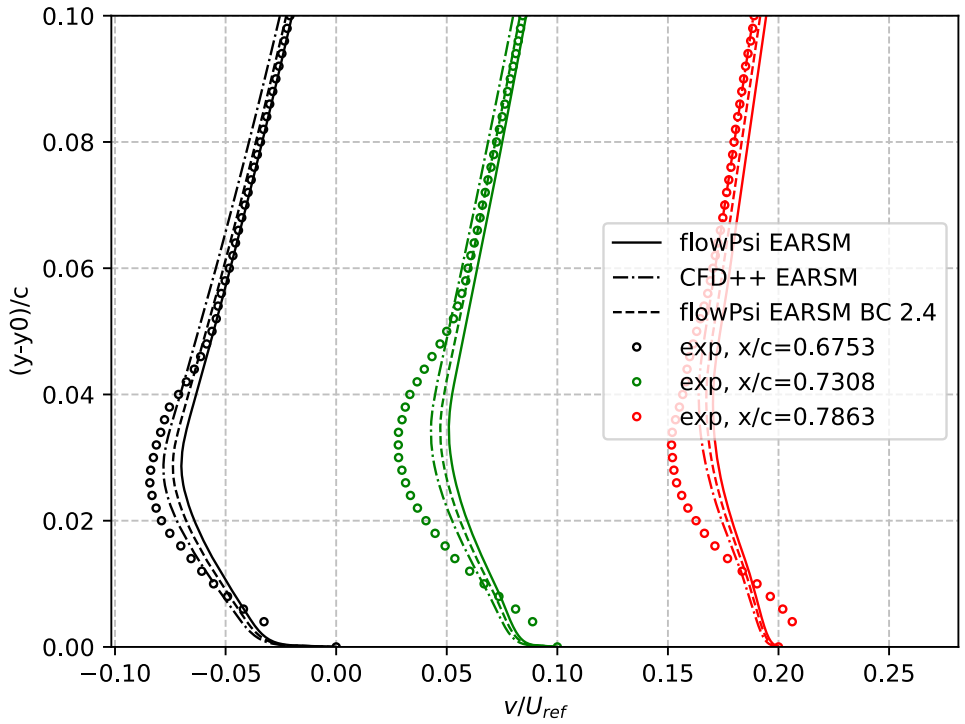

(a) First three stations

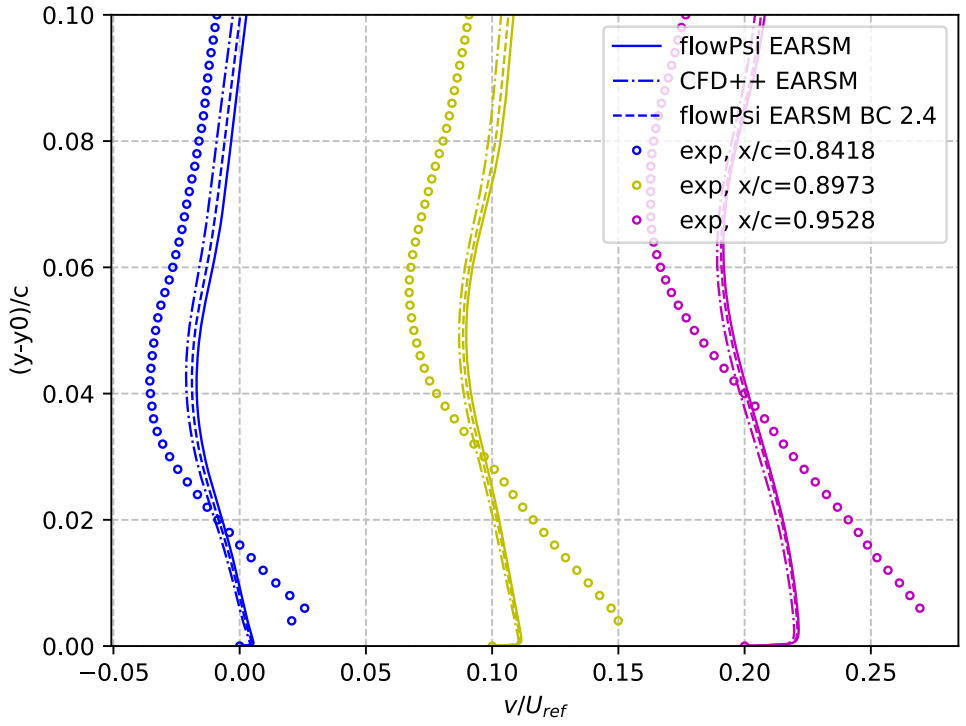

(b) Last three stations

Figure 3.19: y-velocity profiles in a boundary layer of different x-locations for EARSM results of flowPsi and CFD++

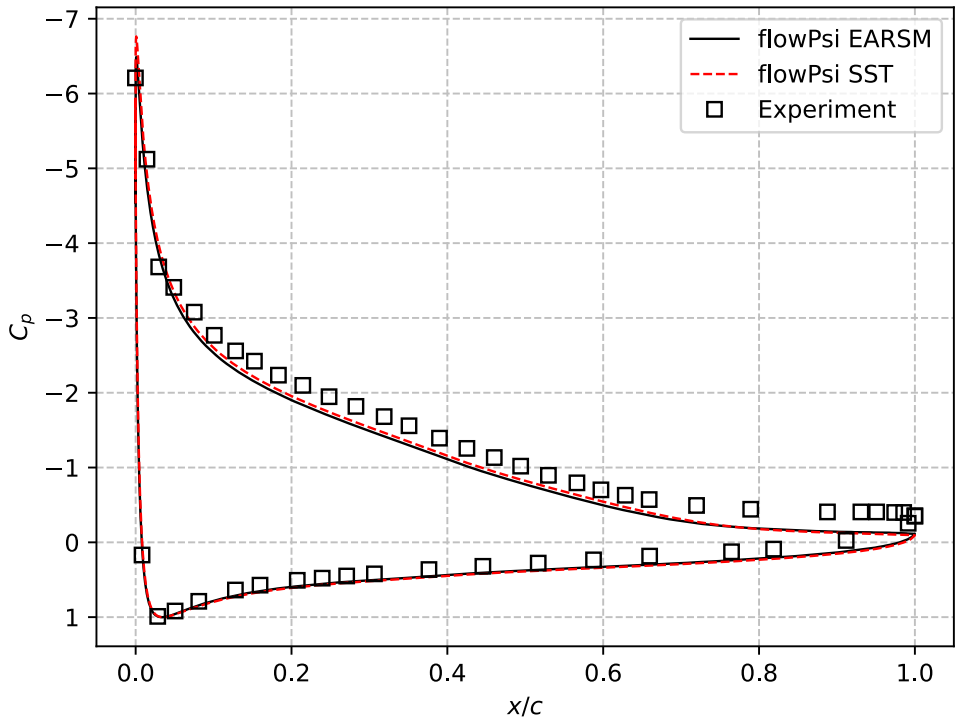

Figure 3.20: Pressure coefficient distribution along the NACA4412 airfoil profile for EARSM and SST of flowPsi along with the experiment [10]

3.3.3 Model Validation

Finally, after the implementation is verified, the results of the model results are compared with both the results of SST in flowPsi and the results of experiments conducted by Coles and Wadcock [10]. When lift coefficients in Table 3.4 are considered, the results of SST are closer to experiments than the present model. In order to make meaningful comparisons, plots of the pressure coefficient distribution along the walls are presented in Figure 3.20. As can be seen from Figure 3.20, the results of the Hellsten's model are nearly the same as the SST results, especially on the pressure side. The only discrepancy is observed on the suction side, on which SST gives slightly closer results to the experimental data. However, both models predict the pressure distribution higher than the experimental results on both walls.

Skin friction coefficient distribution along the upper wall of the airfoil is presented in Figure 3.21 in order to investigate the position of separation predicted with different turbulence models utilized in flowPsi. When the skin friction distribution along the

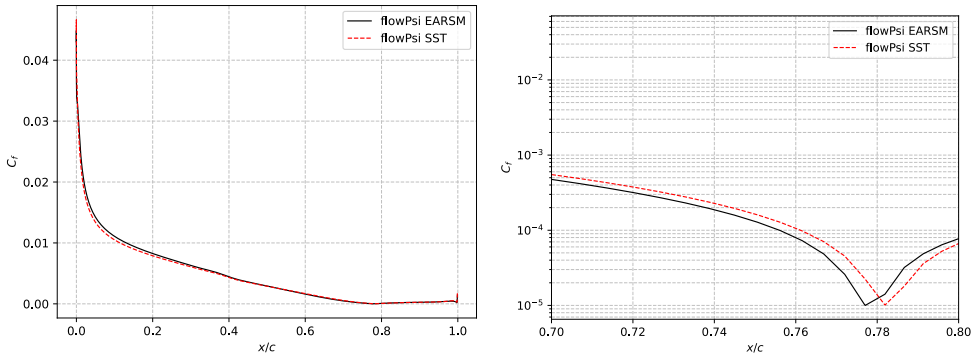

(a) Along airfoil

(b) Near separation

Figure 3.21: Skin friction coefficient along NACA4412 airfoil surface for EARSM and SST of flowPsi

whole wall is considered, there is not any considerable difference between EARSM models with different wall boundary conditions. However, the SST model provides a lower skin friction distribution near the leading edge. Since the separation point cannot be observed from Figure 3.21a, skin frictions near the separation point are presented in Figure 3.21b. Figure 3.21b shows that both models predict the separation location at almost the same location near the 0.78 chords of the airfoil. The SST model predicts a separation location downstream of the location predicted by Hellsten's EARSM.

As x-velocity profiles at six different locations, presented in Figure 3.22, are considered, it can be concluded that the SST model provides the closest results to the experiment in terms of x-velocity. Although the results of EARSM are in strong agreement with the experiment and SST model in the near wall region after the separation, it overpredicts the backflow away from the wall. Even though SST model and the experiment yield almost the same results, the difference between the pressure coefficient data and the aerodynamic coefficients can be explained by errors in the experiment. Experimental results may have been affected by the wall blockage effects, and this can lead to errors in both the measurement of aerodynamic coefficients and angle of attack and pressure distribution. Also, three-dimensional effects might affect the results of the experiment.

As previously presented in Subsection 3.3.2, the y-velocity profiles are shown in Fig-

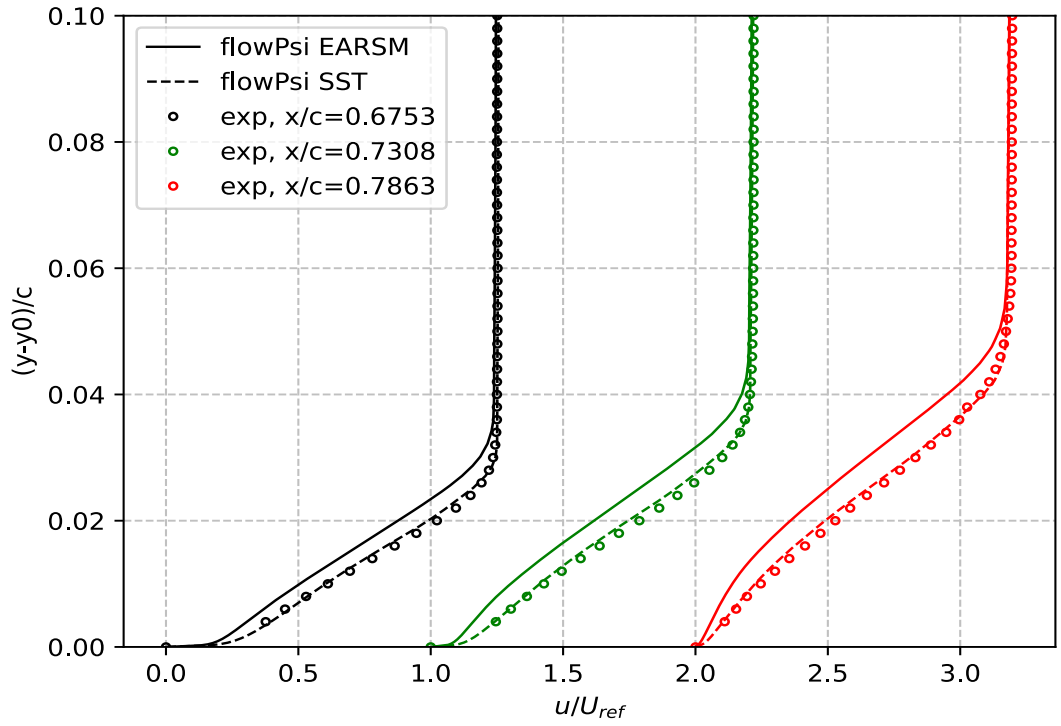

(a) First three stations

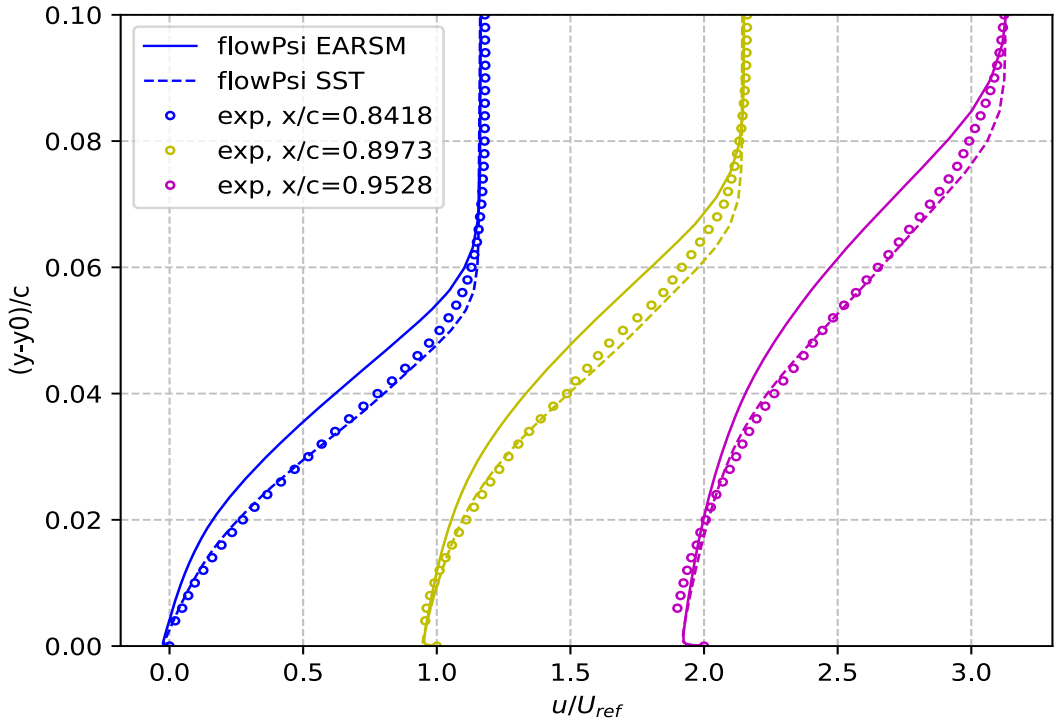

(b) Last three stations

Figure 3.22: x-velocity profiles in a boundary layer of different x-locations for flowPsi SST, EARSM along with the experiment [10]

ure 3.23 EARSM and SST results along with experimental data. This figure implies that both models cannot accurately predict the y-velocity distribution in a boundary layer. However, EARSM is in better agreement with experimental data outside the boundary layer at stations 1 and 2, which are located before the separation. Also, it should be noted that the magnitude of the y-velocities is much lower compared to x-velocities, and differences in terms of numerical values are small.

Lastly, Reynolds shear stress profiles at the same locations obtained from the EARSM solution of flowPsi are given in Figure 3.24 with the experimental results of Coles and Wadcock [10]. The figure shows that EARSM does not show a good match with experiments. This discrepancy might be due to the errors in the experiment, as discussed previously. As demonstrated in the previous Section 3.2, Hellsten's EARS $k-\omega$ model should have predicted Reynolds shear stresses closer to the experiment inside the separated boundary layers.

3.4 Transonic Flow Over RAE2822 Airfoil

Transonic flow over RAE2822 is analyzed for two different flow conditions, to further investigate the model performance on challenging turbulent flows. Flow conditions are determined from the experimental study by Cook et al. [61]. Two cases are selected for validation purposes, Case 9 and Case 10 in Cook's experiments [61]. In both cases, shock occurs on the upper surface of the airfoil. Although in Case 9, the shock is not strong the induce separation, Case 10 has a stronger shock with a significant separation behind the λ shock. These cases will be beneficial to have foresight about the model's capability to predict the complex flow phenomena, such as shock boundary layer interaction, observed in mainly transonic flows over an aerodynamic body.

Boundary conditions used in the analyses are presented in Table (3.5). These are corrected values proposed for the EUROVAL project presented by Haase et al. [1] to modify the experimental conditions to match the farfield conditions used in CFD. Another correction for Case 9 is provided by the EUROVAL project, which suggests an angle of attack of 2.79° can be used to obtain better agreement with experimental

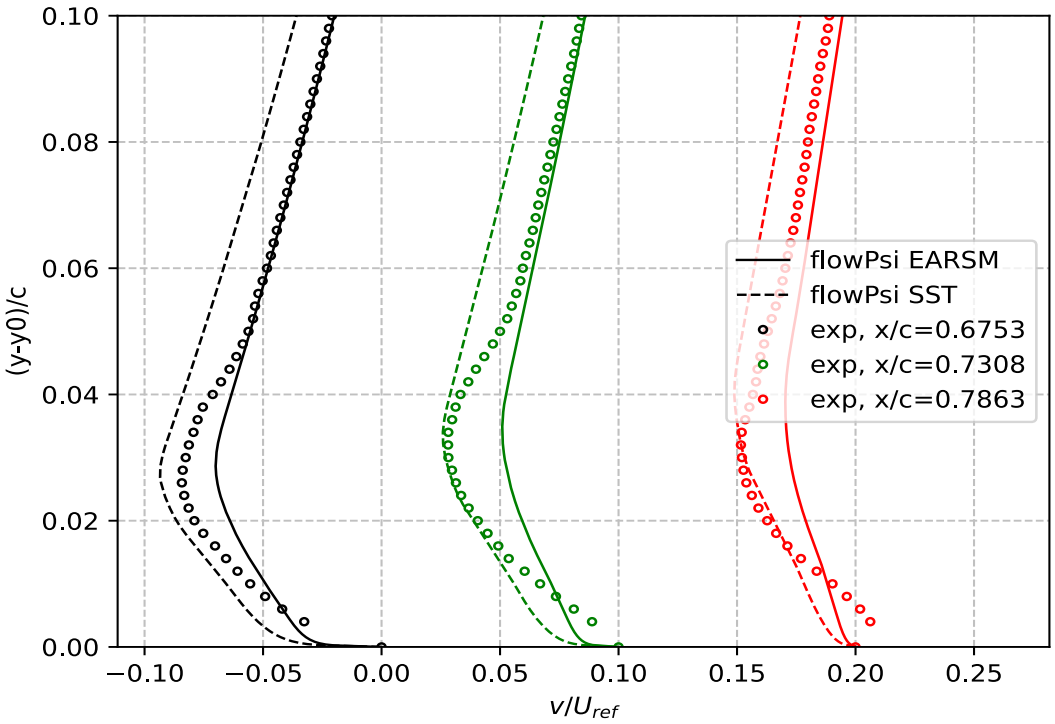

(a) First three stations

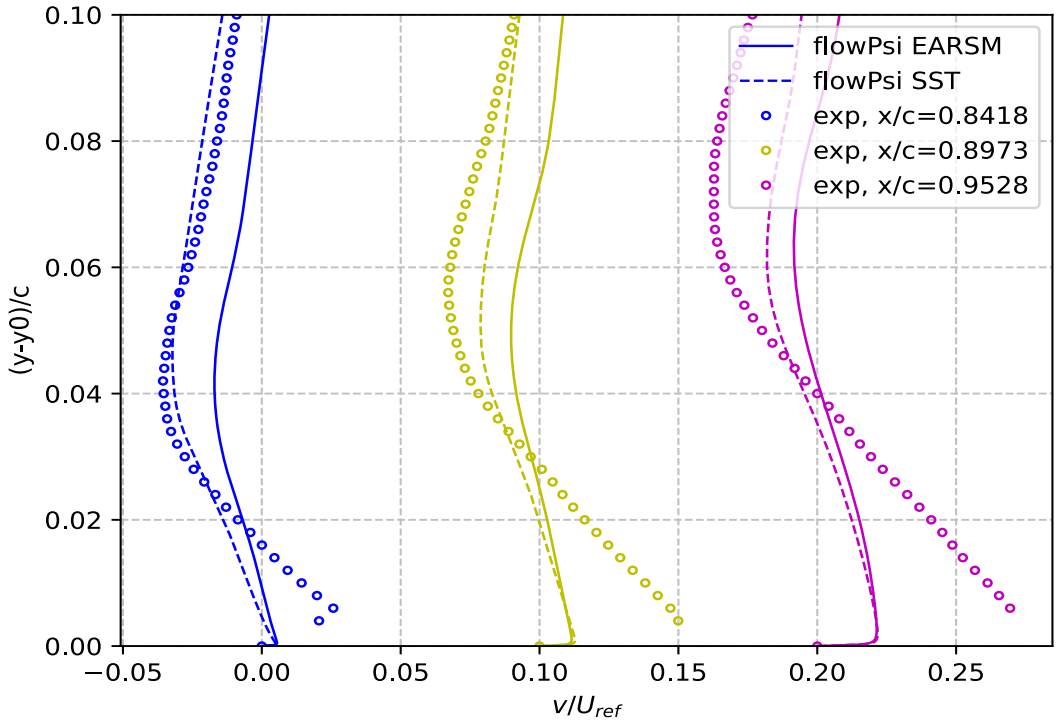

(b) Last three stations

Figure 3.23: y-velocity profiles in a boundary layer of different x-locations for flowPsi SST, EARSM along with the experiment [10]

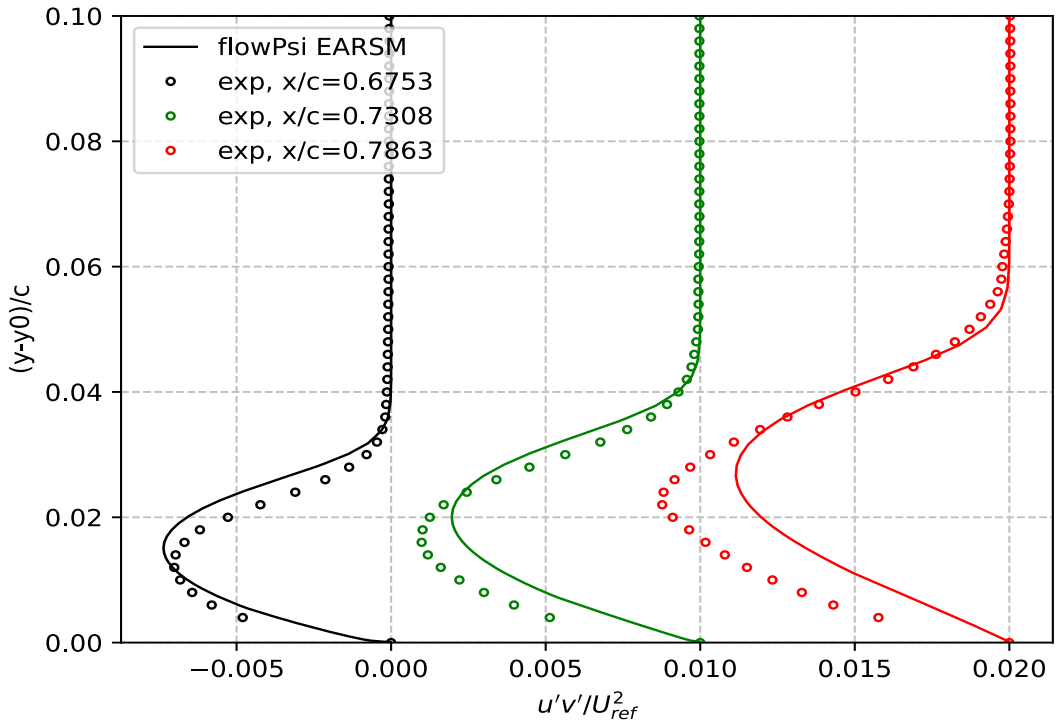

(a) first three stations

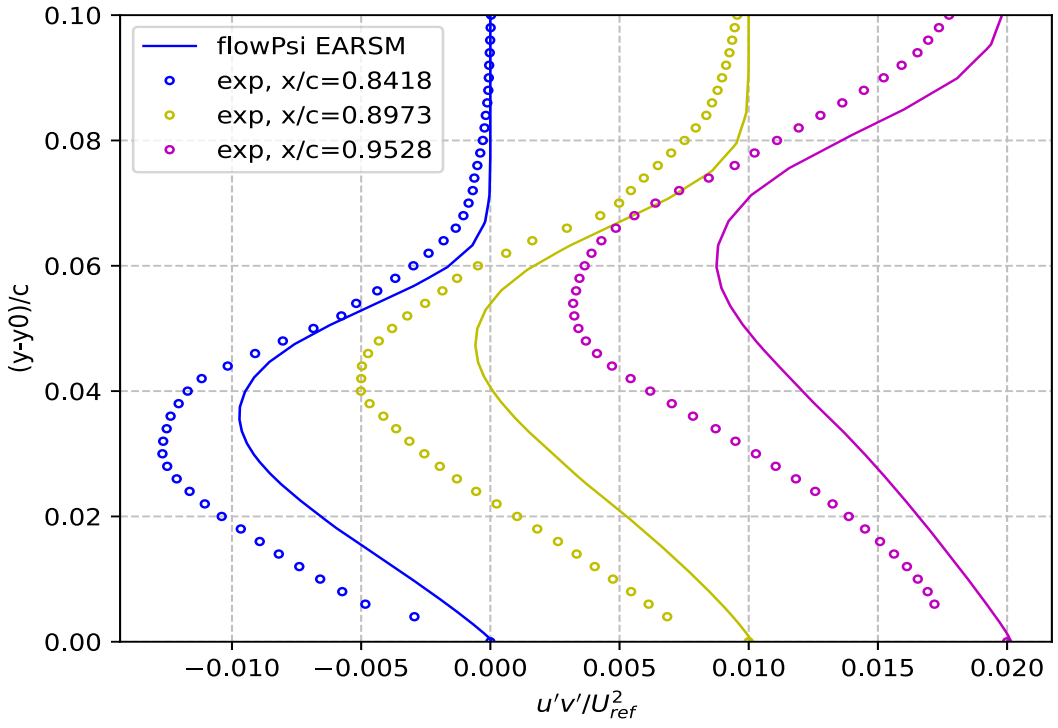

(b) last three stations

Figure 3.24: Reynolds shear stress profiles in a boundary layer of points x/c=0.6573, x/c=0.7308, x/c=0.786 3.24a and x/c=0.8418, x/c=0.8973, x/c=0.9528 for flowPsi SST, EARSM along with experiment [10] 3.24b

Table 3.5: RAE2822 corrected experiment conditions [1]

Case No	Mach	Reynolds	$\alpha[^\circ]$
Case 9	0.734	6.5×10^6	2.54
Case 10	0.754	6.2×10^6	2.57

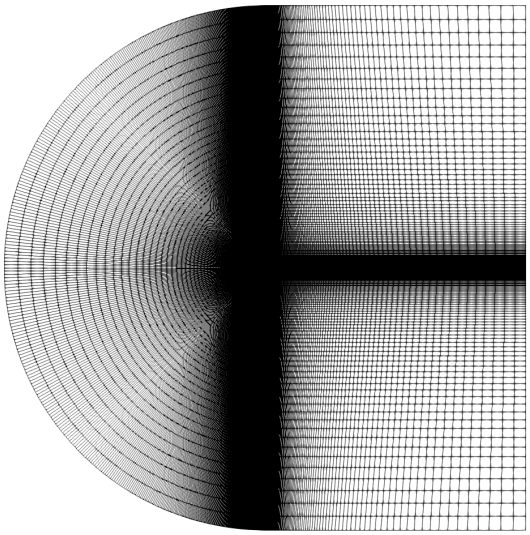

Figure 3.25: RAE2822 solution domain

conditions. However, it is not used in the current study.

A structured grid of C-type is generated. The grid consists of 900 cells over the walls and $1500x600$ on the whole flow domain. The solution domain with the grid is presented in Figure 3.25, and an enlarged view of the grid, generated around the airfoil, is given in Figure 3.26. The outer edges of the domain are modelled as farfield, and they are 100 chords away from the airfoil walls in all directions to eliminate the farfield effects on the solution. RAE2822 airfoil wall is modelled as viscous no-slip walls. The grid adjacent to the walls has below y^+ of 0.2 for both cases.

In both cases, as Lien suggests, turbulence model selection is critical for shock location and extent of separation region predictions [62]. However, Davidson [63] proved that turbulence model choice is more critical in Case 10 since it includes a stronger λ shock, inducing a strong separation upstream of the shock. Among the studied turbulence models, including Wilcox $k-\omega$ and Spalart-Allmaras models, the SST model, as observed by Bardina and Schaefer in separate studies, has the best performance in

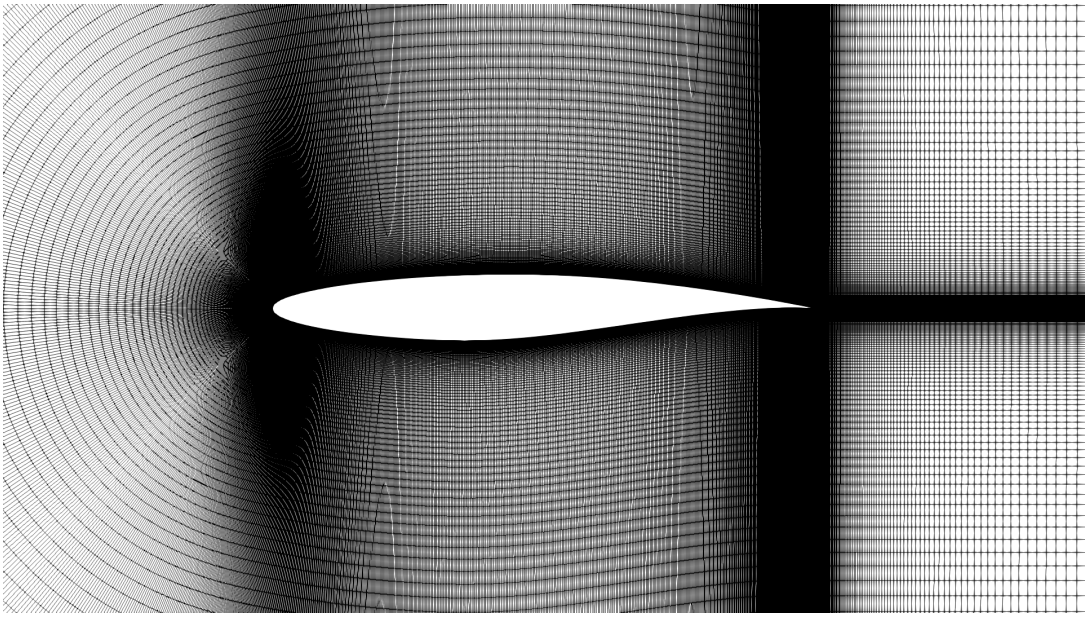

Figure 3.26: RAE2822 enlarged view of the grid

modeling these complex flow physics [64, 65]. As a result, comparing the results of Hellsten's model with the results of the SST model, along with Cook's experimental data, can provide a valuable contribution to model validation.

Shock location and length of separation regions predicted by turbulence models directly affect the accuracy of the predicted aerodynamic coefficients for aerodynamic bodies flying in a transonic flow regime. In order to compare the models' performance in predicting lift and drag coefficients for the RAE2822 airfoil, Table 3.6 is given. Noting that the actual values presented in Cook's values are different from the presented table [61]. Cook found the lift coefficients of the Case 9 and Case 10 were 0.803 and 0.743, respectively, and drag coefficients were 0.0168 and 0.0242, respectively. The presented experimental results, however, differ from the original by applying a correction to agree with the freestream Mach numbers on CFD, as Davidson and Rizzi did in their study [63]. Table 3.6 shows that the SST model has a better agreement with experimental lift data compared with the Hellsten's turbulence model in predicting the lift coefficient. However, the Hellsten's EARSM has a better overall agreement in terms of the drag coefficient. In both cases, the turbulence models underpredict the lift and drag coefficients.

Mach number contours for Case 9 obtained with the SST and Hellsten's models are

Table 3.6: RAE2822 aerodynamic coefficients

Source	Case 9		Case 10	
	C_D	C_L	C_D	C_L
flowPsi-EARSM	0.0153	0.730	0.02300	0.694
flowPsi-SST	0.0148	0.747	0.02298	0.708
Experiment [61]	0.0166	0.794	0.0239	0.735

presented in Figure 3.27. It can be seen that both solutions provide a shock on the suction side of the airfoil with moderate strength. In order to compare the pressure distributions along the walls of the airfoil, Figure 3.28 is presented. Values of the coefficient of pressure are reversed in the graph to present the distribution of the pressure coefficient on the suction side on the upper side of the figure, and the pressure side on the lower side of the figure. As seen from the figure, both models tend to predict higher pressure on the suction side of the airfoil. However, both models have similar behavior on the pressure side and after the shock on the upper wall.

The shock location predicted by the SST model is closer to the experiment than Hellsten's model, which predicts the shock upstream of the SST model and the experiment. It should be noted that, in the experiments, transition trips are used at the locations x/c=0.03 for both the pressure and suction sides of the airfoil. Thus, not modelling the laminar and transitional flow portion may affect the accuracy of the CFD results. Also, the skin friction coefficient distribution along both walls is shown in Figure 3.29. Again, both models agree well with each other and the experiment on the pressure side, but they differ near the leading edge of the suction side. It is also seen in Figure 3.29 that EARSM predicts shock location upstream of the SST model. Another observation is that the SST model predicts lower skin friction just behind the shock, and the skin friction distribution obtained with the SST model gives better overall agreement with the experiment behind the shock. The EARSM overestimates the skin friction behind the shock, which could mean that the SST model predicts a larger drop in velocity magnitude in the boundary layer behind the shock or that the EARSM predicts a higher turbulent viscosity.

Mach contours of Case 10 for both models are presented in Figure 3.30. As seen

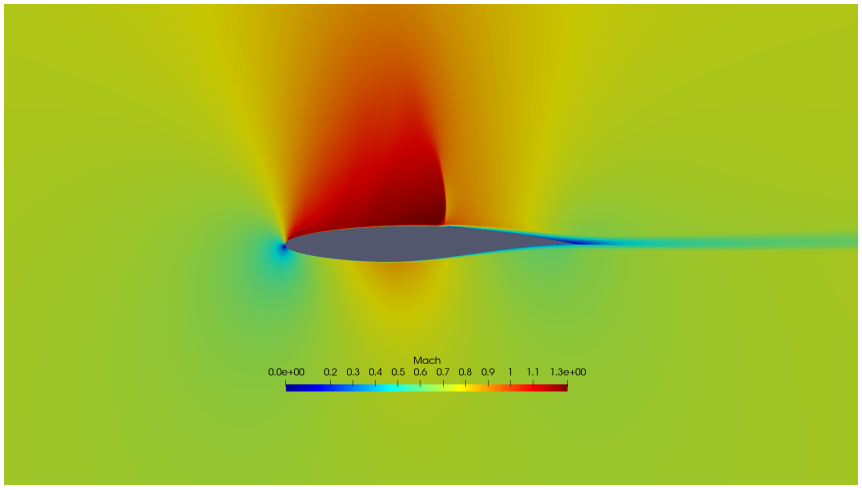

(a) EARSM

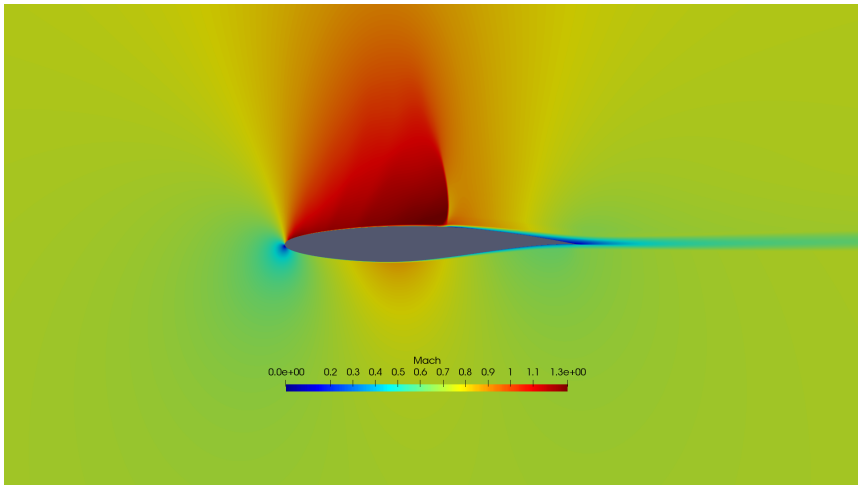

(b) SST

Figure 3.27: Mach contours for RAE2822 Case 9 of EARSM 3.27a and SST 3.27b

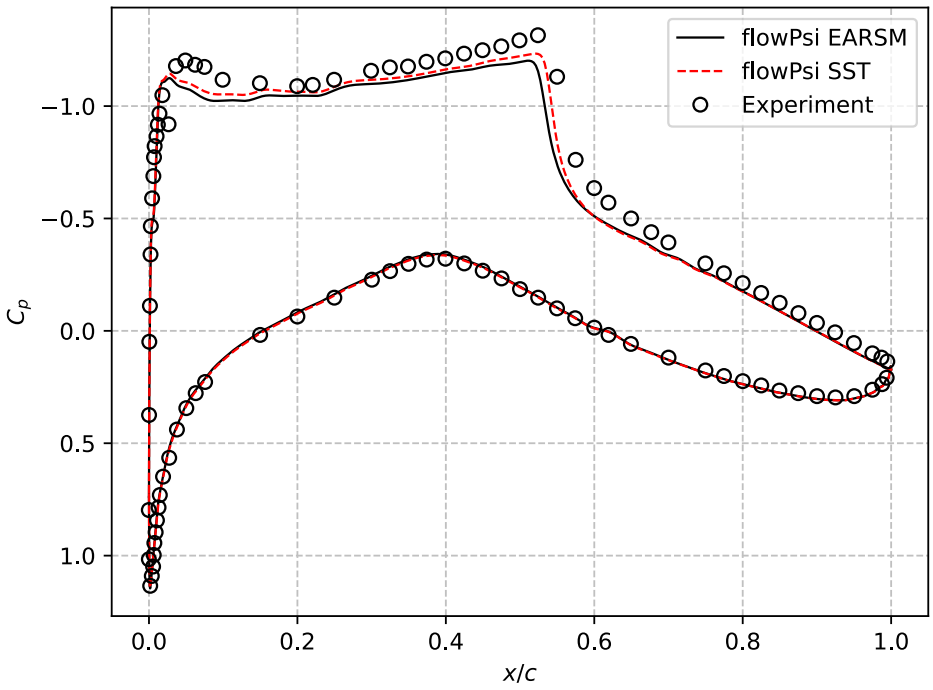

Figure 3.28: Pressure coefficient distribution along the RAE2822 airfoil profile in Case 9

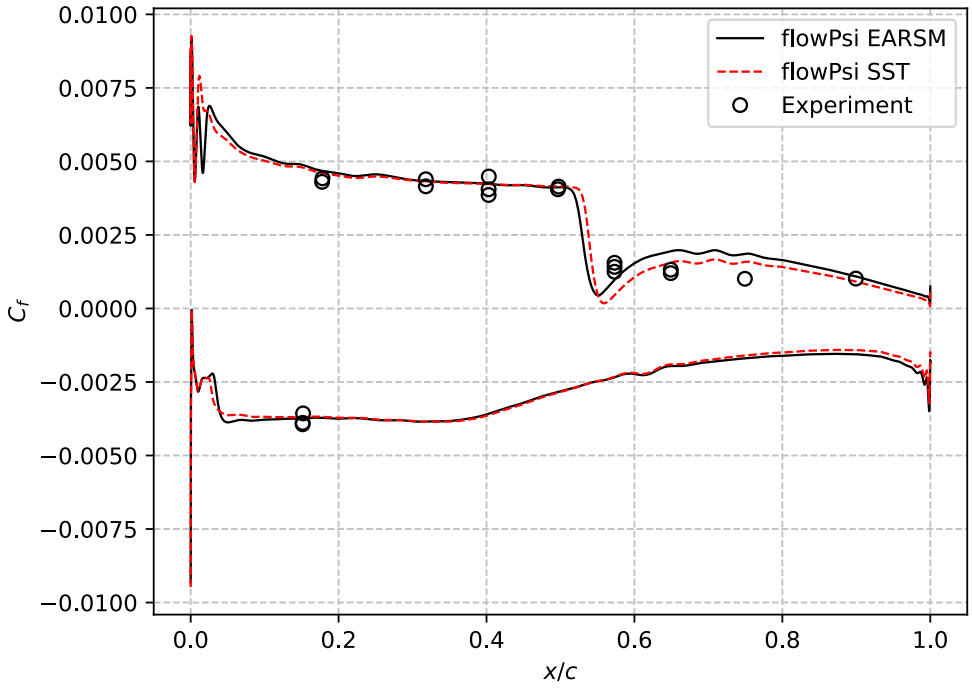

Figure 3.29: Skin friction coefficient distribution along the RAE2822 airfoil profile in Case 9

from the contours, this case involves a stronger shock wave with separation behind the λ shock near the airfoil. As Figure 3.31 indicates, both models tend to overpredict the pressure on the suction side of the airfoil, especially near the leading edge. This difference can be, again, the result of not modelling the transition trips utilized in the experiment. After the leading edge, both models give very similar results except for the shock position, where EARSM is clearly in better agreement with the experimental data for this case. However, both models give higher pressure after the shock and inside the separation zone. The skin friction coefficient for Case 10, presented in Figure 3.32 shows that SST is in better agreement with the experiment on the suction side behind the shock. Also, this figure indicates that both models predict the separation near the same location, which is just after the λ shock wave. However, SST shows a clearly larger separation behind the shock.

This validation problem proves that both models can be used to analyze the performance of aerodynamic vehicles in transonic regime, where the flow problem involves λ shock and shock-induced separation.

3.5 Transonic Flow Over Axisymmetric Bump

The fifth test case chosen is transonic flow over an axisymmetric circular bump. Experiments were conducted by Bachalo and Johnson in 1986 [66] in NASA's 2x2 ft transonic wind tunnel. This case is a widely studied validation case of turbulence models' performance in modelling shock-boundary layer interaction in transonic flow problems. In this validation case, a circular bump of 20.32 cm in length and 1.905 cm in height is attached to a cylinder with a radius of 7.62 cm. The second finest grid provided by NASA's Turbulence Modelling Resource is utilized in the validation study [59]. The grid has 721 nodes in the streamwise direction and has 321 nodes in the normal direction. Note that the elements of the grid are clustered around the shock position, as can be seen in Figure 3.33.

This test case is modelled as an axisymmetric flow problem in flowPsi. Boundaries of the solution domain are shown in Figure 3.33. The outer wall of the domain surrounding the cylinder and the bump is modelled as an inviscid slip-wall boundary.

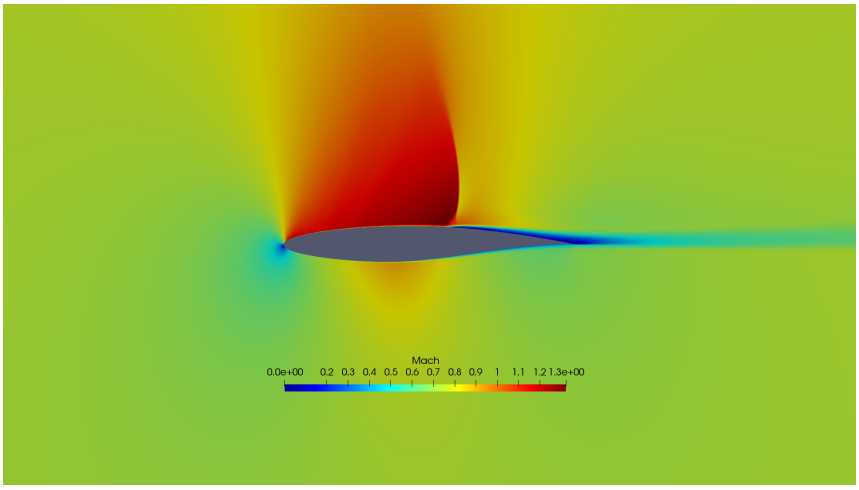

(a) EARSM

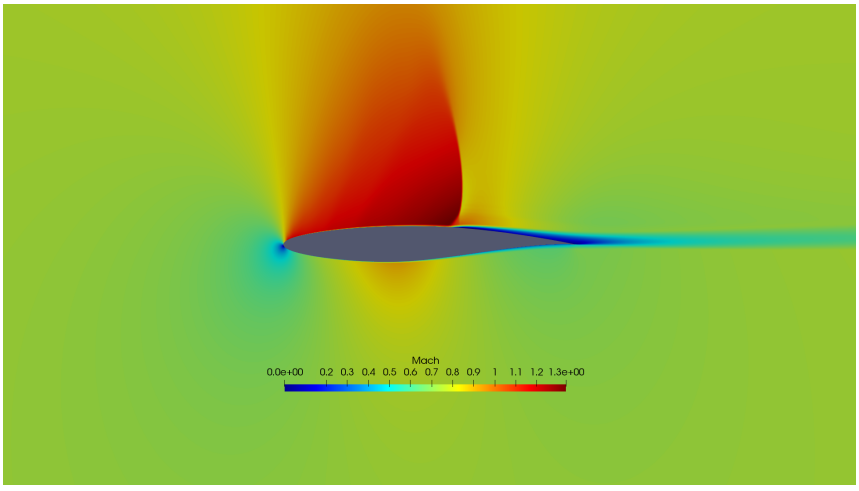

(b) SST

Figure 3.30: Mach contours for RAE2822 Case 10 of EARSM 3.30a and SST 3.30b

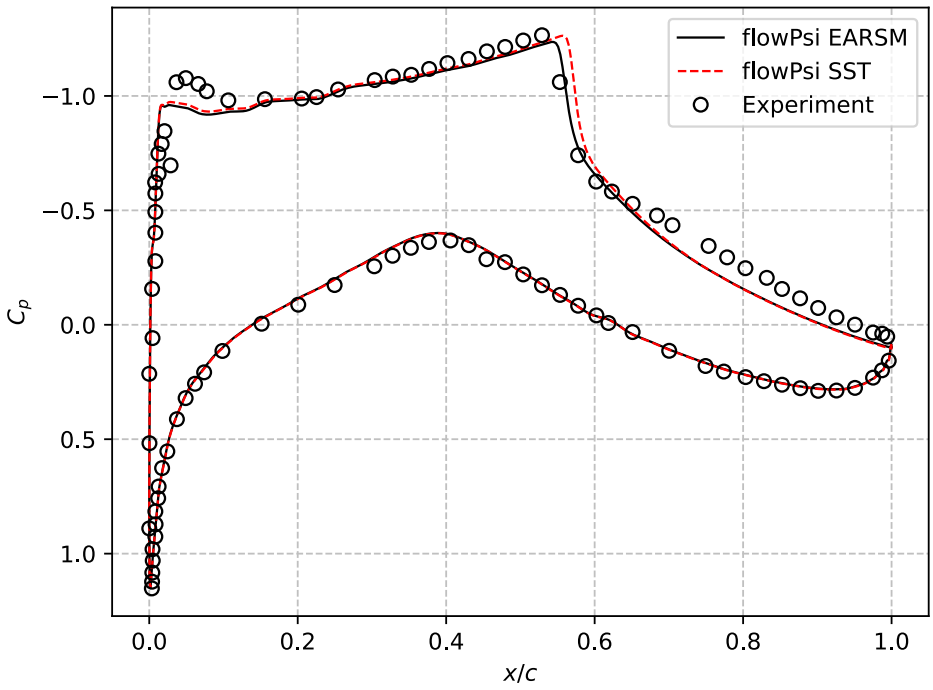

Figure 3.31: Pressure coefficient distribution along the RAE2822 airfoil profile in Case 10

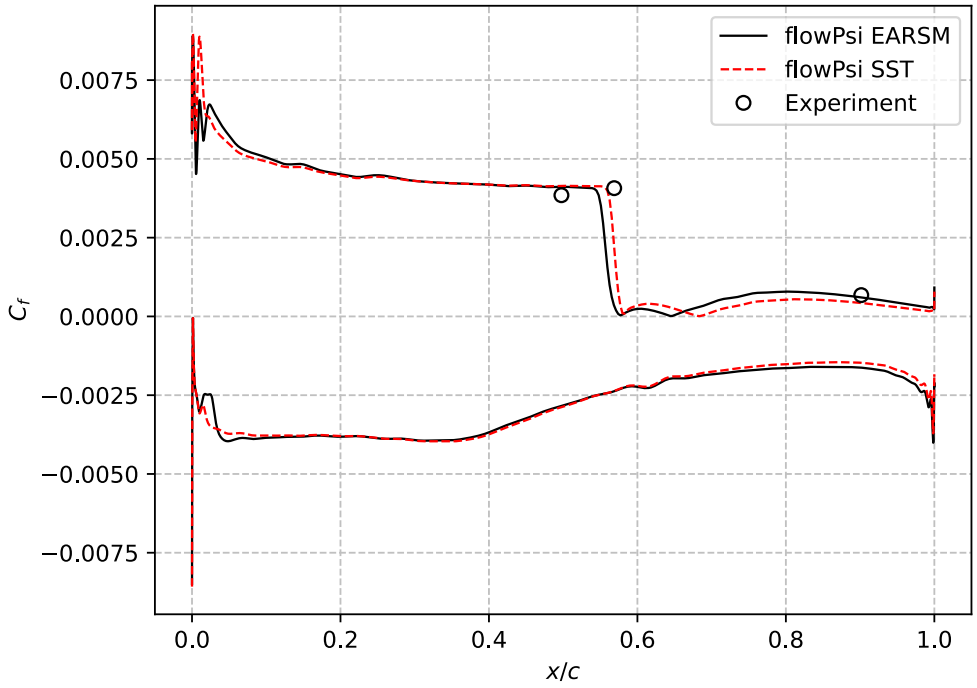

Figure 3.32: Skin friction coefficient distribution along the RAE2822 airfoil profile in Case 10

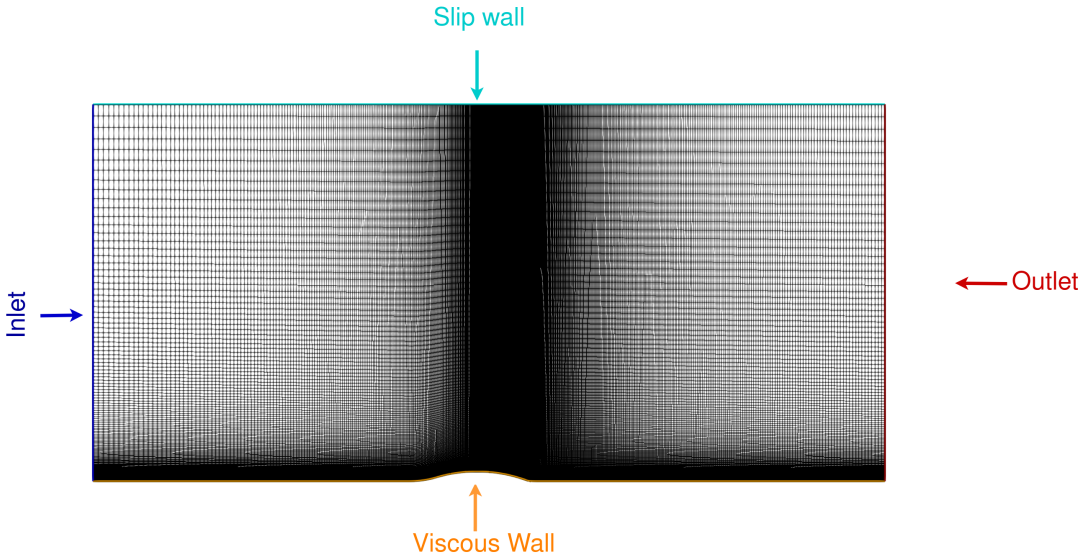

Figure 3.33: Solution domain of axisymmetric bump

The inlet is modelled as an inflow boundary type with a Mach number of 0.875 and a Reynolds number of 2.764 million per bump chord. A viscous wall boundary condition is applied both to a cylinder and a bump. The cylinder extends 3.2 chords in the downstream direction and 4.4 chords in the upstream direction from the bump.

This case is utilized to validate Hellsten's EARSM under transonic flow conditions and for axisymmetric flow problems. Velocity contours over the bump obtained from the analyses conducted with Hellsten's EARS $k-\omega$ and SST models are presented in Figure 3.34. Note that both models predicted a λ shock upstream of the half chord of the bump and a separated flow regime behind the shock.

Pressure coefficient along and behind the bump are presented in Figure 3.35. Pressure coefficient distribution differs between the models. Shock location is predicted by the SST model is in excellent agreement with the experimental data of Bachalo and Johnson [66]. The EARSM of Hellsten predicted the shock location earlier compared to the experiment and the SST model. The pressure distribution of EARSM just behind the shock is clearly in better agreement with the experimental results. At around 1.4 chords, where the bump ends and the cylindrical section continues, both models give nearly identical results with overestimated pressure compared with the experiments.

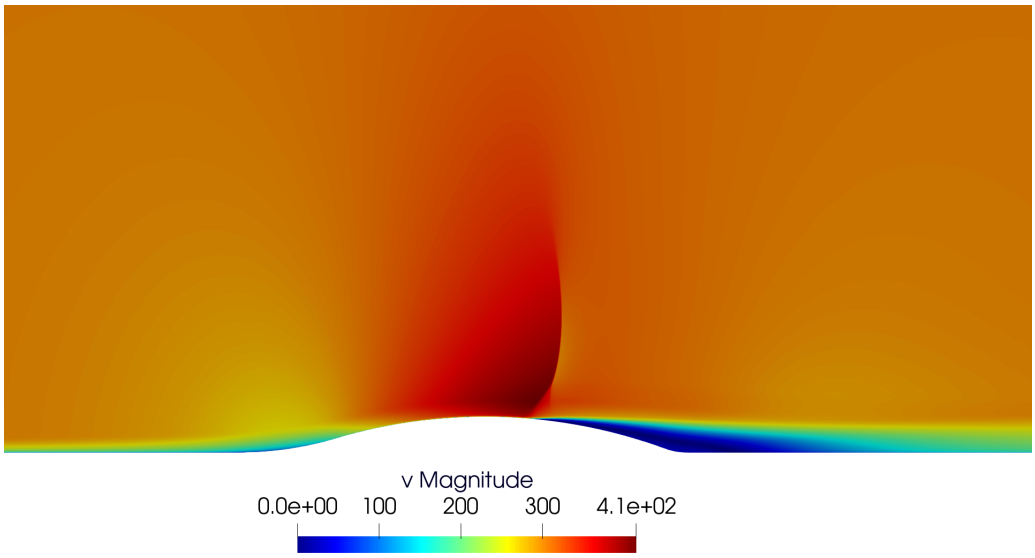

(a) EARSM

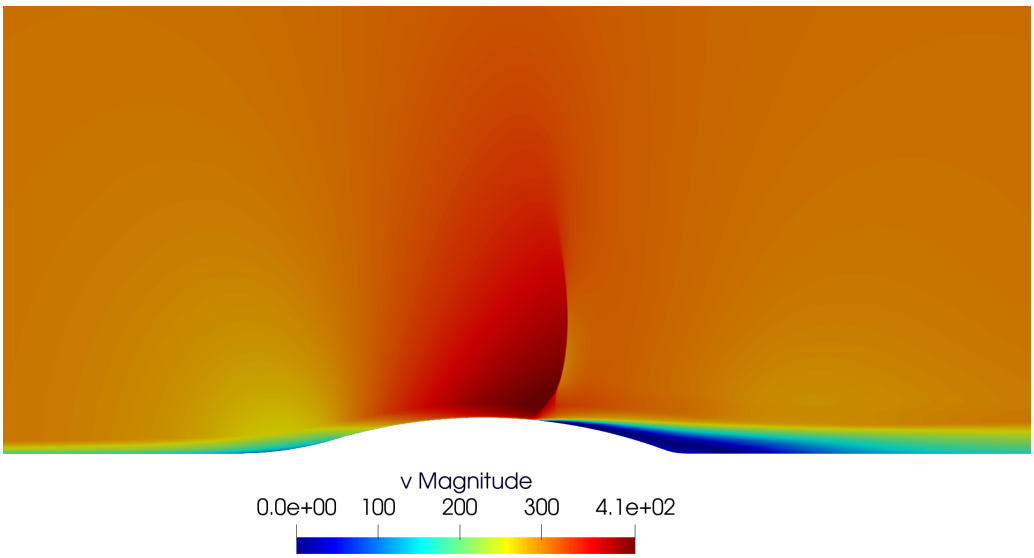

(b) SST

Figure 3.34: Mach contours of flow over transonic bump for EARSM 3.34a and SST 3.34b solutions

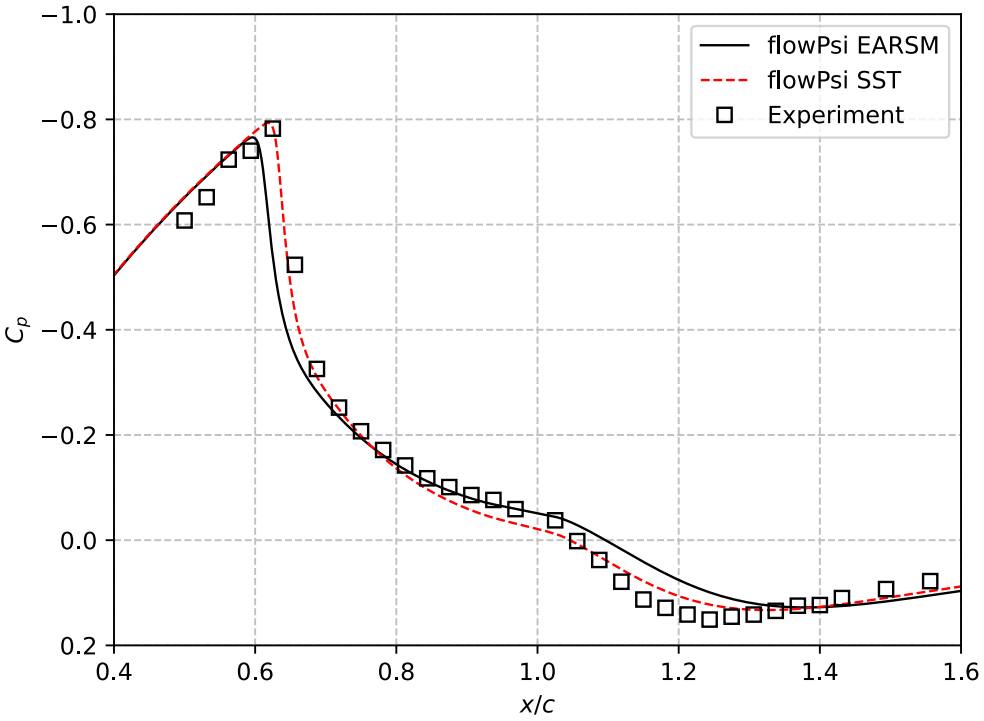

Figure 3.35: Pressure coefficient distribution along the transonic bump

In order to observe both models' capabilities upstream and downstream of the shock and inside the separation regions, x-velocity profiles and turbulent kinetic energy profiles are plotted and presented in Figures 3.36 and 3.37, respectively. Note that $y^{'}$ given in the figures corresponds to the distance from the viscous wall; in other words, $y' = 0$ on the walls. Eight different data extraction locations of both figures are $x/c =$ –0.250, 0.688, 0.813, 0.938, 1.0, 1.125, 1.250, 1.375. The first location is before the bump, and the second location is around the λ shock.

The x-velocity plots show that both models agree well with the experimental data before the bump. However, after the complex flow occur over the bump, both models start to deviate from the experiment. Both models give unsatisfactory results in terms of the x-velocity profile in a boundary layer in the second data location, which is near the shock wave. We can conclude that both models failed to predict the boundary layer around the shock. This might be due to the anisotropy of the normal stresses dominating in these types of flows.. One can use RSTMs for better predictions. Locations inside the separation show that both models overpredict the amount of backflow, except that both models provide better agreement with the experimental results near

the wall and boundary layer edge. Results from the last three stations show that both models tends to predict the reattachment upstream of the experiment, and they gave a smaller amount of x-velocity inside the boundary layer after the reattachment.

Turbulent kinetic energy normalized by the freestream velocity solutions are given in Figure 3.37 for the SST model and Hellsten's model along with the experimental data. Both models are in reasonably good agreement outside the boundary layer, except near the shock location, in which both models predict lower turbulent kinetic energy. Although models accurately predict turbulent kinetic energy outside the boundary layer, their behavior changes inside the boundary layer after the shock and inside the separation and the reattachment regions, and they deviate from the experimental results. Maximum turbulent kinetic energy inside the boundary layers are predicted more accurately by Hellsten's model compared with the SST. However, the location of maximum turbulent kinetic energy is not in agreement with experimental data. Although the SST model tended to predict a lower maximum turbulent kinetic energy, the distribution of turbulent kinetic energy inside a boundary layer is in better agreement with experimental data except after the reattachment point. The EARSM gives better results after the reattachment, especially in regions near to the wall.

Finally, Reynolds shear stresses inside the boundary layer of the eight locations are plotted with the results of the EARSM and the experiment and given in Figure 3.38. It can be concluded from the figure that the model gives nearly identical results to the experiment before the bump, in terms of Reynolds shear stresses. However, the results deviate from experiment near the shock location, even outside the boundary layer. The EARSM results also showed that the shear stresses solved by the current model are lower than the experiment inside the separation. However, it provides better agreement downstream of the reattachment region.

The results of this current test case showed that this model can be used for transonic flows involving shocks and separation. Hellsten's model predicts an earlier separation location compared with SST model and the experiment. However, Hellsten's model better agrees starting from the reattachment point in terms of x-velocity, turbulent kinetic energy, and Reynolds shear stresses. This case, with the Driver's test case presented in Section 3.2, validates the model utilization in axisymmetric problems.

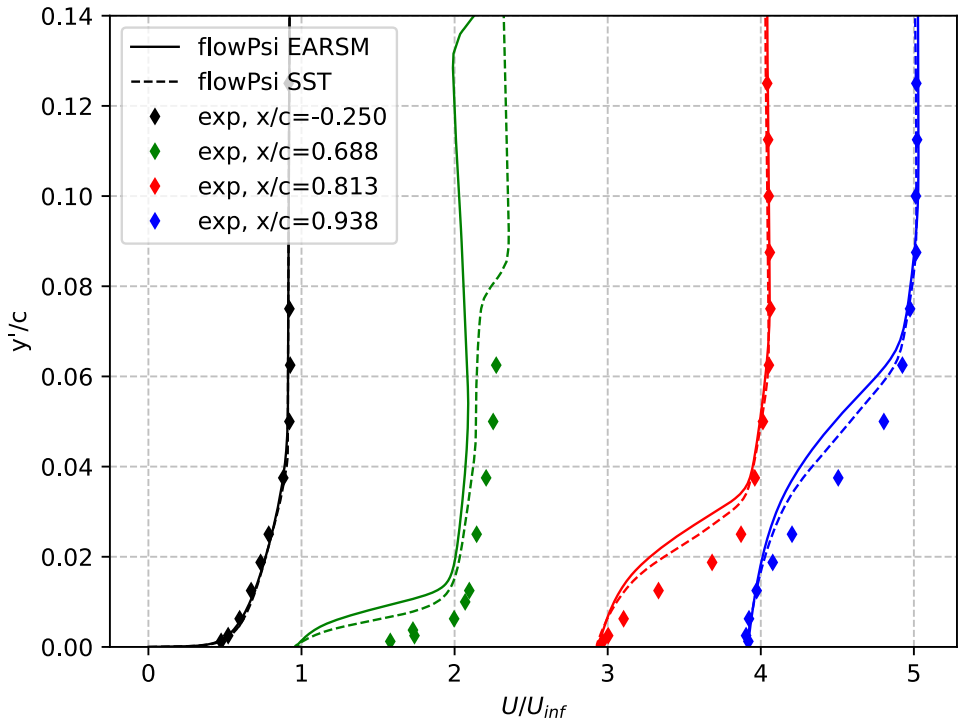

(a) First four stations

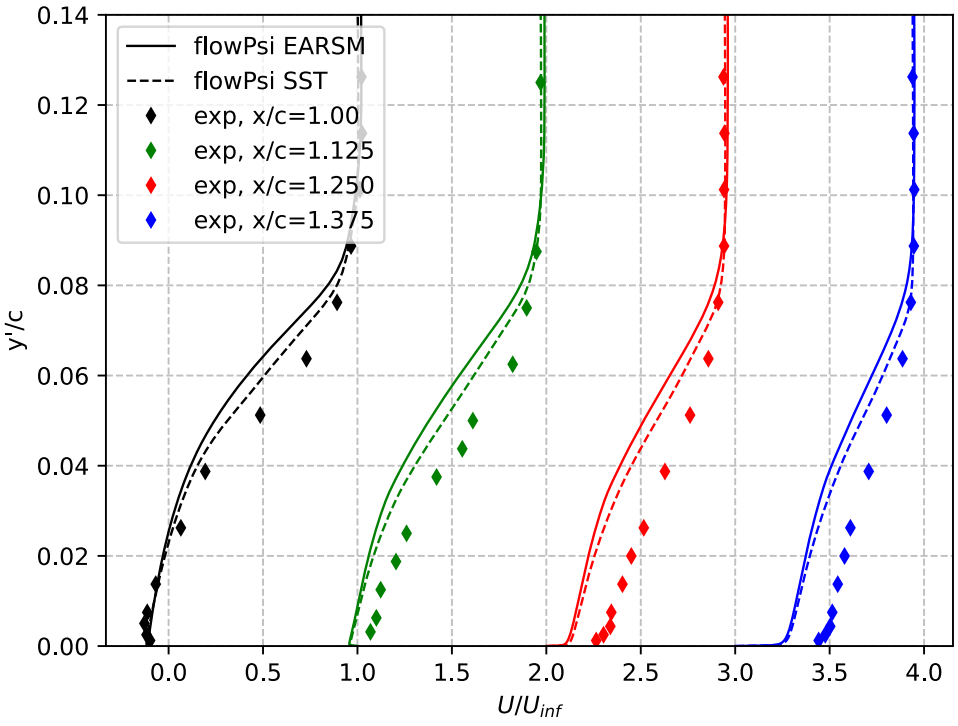

(b) Last four stations

Figure 3.36: x-velocity profiles in a boundary layer of different x-locations for transonic bump case

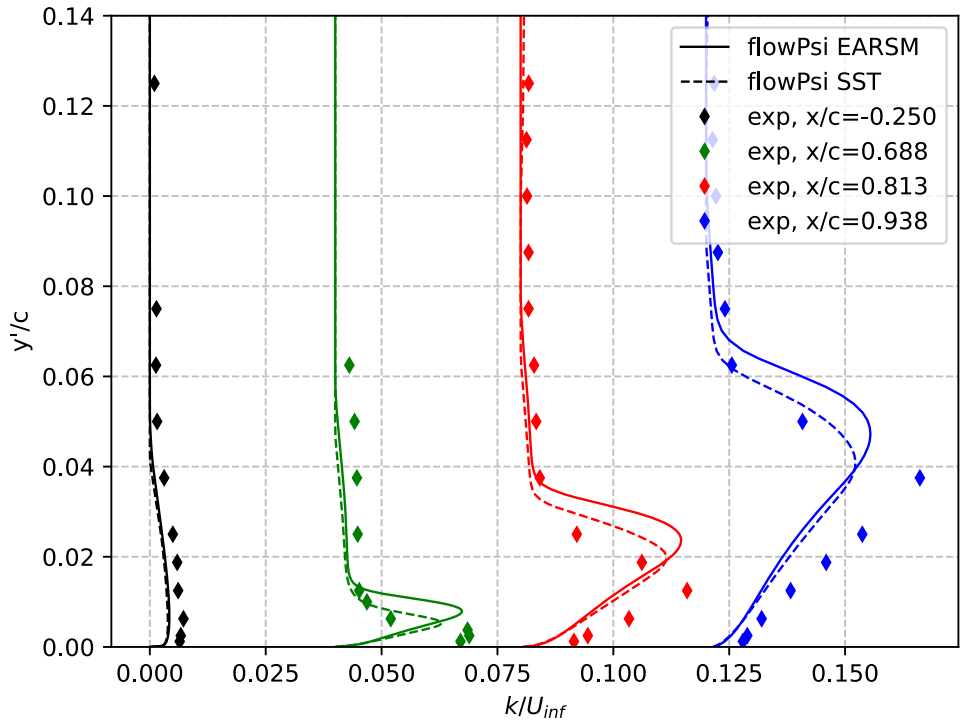

(a) First four stations

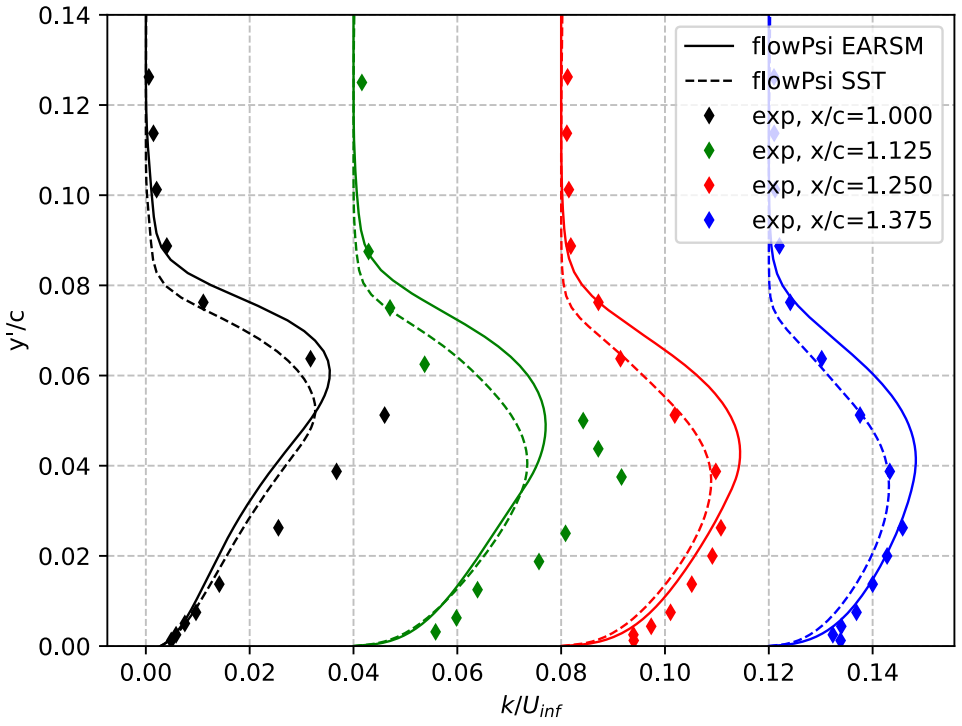

(b) Last four stations

Figure 3.37: Turbulent kinetic energy profiles in a boundary layer of different x-locations for transonic bump case

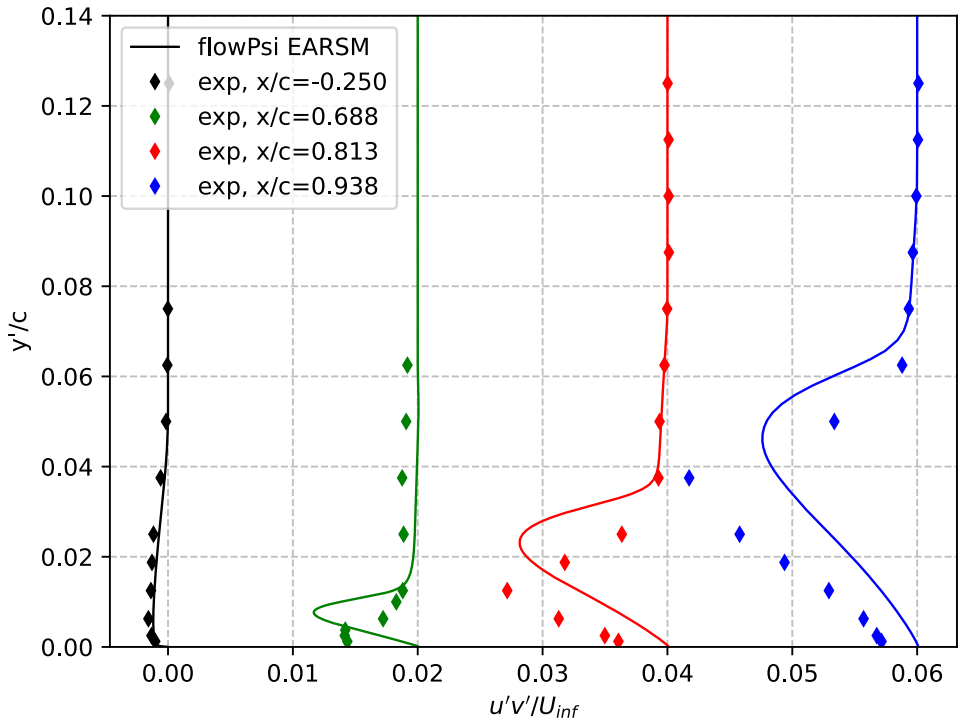

(a) First four stations

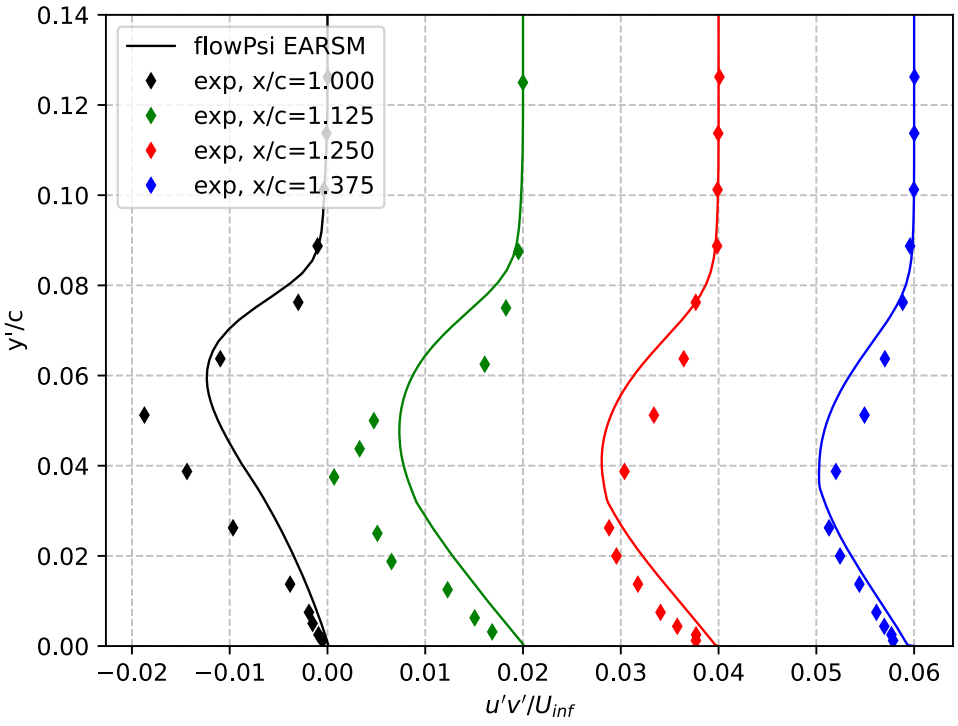

(b) Last four stations

Figure 3.38: Reynolds shear stress profiles in a boundary layer of different x-locations for transonic bump case

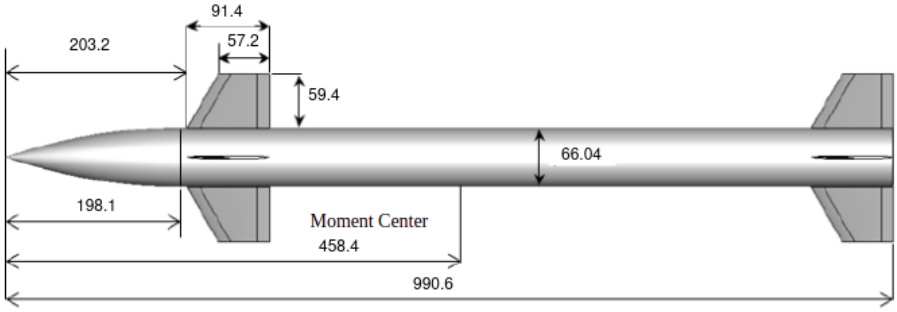

Figure 3.39: Dimensions of NASA Tandem Control Missile

3.6 NASA TCM

Aerodynamic coefficients of the NASA Tandem Control Missile (NASA TCM) are calculated and compared with experiments conducted by NASA in order to validate the implemented model in three-dimensional supersonic aerodynamic flow problems. Wind tunnel tests of TCM model are conducted at freestream Mach numbers ranging between 1.75 and 2.86 and angles of attack ranging between -4° and 28°. TCM model consists of an ogive nose with a radius of 610.9 mm, a cylindrical body, and four tails and four canards of the same size that are inlined with each other. Figure 3.39 shows dimensions of the TCM model in millimeters. Experimental results of the "X" form ($\phi = 45°$) configuration with zero canard deflections at 1.75 freestream Mach number and Reynolds number of $6.6 \times 10^4/m$ are compared with the CFD results in this study. This case was also studied by NATO Applied Vehicle Technology (AVT) Panel Group 082 of the Research Technology Organization (RTO) for the validation of turbulence models. X-form configuration is selected since the canard-induced vortices are more dominant and have strong influences on the forces acting on the body and tail components [67].

Computational grid is is unstructured and has 8.15 million elements. The surface mesh on the model is given in figure 3.40. 20 prism cell layers are generated, and $y^+$of the first prism cell layer have maximum value of 0.6. A cylindirical computational domain was generated and farfield boundary conditions were applied on domain faces, which extended up to 20 model length.

Figures 3.41, 3.42 and 3.43 show lift, drag and pitching moment coefficients obtained

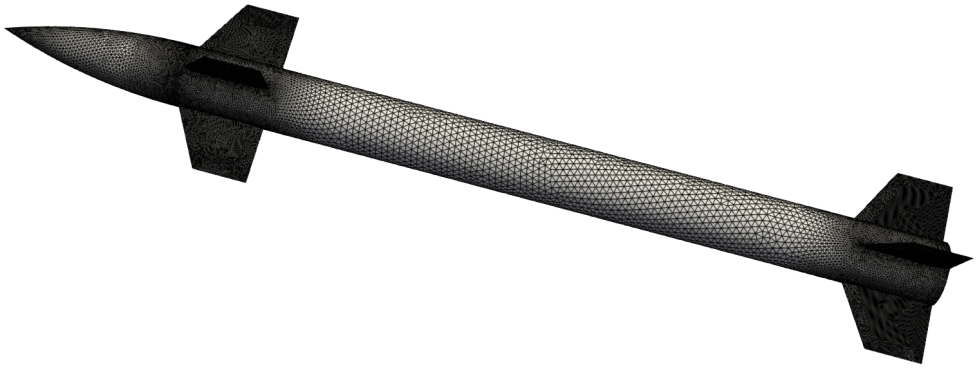

Figure 3.40: Surface mesh of NASA TCM

from analyses with SST and Hellsten EARS $k - \omega$ models, as well as with experimental data from NASA. Note that the pitching moment reference center is given in Figure 3.39, which is 485.39 mm away from the missile nose tip.

The lift coefficient obtained from CFD analyses is nearly in perfect agreement with the experimental data. However, the drag coefficient is not accurately predicted with both models. The models exhibit the same behavior in drag coefficient, and they both overpredict drag coefficient compared with the experimental measurements. This might be due to insufficient grid resolution utilized in the analyses. A finer grid around the shocks and downstream of the missile, where separation occurs, may enhance the drag coefficient predictions. Also, it is observed that the highly nonlinear behavior of the pitching moment is predicted accurately with both models except at the 9.9° angle of attack where the peak occurs. This might be the result of the grid resolution again. Since other nonlinearities are captured accurately with the turbulence models, we can say that both models are capable of modelling the vortex interactions of a supersonic aerodynamic vehicle. Canard vortices generated from the fin tip and body-induced vortices have a strong influence on the forces acting on the tails that causes nonlinearities in the pitching moment. Although this complex flow is challenging to solve for many CFD software and turbulence models, flowPsi and compared turbulence models had satisfactory results. As a result, the EARSM model is validated to be used in a supersonic aerodynamic problems with complex vortex and body interactions, even at high angles of attack where separation and vortices dominate the behavior of aerodynamic coefficients.

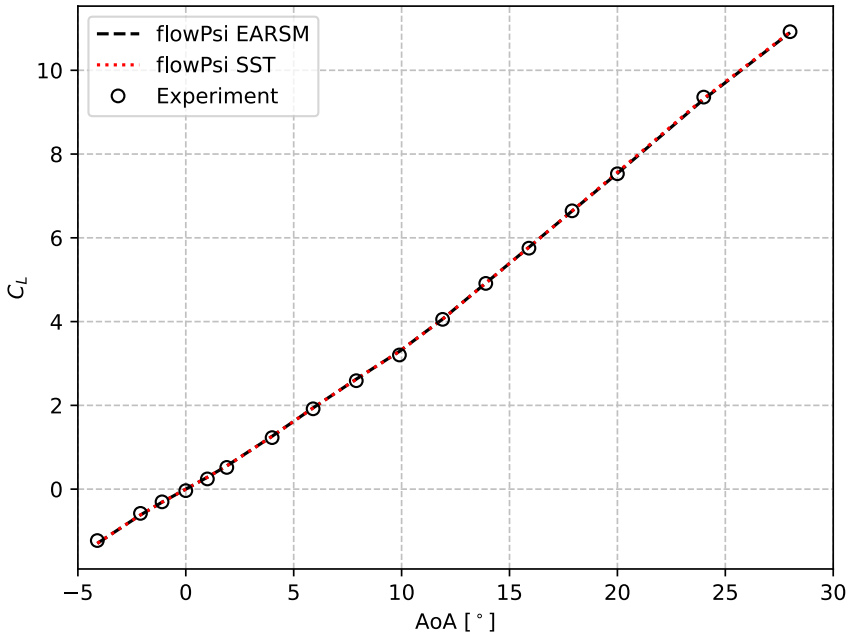

Figure 3.41: Lift coefficient of NASA TCM

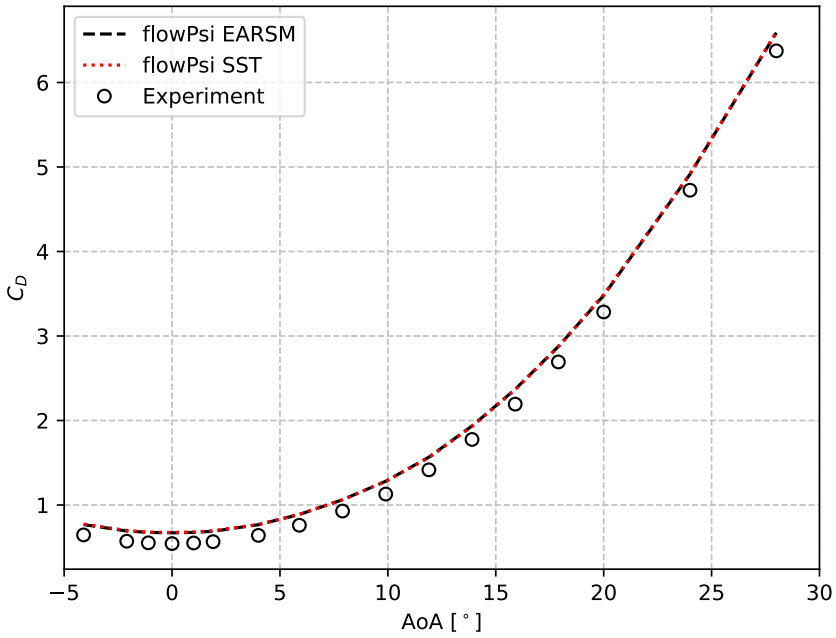

Figure 3.42: Drag coefficient of NASA TCM

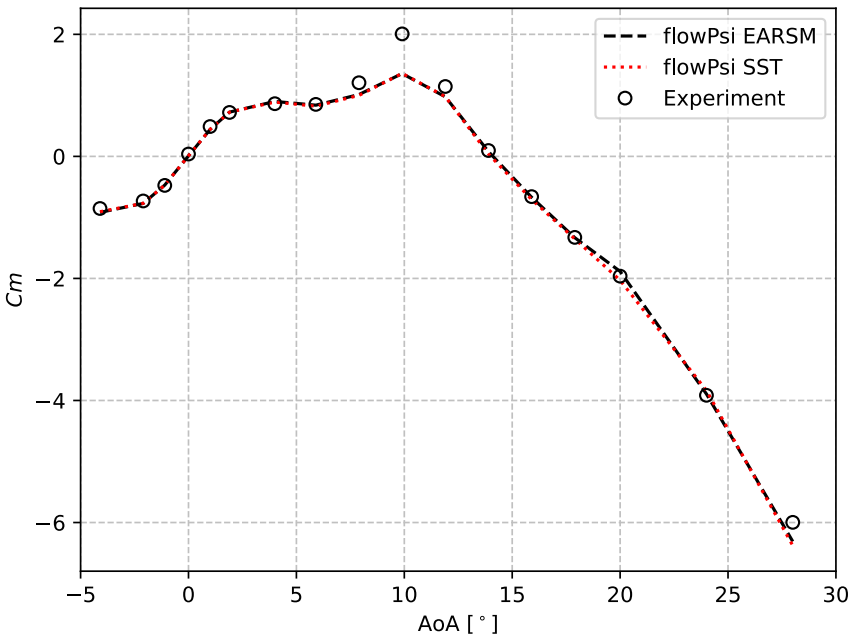

Figure 3.43: Pitching moment coefficient of NASA TCM

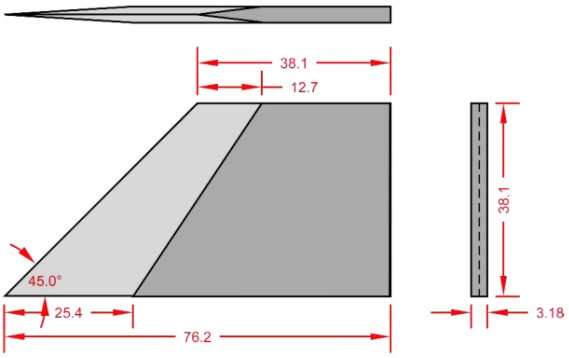

Figure 3.44: Tapered fin geometry dimensions in mm, as taken from Beresh [11]

3.7 Fin Trailing Vortex

As the final test case, the experiment of Beresh et al. [11] is studied. In this experiment, fin trailing vortex measurements at different transonic Mach numbers, Reynolds numbers, and angles of attack were conducted. The geometry of the tapered fin ,which the vortex sheds from, is given in Figure (3.44). The fin surface is attached to the surface of the test section, which has a $305 \times 305\ mm^2$ rectangular cross-section. For the present test case, experimental conditions are given in Table 3.7 for the assessment.

The grid utilized in the present study is the same as the grid used by Dikbaş and Baran

Table 3.7: Fin trailing vortex experiment conditions

Mach	Reynolds	$\alpha[^\circ]$
0.80	$19 \times 10^6 m^{-1}$	10

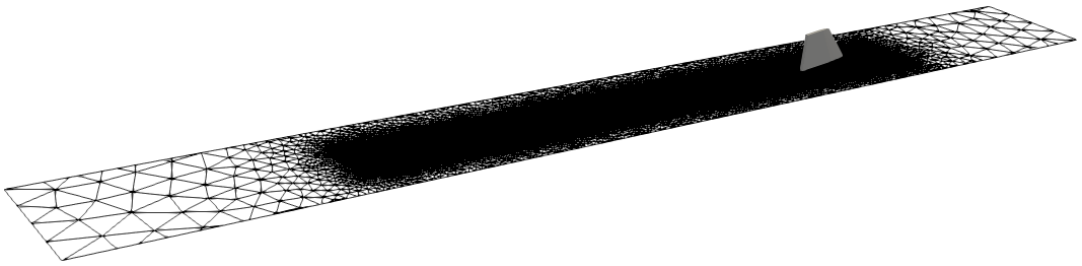

Figure 3.45: Fin trailing vortex grid

[68]. Therefore, the grid convergence is verified in this study. The grid has approximately 24.8 million elements and a maximum wall y^+ value of 0.74. The walls of the test section in the experiment as well as the fin wall are modeled as viscous walls. Also, grid elements on the lower wall, where the isolated fin is attached, have fine enough resolution to better capture the trailing vortex. Grid elements on the lower wall can be seen in Figure 3.45.

Firstly, the tangential velocity distributions near the vortex cores at four different cross sections in the x-direction are presented in Figure 3.46. Velocity profiles show that both the SST and EARSM shows excessively diffusive flow field near the vortex core, as seen from the velocity profiles near this zone. This is due to the excessive eddy viscosity prediction of the turbulence models at high gradient areas. The excessive turbulent viscosity results in excessive viscous dissipation. This dissipation prevents conservation of the strength of the vortex core. Moreover, we can see that the EARSM has more diffusive behavior away from the fin compared to the SST. Thus, we can observe that the implementation of EARSM is not followed by an improvement in the vortex modeling performance.

Figures 3.47, 3.48, and 3.49 show normal Reynolds stresses obtained from the Hellsten EARS $k - \omega$ model and the experiment of Beresh et al. [11]. These figures show that the EARSM overpredicts the normal stresses in the vortex cores. Also, it can be seen that the tangential normal stresses in Figures 3.47 and 3.48 are similar to

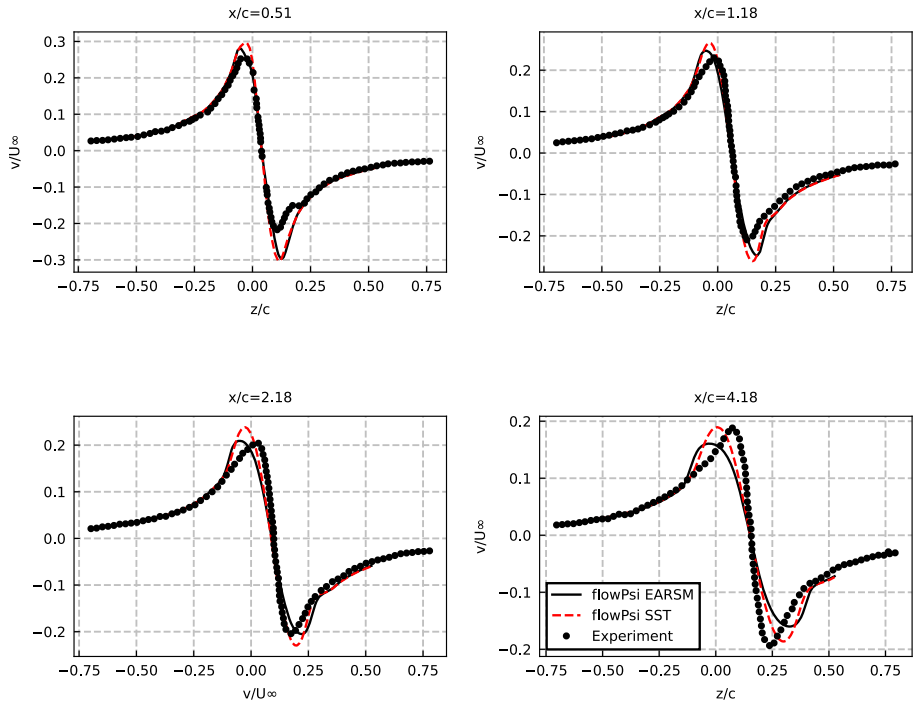

Figure 3.46: y-velocity profiles near the vortex cores at four different cross sections for fin trailing vortex case

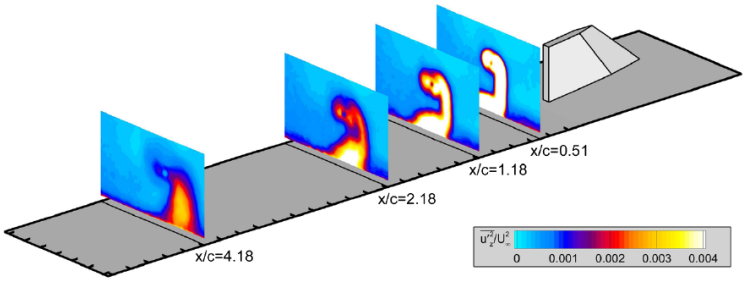

(a) Experiment

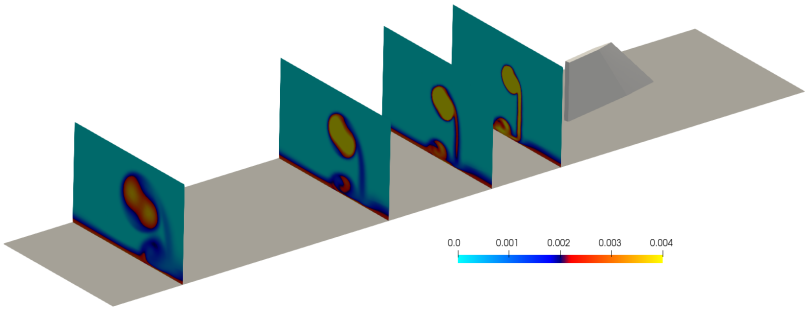

(b) EARSM

Figure 3.47: Reynolds normal stresses in z-direction with the experimental data of Beresh et al. [11]

each other, and the anisotropy of the normal stresses is not well captured. Due to the excessive eddy viscosity predictions, normal Reynolds stresses do not decay with the distance from the fin, as experiment showed.

Finally, Reynolds shear stresses obtained from the EARSM solution are compared with the experiment and presented in Figures 3.50, 3.51, and 3.52. When Reynolds shear stresses are considered, the vortex structure changes with direction. Stresses do not decay with distance, which was seen in the normal stress components.

So, this case showed that the EARSM overestimates the eddy viscosity, which leads to higher Reynolds stresses and a more diffuse distribution of tangential velocity near the vortex cores.

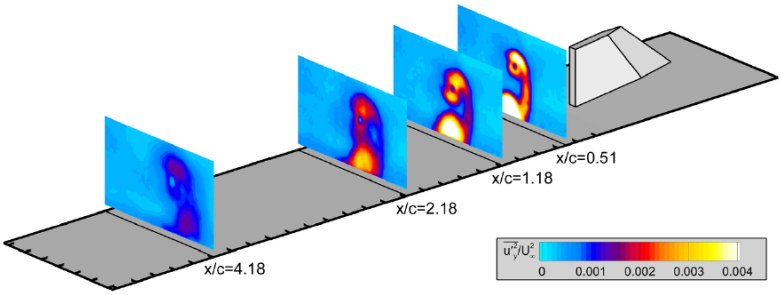

(a) Experiment

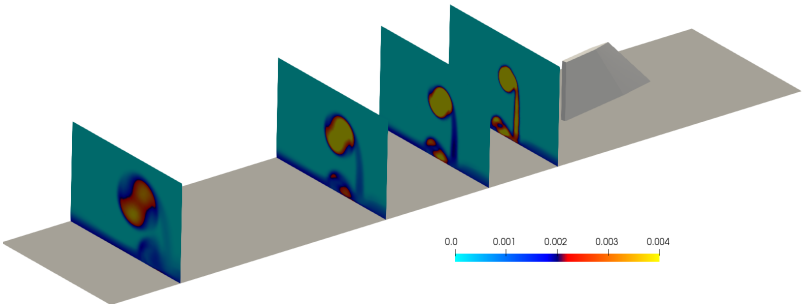

(b) EARSM

Figure 3.48: Reynolds normal stresses in y-direction with the experimental data of Beresh et al. [11]

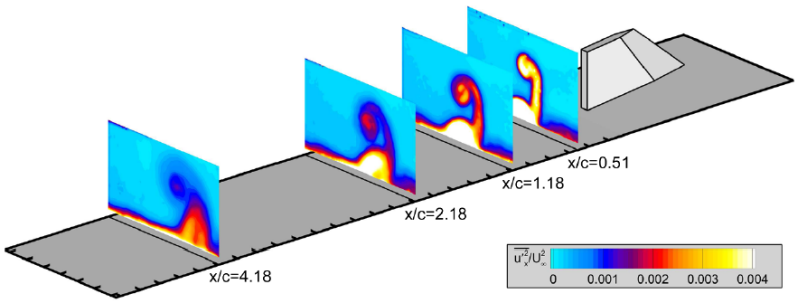

(a) Experiment

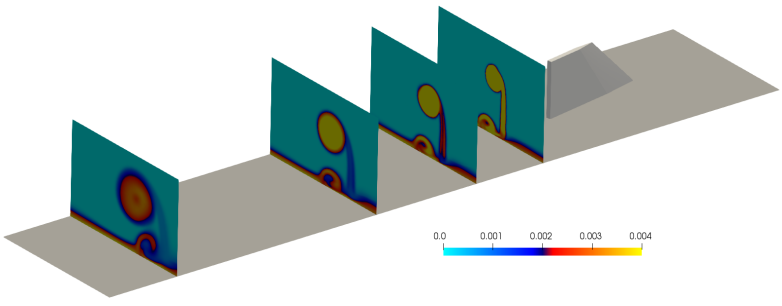

(b) EARSM

Figure 3.49: Reynolds normal stresses in x-direction with the experimental data of Beresh et al. [11]

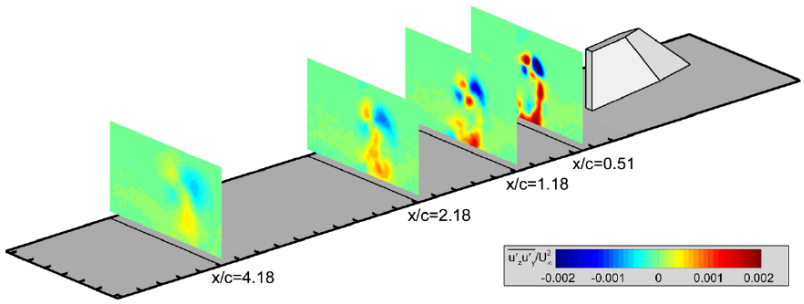

(a) Experiment

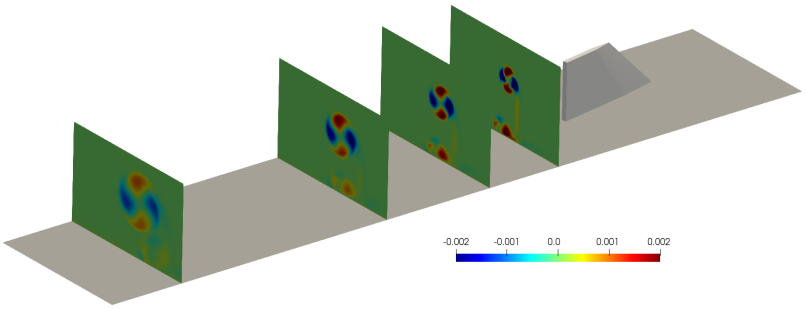

(b) EARSM

Figure 3.50: Reynolds shear stresses ($\overline{u_z' u_y'}/U_\infty^2$) with the experimental data of Beresh et al. [11]

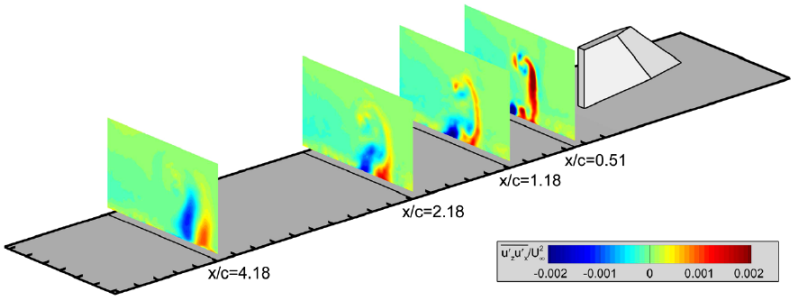

(a) Experiment

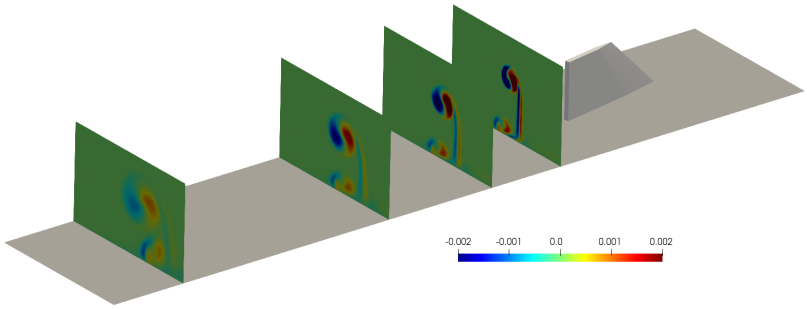

(b) EARSM

Figure 3.51: Reynolds shear stresses ($\overline{u_z' u_x'}/U_\infty^2$) with the experimental data of Beresh et al. [11]

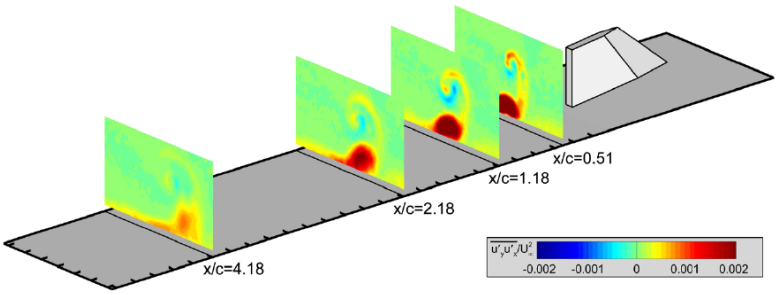

(a) Experiment

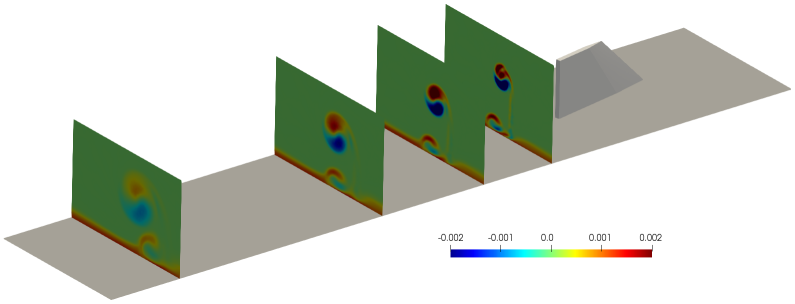

(b) EARSM

Figure 3.52: Reynolds shear stresses ($\overline{u'_y u'_x}/U^2_\infty$) with the experimental data of Beresh et al. [11]

CHAPTER 4

CONCLUSION

4.1 Conclusion

In this thesis, the Hellsten explicit algebraic Reynolds-stress $k-\omega$ model is implemented in an open-source CFD solver called flowPsi. After the implementation, the turbulence model is verified and validated using several test cases, including high-lift aerodynamic problems. The first three test cases, which are zero pressure gradient flat plate, Driver's separating boundary layer, and NACA4412 airfoil with separation, are used to verify that the model is implemented without an error. Also, these test cases showed that the Hellsten's model captures separating flow physics with acceptable accuracy. Flow around RAE2822 airfoil, transonic flow over an axisymmetric bump, fin trailing vortex, and NASA TCM test cases are also thoroughly investigated in order to validate the model in transonic flow and three-dimensional supersonic aerodynamic problems. However, the results obtained with the present model did not show considerable superiority over SST model. These cases demonstrated that, while utilization of the Hellsten EARS $k-\omega$ model is theoretically beneficial, it may require recalibration for the model coefficients. After a proper recalibration study is done for Hellsten's model, this model can improve the solution of aerodynamic problems, especially.

4.2 Future Work

For future work, the curvature-correction introduced by Wallin and Johansson [52] and corrected N introduced by Hellsten et al. [8] can be applied to the model.

Moreover, model coefficients can be recalibrated for different flow problems such as Driver's adverse pressure gradient separated boundary layer utilizing machine learning algorithms to improve model effectiveness. Furthermore, other generic turbulence model test cases, such as ONERA-M6 wing and DLR-F6 test cases, can be used for further validation of the model for aerodynamic flow problems.

REFERENCES

[1] W. Haase, F. Brandsma, E. Elsholz, M. Leschziner, and D. Schwamborn, *EUROVAL—An European Initiative on Validation of CFD Codes: Results of the EC/BRITE-EURAM Project EUROVAL, 1990–1992*, vol. 42. Springer-Verlag, 2013.

[2] T. B. Gatski and T. Jongen, "Nonlinear eddy viscosity and algebraic stress models for solving complex turbulent flows," *Progress in Aerospace Sciences*, vol. 36, pp. 655–682, 2000.

[3] W. J. Devenport and R. L. Simpson, "Flow past a wing-body junction - experimental evaluation of turbulence models," *AIAA Journal*, vol. 30, no. 4, pp. 873–881, 1992.

[4] S. Wallin and A. V. Johansson, "An explicit algebraic reynolds stress model for incompressible and compressible turbulent flows," *Journal of Fluid Mechanics*, vol. 403, pp. 89–132, 1 2000.

[5] P. Klebanoff, "Characteristics of turbulence in a boundary layer with zero pressure gradient," tech. rep., National Bureau of Standards Gaithersburg Md, 1955.

[6] K. G. Winter and L. Gaudet, "Turbulent boundary-layer studies at high reynolds numbers at mach numbers between 0.2 and 2.8," *RAE Technical Report No. 70251*, 1970.

[7] K. Wieghardt and W. Tillmann, "On the turbulent friction layer for rising pressure," 1951.

[8] A. Hellsten and (Otamedia), *New two-equation turbulence model for aerodymamics applications*. Helsinki University of Technology, 2004.

[9] A. Hellsten, "New advanced k-omega turbulence model for high-lift aerodynamics," *AIAA Journal*, vol. 43, pp. 1857–1869, 2005.

[10] D. Coles and A. J. Wadcock, "Flying-hot-wire study of flow past an naca 4412 airfoil at maximum lift," *AIAA Journal*, vol. 17, pp. 321–329, 1979.

[11] S. Beresh, J. Henfling, and R. Spillers, "Turbulence of a fin trailing vortex in subsonic compressible flow," *AIAA Journal*, vol. 50, pp. 2609–2622, 11 2012.

[12] H. Tennekes, J. L. Lumley, J. L. Lumley, *et al.*, *A first course in turbulence*. MIT press, 1972.

[13] C. D. Argyropoulos and N. C. Markatos, "Recent advances on the numerical modelling of turbulent flows," 2015.

[14] K. Hanjalic, "Closure models for incompressible turbulent flows," *Lecture Notes at Von Kármán Institute*, vol. 75, 2004.

[15] J. Boussinesq, "Theorie de l'ecoulement tourbillant," *Mem. Acad. Sci.*, vol. 23, p. 46, 1877.

[16] O. Grundestam, S. Wallin, and A. V. Johansson, "An explicit algebraic reynolds stress model based on a nonlinear pressure strain rate model," *International journal of heat and fluid flow*, vol. 26, pp. 732–745, 2005.

[17] B. Baldwin and T. Barth, "A one-equation turbulence transport model for high reynolds number wall-bounded flows," in *29th aerospace sciences meeting*, p. 610, 1991.

[18] P. Spalart and S. Allmaras, "A one-equation turbulence model for aerodynamic flows," in *30th aerospace sciences meeting and exhibit*, p. 439, 1992.

[19] N. Markatos, "The mathematical modelling of turbulent flows," *Applied Mathematical Modelling*, vol. 10, no. 3, pp. 190–220, 1986.

[20] K. Hanjalic, "Will rans survive les? a view of perspectives," 2005.

[21] B. Launder and D. Spalding, "The numerical computation of turbulent flows," *Computer Methods in Applied Mechanics and Engineering*, vol. 3, no. 2, pp. 269–289, 1974.

[22] W. P. Jones and B. Launder, "The calculation of low-reynolds-number phenomena with a two-equation model of turbulence," *International Journal of Heat and Mass Transfer*, vol. 16, pp. 1119–1130, 7 1973.

[23] W. Rodi and G. Scheuerer, "Scrutinizing the k-ε turbulence model under adverse pressure gradient conditions," 1986.

[24] K. Hanjalic and B. Launder, "Sensitizing the dissipation equation to irrotational strains," 1980.

[25] V. Yakhot, S. Orszag, S. Thangam, T. Gatski, and C. Speziale, "Development of turbulence models for shear flows by a double expansion technique," *Physics of Fluids A: Fluid Dynamics*, vol. 4, no. 7, pp. 1510–1520, 1992.

[26] D. C. Wilcox, "Reassessment of the scale-determining equation for advanced turbulence models," *AIAA journal*, vol. 26, pp. 1299–1310, 1988.

[27] F. R. Menter, "Performance of popular turbulence model for attached and separated adverse pressure gradient flows," *AIAA journal*, vol. 30, no. 8, pp. 2066–2072, 1992.

[28] F. R. Menter, "Review of the shear-stress transport turbulence model experience from an industrial perspective," *International Journal of Computational Fluid Dynamics*, vol. 23, pp. 305–316, 5 2009.

[29] F. R. Menter, "Influence of freestream values on k-omega turbulence model predictions," *AIAA Journal*, vol. 30, pp. 1657–1659, 6 1992.

[30] D. C. Wilcox *et al.*, *Turbulence modeling for CFD*, vol. 2. DCW industries La Canada, CA, 1998.

[31] F. R. Menter, "Zonal two equation k-omega turbulence models for aerodynamic flows," American Institute of Aeronautics and Astronautics Inc, AIAA, 1993.

[32] F. R. Menter, "Two-equation eddy-viscosity turbulence models for engineering applications," *AIAA Journal*, vol. 32, pp. 1598–1605, 1994.

[33] P. E. Smirnov and F. R. Menter, "Sensitization of the sst turbulence model to rotation and curvature by applying the spalart–shur correction term," *Journal of turbomachinery*, vol. 131, no. 4, 2009.

[34] B. P. Reif and P. Durbin, *Statistical theory and modeling for turbulent flows*. John Wiley & Sons, 2011.

[35] P. Y. Chou, "On velocity correlations and the solutions of the equations of turbulent fluctuation," *Quarterly of applied mathematics*, vol. 3, no. 1, pp. 38–54, 1945.

[36] J. Rotta, "Statistische theorie nichthomogener turbulenz," *Zeitschrift fur Physik*, vol. 129, pp. 547–572, 11 1951.

[37] K. Hanjalić and B. E. Launder, "A reynolds stress model of turbulence and its application to thin shear flows," *Journal of fluid Mechanics*, vol. 52, pp. 609–638, 1972.

[38] B. E. Launder, G. J. Reece, and W. Rodi, "Progress in the development of a reynolds-stress turbulence closure," *Journal of Fluid Mechanics*, vol. 68, pp. 537–566, 1975.

[39] C. G. Speziale, S. Sarkar, and T. B. Gatski, "Modelling the pressure-strain correlation of turbulence : An invariant dynamical systems approach," *Journal of Fluid Mechanics*, vol. 227, pp. 245–272, 1991.

[40] A. Hellsten and S. Wallin, "Explicit algebraic reynolds stress and non-linear eddy-viscosity models," *International Journal of Computational Fluid Dynamics*, vol. 23, pp. 349–361, 5 2009.

[41] F. R. Menter, A. V. Garbaruk, and Y. Egorov, "Explicit algebraic reynolds stress models for anisotropic wall-bounded flows," pp. 89–104, EDP Sciences, 2012.

[42] A. Hellsten and S. Laine, "Explicit algebraic reynolds-stress modelling in decelerating and separating flows," American Institute of Aeronautics and Astronautics Inc., 2000.

[43] S. Crippa, "Advances in vortical flow prediction methods for design of delta-winged aircraft," 2008.

[44] V. Hämäläinen *et al.*, *Implementing an explicit algebraic Reynolds stress model into the three-dimensional FINFLO flow solver*. Citeseer, 2001.

[45] S. B. Pope, "A more general effective-viscosity hypothesis," *Journal of Fluid Mechanics*, vol. 72, pp. 331–340, 1975.

[46] T. B. Gatski and C. G. Speziale, "On explicit algebraic stress models for complex turbulent flows," *Journal of fluid Mechanics*, vol. 254, pp. 59–78, 1993.

[47] M. Franke, S. Wallin, and F. Thiele, "Assessment of explicit algebraic reynolds-stress turbulence models in aerodynamic computations," *Aerospace Science and Technology*, vol. 9, pp. 573–581, 10 2005.

[48] R. Abid, C. Rumsey, and T. Gatski, "Prediction of nonequilibrium turbulent flows with explicit algebraic stress models," *AIAA journal*, vol. 33, no. 11, pp. 2026–2031, 1995.

[49] C. L. Rumsey and T. B. Gatski, "Summary of easm turbulence models in cfl3d with validation test cases," 2003.

[50] T. Rung, H. Lübcke, M. Franke, L. Xue, F. Thiele, and S. Fu, "Assessment of explicit algebraic stress models in transonic flows," 1999.

[51] S. S. Girimaji, "Fully explicit and self-consistent algebraic reynolds stress model," *Theoretical and Computational Fluid Dynamics*, vol. 8, pp. 387–402, 11 1996.

[52] S. Wallin and A. V. Johansson, "Modelling streamline curvature effects in explicit algebraic reynolds stress turbulence models," *International Journal of Heat and Fluid Flow*, vol. 23, no. 5, pp. 721–730, 2002.

[53] V. Bělák, P. Sváček, J. Novotnỳ, J. Fürst, and J. Fořt, "On application of earsm turbulence model for simulation of flow field behind rack station," in *EPJ Web of Conferences*, vol. 45, p. 01013, EDP Sciences, 2013.

[54] M. Carri, M. Biava, R. Steijl, G. Barakos, D. Stewart, *et al.*, "Computational fluid dynamics challenges for hybrid air vehicle applications," *Progress in Flight Physics–Volume 9*, vol. 9, pp. 43–80, 2017.

[55] M. Costes and F. Moens, "Advanced prediction of iced airfoil aerodynamics," vol. 0, American Institute of Aeronautics and Astronautics Inc, AIAA, 2018.

[56] J. C. Kok, "Resolving the dependence on freestream values for the k-turbulence model," *AIAA journal*, vol. 38, no. 7, pp. 1292–1295, 2000.

[57] E. A. Luke, X. Tong, and R. Chamberlain, "Flowpsi: An ideal gas flow solver-the user guide," 2021.

[58] E. F. Toro, M. Spruce, and W. Speares, "Restoration of the contact surface in the hll-riemann solver," *Shock waves*, vol. 4, no. 1, pp. 25–34, 1994.

[59] "Turbulence modeling resource." `https://turbmodels.larc.nasa.gov/`. Accessed: 2021-06-12.

[60] D. M. Driver, "Reynolds shear stress measurements in a separated boundary layer flow," American Institute of Aeronautics and Astronautics Inc, AIAA, 1991.

[61] P. Cook, M. Firmin, and M. McDonald, *Aerofoil RAE 2822: pressure distributions, and boundary layer and wake measurements*. RAE, 1977.

[62] F. Lien, G. Kalitzin, and P. Durbin, "Rans modeling for compressible and transitional flows," in *Proceedings of the summer program*, vol. 1, p. 1998, Citeseer, 1998.

[63] L. Davidson and A. Rizzi, "Aiaa 94-0309 reynolds stress transport modelling of transonic flow around the rae2822 airfoil t. reynolds stress transport wiodelling of transonic flow around the rae2822 airfoil," 1994.

[64] J. E. Bardina, P. G. Huang, and T. J. Coakley, "Turbulence modeling validation," 1997.

[65] J. Schaefer, S. Hosder, T. West, C. Rumsey, J. R. Carlson, and W. Kleb, "Uncertainty quantification of turbulence model closure coefficients for transonic wall-bounded flows," vol. 55, pp. 195–213, American Institute of Aeronautics and Astronautics Inc., 2017.

[66] W. D. Bachalo and D. A. Johnson, "Transonic, turbulent boundary-layer separation generated on an axisymmetric flow model," *AIAA Journal*, vol. 24, no. 3, pp. 437–443, 1986.

[67] M. Khalid, P. Henning, M. Mendenhall, and L. Leavitt, "Assesment of turbulence modeling for high-speed vehicles," tech. rep., Technical Report TR-AVT-082, NATO Research and Technology Organization, 2005.

[68] E. DİKBAŞ and Ö. U. BARAN, “Implementation, verification and assessment of vortex capturing capabilities of k-kl turbulence model,” *Isı Bilimi ve Tekniği Dergisi*, vol. 42, no. 1, pp. 113–122, 2022.